Spring 1998

Reduction of Thermal Deflection and Random Response of Composite Structures With Embedded Shape Memory Alloy at Elevated Temperature

Zhiwei Zhong
Old Dominion University

Recommended Citation

Zhong, Zhiwei. "Reduction of Thermal Deflection and Random Response of Composite Structures With Embedded Shape Memory Alloy at Elevated Temperature" (1998). Doctor of Philosophy (PhD), dissertation, Mechanical & Aerospace Engineering, Old Dominion University, DOI: 10.25777/5pde-tq63
https://digitalcommons.odu.edu/mae_etds/188

REDUCTION OF THERMAL DEFLECTION AND RANDOM RESPONSE OF COMPOSITE STRUCTURES WITH EMBEDDED SHAPE MEMORY ALLOY AT ELEVATED TEMPERATURE

by

ZHIWEI ZHONG
B.S. June 1985, Wuhan Institute of Technology
M.S. June 1990, Huazhong University of Science and Technology

A Dissertation Submitted to the Faculty of Old Dominion University
in Partial Fulfillment of the Requirement for the Degree of

DOCTOR OF PHILOSOPHY

ENGINEERING MECHANICS

OLD DOMINION UNIVERSITY
May 1998

Approved by:

Chuh Mei (Director)

Norman F. Knight, Jr. (Member)

Brett A. Newman (Member)

Yong-Xiang Xue (Member)

ABSTRACT

REDUCTION OF THERMAL DEFLECTION AND RANDOM RESPONSE OF COMPOSITE STRUCTURES WITH EMBEDDED SHAPE MEMORY ALLOY AT ELEVATED TEMPERATURE

ZHIWEI ZHONG
Old Dominion University, 1998
Director: Dr. Chuh Mei

A feasibility study on the reduction of thermal deflection and random response of the composite structures using shape memory alloys (SMA) at elevated temperatures is presented in this dissertation. The characteristics of SMA are introduced and the structural problems, static and dynamic, of SMA fiber reinforced composites are investigated. The stress-strain relations are developed for a composite lamina with embedded SMA fibers. The finite element system equations including shape memory effect are derived. A consistent two-step solution procedure is developed for solving the static and dynamic problems of composite structures with embedded SMA fibers subjected to combined acoustic and thermal loads. With the consideration of nonlinear material properties of SMA and geometrically nonlinear deflection, an incremental technique and the Newton-Raphson iteration method have been employed to determine the static response of the SMA embedded composite structures.

Thermal buckling behavior of composite plates with and without embedded SMA has been studied first. The results show that the change of the austenite start temperature of SMA results in the increase of the critical buckling temperature of composite structures with embedded SMA. The study of thermal deflection of SMA hybrid composite structures has revealed that the thermal deflection can be reduced by changing the volume fraction, prestrain, austenite start temperature of SMA, as well as stacking sequence and boundary condition of structures.

The random response analysis of SMA hybrid composite structures indicates that the random response of composite structure with embedded SMA can be significantly reduced by combining proper percentages of SMA volume fraction and prestrain and also altering the austenite start temperature. Thus the benefits of using SMA will maintain the originally designed optimal aerodynamic efficiency at high temperatures during cruise and result in lower noise and longer service life.

ACKNOWLEDGMENTS

I am grateful to my committee chairman, Dr. Chuh Mei, for introducing me to the wonderful world of shape memory alloys and encouraging me to get my Ph. D degree. I would like to thank Dr. Mei for having confidence in me as an engineering student in my graduate study. Dr. Mei's confidence in me as a "survivor" has been a tremendous boost to the confidence I have in myself. I would like to thank committee members Dr. Norman F. Knight, Dr. Brett A. Newman and Dr. Yong-Xiang Xue for their helpful suggestions and consistent willingness to talk to me when I had a problem.

I would like to thank the people closest to me whose love and support have been an absolute necessity in seeing this degree through. I would like to thank my father Weifang Zhong, my mother Yueyun Xie and my brother Zhijun Zhong for their consistent love pride and confidence. Without the unceasing support and encouragement of my parents and brother, I would certainly not be an accomplished engineer.

Finally, I would like to thank my wife Chen Hong for the great love I thought was impossible to find. Her undying support and love has been the basis of my pride and confidence necessary in completing this degree and my life in general. In this respect, I consider myself the luckiest man alive.

If anybody told me eight years ago that I would be an engineer and even more a Ph. D., I might have said they were dreaming. The dream is now a reality and I now have the uncompromised belief that you can do anything you set your mind to. In the immortal words of Steven Tyler of Aerosmith, "Dream on, dream on, dream on, dream yourself a dream come true. Dream on, dream on, dream on, dream until your dream comes true." Without the special people mentioned above, this dream would not have come true.

TABLE OF CONTENTS

APPENDICES

LIST OF TABLES

LIST OF FIGURES

LIST OF SYMBOLS

a	length of rectangular plate
A	area of element matrix
A_s or T_s	austenite start temperature
A_f or T_f	austenite finish temperature
A_{ss}	cross section area of SMA
A_m	cross section area of matrix material
[A], [B], [D]	laminate extensional, extension-bending and bending stiffness matrices
$[A_s]$	shear stiffness matrix
[C]	the matrices relating slope and curvature with displacements
E	Young's modulus
E_s	Young's modulus of SMA
E_m	Young's modulus of matrix material
E[ ]	expected value
{f}	modal force vector
G	shear modulus
G_s	shear modulus of SMA
G_m	shear modulus of matrix material
h	thickness of plate
$H_j(\omega)$	transfer function
[H]	shape function matrix
[k], [K]	element and system linear stiffness matrices

$[k_s]$, $[K_s]$	element and system transverse shear stiffness matrices
$[K_{tan}]$	tangent matrix
$[m]$, $[M]$	element and system mass matrices
$\{M\}$, $\{N\}$	moment and force resultant vectors
$[n1]$, $[n2]$ $[N1]$, $[N2]$	element and system nonlinear stiffness matrices
$\{p\}$, $\{P\}$	element and system force vectors
$\{P_p(t)\}$	random excitation force vector
$\{q\}$	modal coordinate vector
$[Q]$	laminate reduced stiffness
$[Q]_m$	laminate reduced stiffness of the composite matrix
$[\bar{Q}]$	transformed reduced stiffness matrix
$[\bar{Q}]_m$	transformed reduced stiffness matrix of the composite matrix
$\{R\}$	resultant shear force vector
t	time
u, v	in-plane displacements
v_s	volume fraction of SMA
v_m	volume fraction of composite matrix
w	transverse displacement
w_o	initial transverse displacement
x, y, z	Cartesian coordinates

Greek Symbols

α	thermal expansion coefficient
α_s	thermal expansion coefficient of SMA
α_m	thermal expansion coefficient of the composite matrix
β	shear correction factor
ΔT	temperature distribution
$\{\varepsilon\}$, $\{\gamma\}$	strain vectors
$\{\varepsilon_s\}$	strain vector of SMA
$\{\varepsilon_m\}$	strain vector of matrix material
$\{\sigma\}$	stress vector
$\{\sigma_s\}$	stress vector of SMA
$\{\sigma_m\}$	stress vector of matrix material
ς	damping ratio
μ, ν	Poisson's ratio
ρ	mass density
$\{\phi\}$	modal vector
$[\phi]$	modal matrix
ψ_x, ψ_y	rotations of the normal around x and y axes due to bending only
ω	natural frequency
ξ	area coordinate

Superscripts

*	quantity related to temperature

Subscripts

b	bending
c	constant
e	equilibrium
l	linear
m	membrane
Nb	stiffness matrices due to $\{N_b\}$
Nm	stiffness matrices due to $\{N_m\}$
NΔT	stiffness matrices due to $\{N_{\Delta T}\}$
o	quantity related to initial displacement
r	quantity related to recovery stress of SMA
σ	quantity due to initial stress
τ	quantity due to shear stress

CHAPTER I

INTRODUCTION AND LITERATURE REVIEW

The characteristics of Shape Memory Alloys (SMA) are introduced in this chapter. The structural problems, static and dynamic, of SMA fiber reinforced composite structures are investigated. Based on the results from analysis, the potential applications on aerospace vehicles using SMA are revealed.

1.1 Introduction

Many alloys are known to exhibit the shape memory effect. These alloys include the copper alloy family of Cu-Zn, Cu-Zn-Si, Cu-Zn-Sn, Cu-Zn-Al, Cu-Zn-Ga, Cu-Al-Ni, Cu-Au-Zn, the alloys of Ag-Cd, Ni-Al, Fe-Pt and others. Nickel-Titanium alloys (Ni-Ti) are the most common Shape Memory Alloys (SMA). The Ni-Ti alloy series was developed in 1965 by metallurgists Buehler and Wiley of the U.S. Naval Ordinance Laboratory with a United States Patent. The generic name given to this series of alloys was 55-Nitinol, derived from Ni (Nickel)-Ti (Titanium)-NOL (US Naval Ordinance Laboratory now known as the Naval Surface Weapons Center). The 55 refers to the nickel content (weight percent) in the material composition although it can change between 49 and 57 percent. Several other laboratories made early significant contributions to the understanding of the Nitinol, in particular the Battelle Memorial Institute and NASA.

Shape memory alloys exhibit a characteristic phase transformation from martensite to austenite, initiating at the austenite start temperature T_s or A_s and asymptotically ending

---

The journal model for this dissertation is AIAA Journal.

at austenite finish temperature T_f. A shape memory alloy in the low temperature martensitic condition ($T<T_s$), when plastically deformed and the external stresses removed, will regain its original (memory) shape when heated. This characteristic is called the Shape Memory Effect (SME). Shape memory effect is attributed to the material which undergoes a change in crystal structure known as a reversible austenite to martensite phase transformation. For example, strains of typically up to six percent can be completely recovered by heating the Nitinol above the austenite finish temperature.

The transformation temperature of SMA can be altered by changing the composition of the alloy as shown in Fig.1.1 [1]. It is explicit that with only three weight percent change of Nickel, the transformation temperatures can vary from $-50^{\circ}C \ to \ 175^{\circ}C$ for Nitinol. This characteristic enables the designers to determine the composition of Nickel much more flexibly to satisfy the requirements of applications. The solid-solid phase transformation also gives an increase in Young's modulus by a factor of three or four and an increase in yielding strength approximately ten times as shown in Fig.1.2 [2].

Shape memory applications for structures can generally be divided into four groups: free recovery, constrained recovery, work production (actuators) and superelasticity. These groupings are made according to the primary function of the memory element, but are useful in defining common product screening criteria, pitfalls and engineering design parameters. The *Free recovery* group includes applications in which the sole function of the memory element is to cause motion or strain. For example, one could cool a wire into the martensite regime, bend it to a new shape, then heat to recover the original shape.

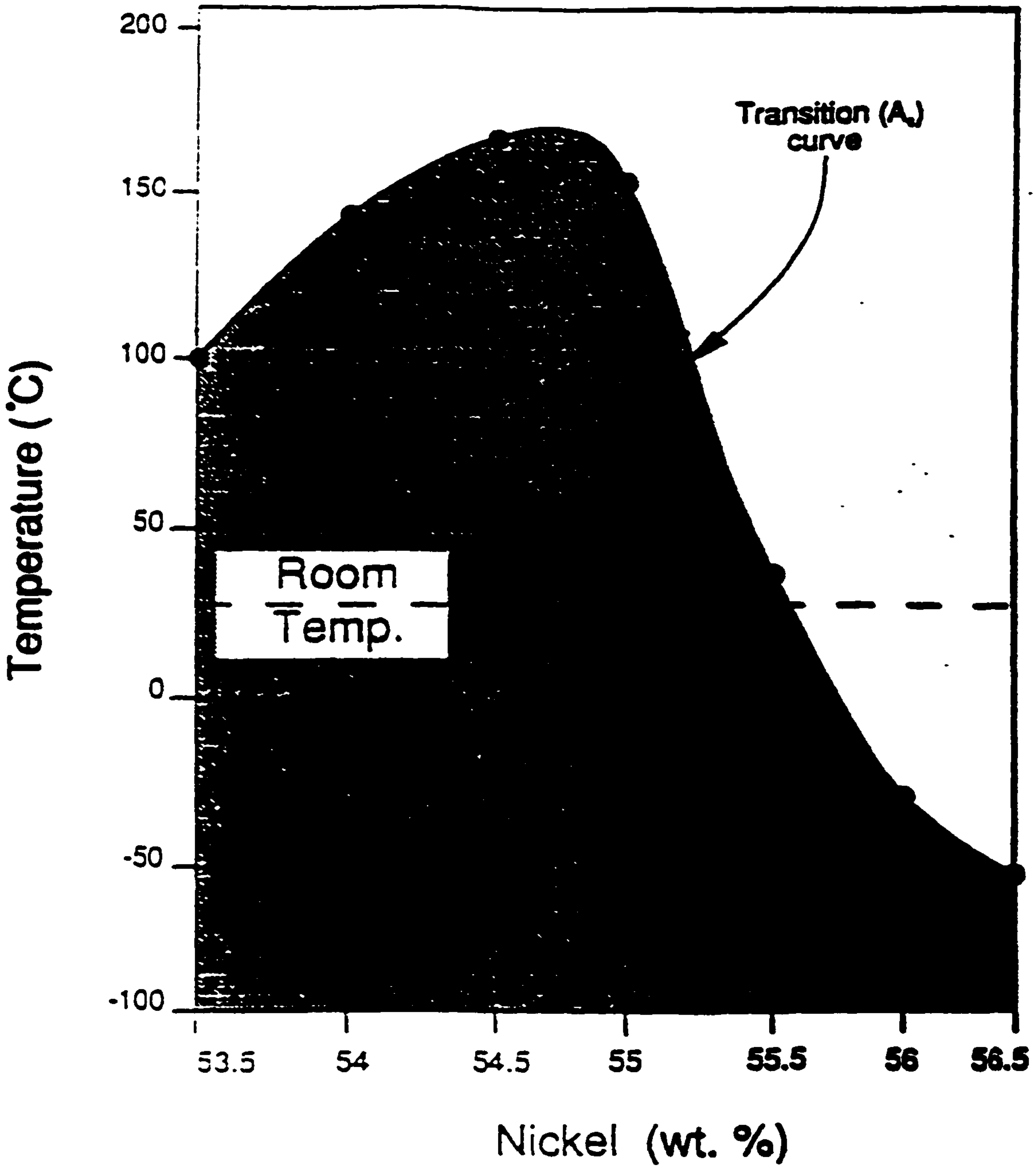

Fig. 1.1 Variation of T_s with Nickle content [1]

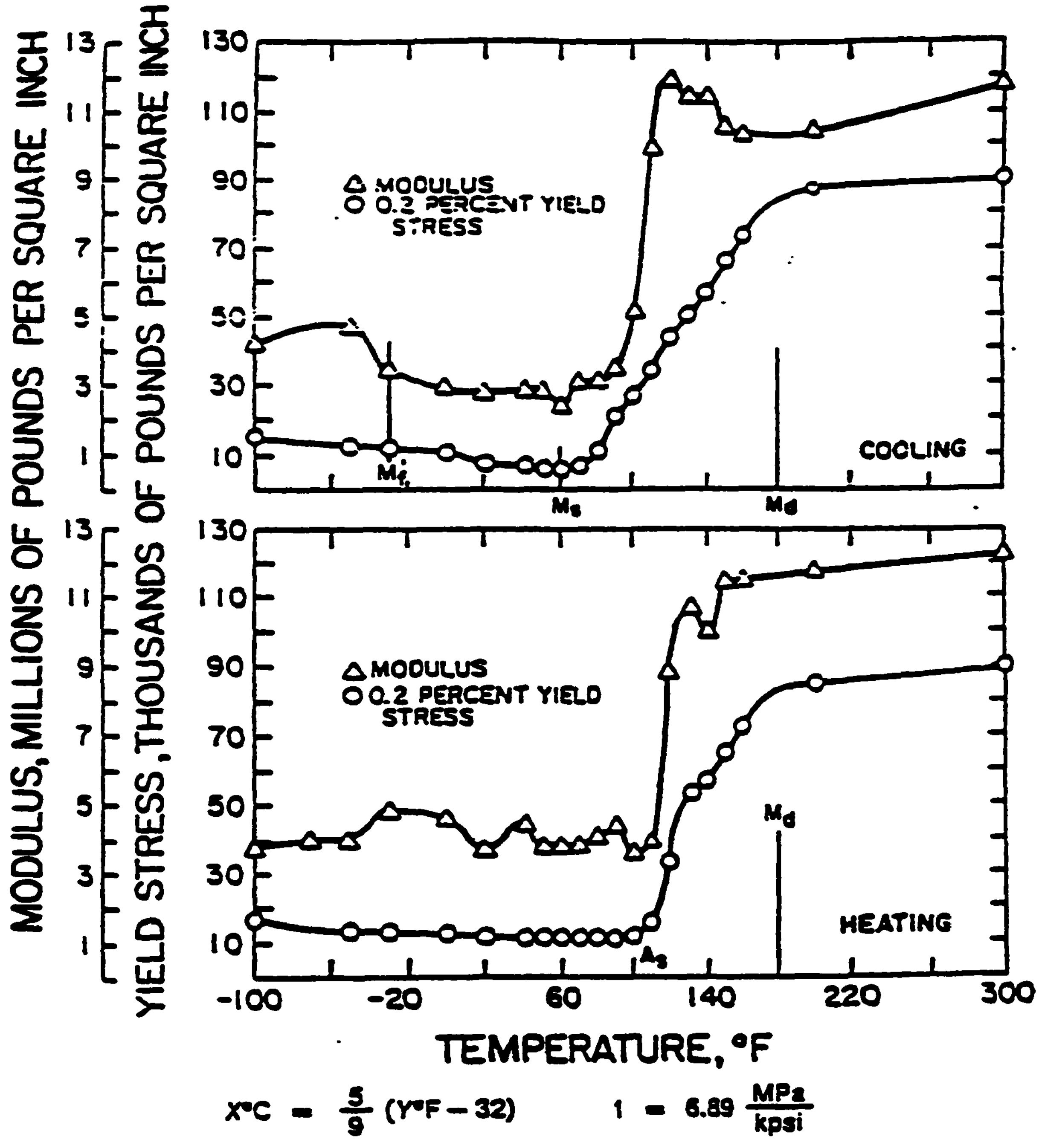

Fig. 1.2 The effect of temperature on the yield stress and elastic modulus [2]

The *constrained recovery* group includes applications in which the memory element is prevented from changing shape and thereby generates a stress. In this case there may be some free recovery before contact is made, but the primary function of the memory element is to generate or induce a stress. The *actuator or work production* group includes applications that are those in which there is motion against a stress and thus work is being done. The ideal case would be a wire or spring which lifts a weight when heated (and perhaps drops the weight again when cooled). More often, the memory element works against a biasing spring. The *superelastic or pseudoelastic* group includes applications that are isothermal in nature and involve the storage of potential energy.

Many studies have contributed to the development of the products and applications using different characteristics of SMA. These studies will be reviewed in the next section entitled Literature Survey. Generally, the behaviors of SMA are dependent on temperature. Thus temperature becomes a very important factor when discussing the applications of SMA. Since the expected aerodynamic heating on the skin panels of the future high-performance flight vehicles, such as the High Speed Civil Transport (HSCT), Advanced Tactical Fighter (ATF) and Reusable Launch Vehicle (RLV), will cause the panel temperature to exceed the austenite finish temperature during supersonic/ hypersonic cruise, SMA will be ideal for such an application. Meanwhile the high panel temperature will result in large geometrically nonlinear deflections of the skin structure. It is expected that SMA can play an important role in the reduction of deflection of panel structures at elevated temperatures. This research extends the study of SMA characteristics and applications on using the nonlinear material properties of SMA as well as reducing large geometrically nonlinear deflections of structures by the use of SMA.

Shape memory effect employed in this study belongs to the category of constrained recovery which can be obtained by embedding initially elongated SMA fibers or wires at low temperature ($T<T_s$) in conventional fiber-reinforced advanced composite panels such as graphite-epoxy. Hence the SMA is constrained and prevented from changing length when heated. The strain due to the initial elongation is called prestrain. Thus, after the SMA is heated above T_s, a large tensile stress is generated in the SMA from the tendency to recover its initial elongation. This tensile stress is called recovery stress as shown in Fig.1.3 [2]. It is explicit that the recovery stress is a nonlinear function of prestrain and temperature. The established constitutive relations and computational methods are to be employed in the presented aerospace application.

1.2 Literature Survey

1.2.1 Characteristics of Shape Memory Alloys

Since shape memory alloys were first revealed in 1965, a great deal of effort was expended over the next ten years in characterizing the material and developing new applications to exploit its remarkable shape memory effect and its unusual mechanical properties. Basically, shape memory effect can be described as follows: an object in the low-temperature martensitic condition, when plastically deformed and the external stress removed, will regain its original (memory) shape when heated. The process, or phenomenon, is the result of a martensitic transformation taking place during heating. Although the exact mechanism by which the shape recovery takes place is a subject of controversy, a great deal has been learned about the unique properties of this class of materials in the past twenty years [3-5]. It is clear, however, that the process of regaining

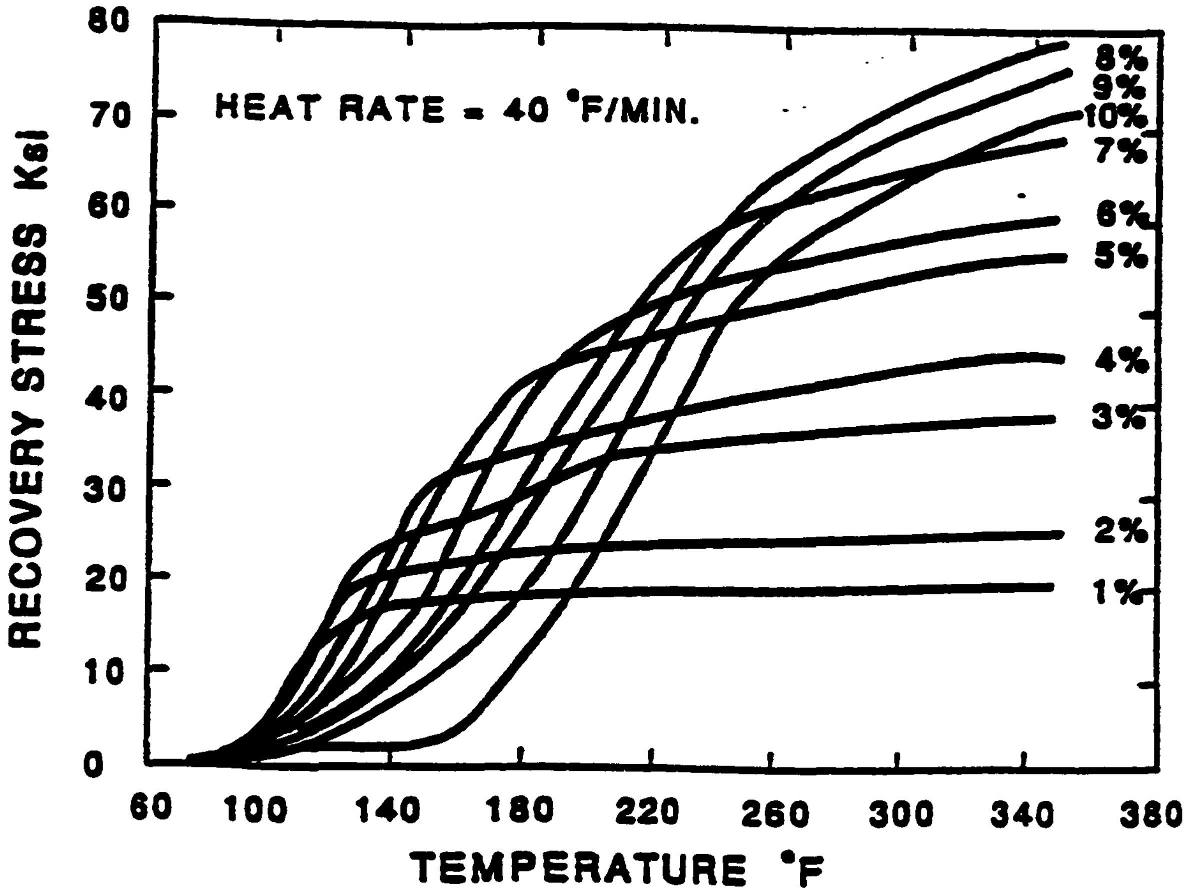

Fig. 1.3 Recovery stress as a function of temperature and prestrain [2]

the original shape is associated with a reverse transformation of the deformed martensitic phase to the higher temperature austenite phase.

Of the many alloys that demonstrate the shape memory effect, Nitinol has been investigated predominantly. For this reason, the properties of Nitinol will be used as the generic SMA properties in this study. The unusual memory behavior is limited to Nitinol having near-equiatomic composition. Plastic strains of typically six percent may be completely recovered by heating the material so as to transform it to its austenite phase. Restraining the material from regaining its memory shape can create stresses of 60,000 psi with the yield strength of martensitic Nitinol being approximately 12,000 psi [2]. It is these force and displacement capabilities that are exploited for electromechanical actuators [6].

Substantial progress has been made in understanding the nature of the shape memory effect. A lot of literature has been published over the past twenty years presenting detailed thermal, electrical, magnetic, and mechanical characteristics of this unusual alloy [7-11]. Because of the unique characteristics of SMA material properties, it is expected that numerous advantages can be gained by using SMA in smart structural applications.

1.2.2 SMA Fiber-Reinforced Composite Structure

Since the characteristics of SMA have been widely used in scientific areas, only the applications corresponding to the second group are reviewed here. SMA fiber-reinforced hybrid composites are defined as the conventional advanced composite materials such as graphite/epoxy that contain embedded SMA fibers or wires which have been aligned in the same direction as the graphite fibers. Various aspects of integrating SMA elements into host composite materials and desired properties has been developed [12-20].

As mentioned previously, the application of SMA corresponding to the second group is constrained recovery which means that the SMA elements are prevented from the shape change even though the external condition such as temperature is increased. A large tensile stress is generated in the SMA due to the constraint. This stress can be used to alter the static and dynamic behaviors of composite structures with embedded SMA fibers. For static analysis, several methods as well as solutions have been proposed to solve the thermal buckling and deflection control problems.

1.2.2.1 Buckling Control

The static characteristics of SMA fiber-reinforced composite structures are primarily governed by their stiffness. The SMA are prestrained and activated to generate significant phase recovery forces in order to increase the in-plane strain energy which in turn increases the critical buckling load of the SMA reinforced composite structures. A finite element model of Nitinol reinforced plates [21] has been developed to describe the interaction between the external loads, operating conditions and the geometrical and physical parameters of the composite plate and the Nitinol fibers. This model predicted the critical buckling loads of Nitinol reinforced plates and then was used to study the buckling characteristics of Nitinol reinforced composites. It was found that reinforcing composite plates with Nitinol fibers can dramatically enhance their critical buckling loads even when these plates are clamped on all their edges. The mathematical models had been developed [22] to enhance the critical buckling loads of long slender beams by using shape memory actuators which are mounted externally on the beam. Based on these developed mathematical models, a closed-loop, computer-controlled system was designed and implemented to control the buckling of simple beams. The testing of a computer-controlled system demonstrated the feasibility of the active control system in preventing the buckling of a flexible beam. The results of an experimental study of buckling of composite beams with embedded Nitinol fibers in resin sleeves have been presented [23, 24]. In these experiments, SMA fibers were electrically activated and heated in response to pre-set deflections of the beam indicating buckling. Tensile recovery forces induced in the SMA brought the buckled beam back to the straight position. It was shown that the buckling load could be increased by a factor of three, as a result of activation of SMA. Experimental results were found to be in close agreement with the finite element solution.

Application of SMA fibers in resin sleeves to control lateral buckling of composite beams has been reported [25]. The results obtained by the finite element analysis were in an excellent agreement with experiment data. Consequently, some theoretical and experimental methods of solving structural buckling problems have been developed, and the results were shown for a particular group [21-25]. But the dependence of the material properties of SMA on the temperature and the thermal effects of the structures due to the change of temperature were not considered in their finite element analysis. Thus, improvement of the finite element model is needed when the SMA fiber-reinforced hybrid composite structure is subjected to a combination of acoustic and thermal loads. As follows from the studies in [21-25], SMA fibers can successfully control lateral buckling of beams. A classical model for processing buckling analysis of SMA embedded composite rectangular plates had been proposed [26]. The results revealed that SMA fibers are stiffened within a composite to alter the critical buckling load of the structure.

However, they considered only the effects of SMA recovery stress but neither the temperature effect of the composite matrix nor the temperature dependent material properties of SMA. It is more likely that this classical model can not be used for the applications of SMA in high- performance flight vehicles.

1.2.2.2 Deflection and Shape Control of SMA Embedded Composite Structures

As one of the important characteristics, the shape memory alloy embedded in conventional composite materials will generate the recovery stress when it activates. The recovery stress can return a structure to its original shape after being deformed by a load. In the deflection control area using SMA, the deflection control concept has been proposed [27]. The deflections of a centrally loaded clamped-clamped SMA hybrid graphite/epoxy plate (10x10x0.03 in.) with a 15% volume fraction of Nitinol prestrained to 3% were measured. When activated, the SMA elements can reduce the deflection by as much as 30%. The recovery stress induced from SMA reduces the beam's deflection similar to pretensioning a loaded cable in order to reduce the cable's deflection.

The theory of hybrid composite plates using micromechanics based on the mechanics of materials approach (rule of mixtures) has been presented [28]. The temperature effect of the composite matrix and the temperature dependent material properties of SMA were ignored. The solution of the bending problem was obtained for a simply supported symmetrically laminated plate by the Rayleigh-Ritz method. In addition to bending, the paper presented results illustrating that SMA fibers can affect natural frequencies, mode shapes of free vibrations, acoustic transmission, and buckling loads of composite plates.

The use of SMA wires to reduce radial expansion of an internally pressurized composite cylinder has been investigated [29]. In the cylinder deflection control concept, SMA wire is continuously wrapped around or within a composite cylinder much like filament winding the composite reinforcing fibers. The SMA is anchored only at the wire ends. When heated, the SMA attempts to recover against the inner composite layers and internal pressure which constrain the shape recovery. Consequently, the SMA recovery force effectively applies an external pressure to the cylinder reducing the internal pressure induced radial expansion. However, the previous work [27-29] dealing with the deflection control using SMA is not concerned about the temperature effects on matrix material which may play a very important role.

The one-dimensional constitutive theory of modeling the behavior of SMA [11] has been employed to solve the problem of control of geometrically linear and nonlinear deformations of beams using SMA actuators [30]. Cylindrical bending of a laminate consisting of outer piezoceramic layers and an inner SMA (Nitinol) layer was studied [31]. It was shown that energy is lost during the cycle of the applied electric field as a result of the stress-induced martensitic transformation. The investigation of tension/compression, bending and torsional deformations of composite beams, as a result of activation of SMA wires, using a simple analytical model and experiments has been reported [32].

The problem of an optimal distribution of SMA stiffeners-actuators to reduce static bending of sandwich panels was addressed [33]. An optimum design was based on the requirement of minimal transverse deflections of the panel subject to a constraint on the volume of the SMA material.

Deformations and local stresses in a SMA hybrid composite consisting of Nitinol fibers embedded within an elastic matrix were considered [34]. The solution utilized the multi-cell micromechanical method, a constitutive theory for SMA, and a three-phase concentric cylinder model for evaluation of local stresses. The results illustrated that substantial longitudinal strains may be induced in a SMA composite, even if the volume fraction of SMA fibers remains rather small (30%). The magnitude, and even the sign of local stress, were shown very sensitive to the martensitic fraction in SMA fibers.

A distribution of temperature in hybrid composites with SMA fibers activated represents an important issue. The investigation on deformation of SMA fiber reinforced composite structures arises for the possible applications such as high-performance flight vehicle under the combined thermal and dynamic mechanical loads. To the best knowledge of the author, there is no literature existing in solving thermal deflection or thermal postbuckling of SMA embedded composite structures.

1.2.2.3 Dynamic Response Control of SMA Reinforced Composite Structures

The dynamic response of composite structures with SMA can be changed by the variation of SMA volume fraction, SMA prestrain, or external condition such as temperature and load. A lot of contributions have been made to address the applications of SMA in this area. One analytical approach was formulated and results were generated [26, 35-39]. Generally, the activation of SMA fibers resulted in the changes of overall stiffness of the hybrid composite as well as the modification of its natural frequencies and mode shapes. It was shown that the natural frequencies of a quasi-isotropic hybrid composite plate of graphite/epoxy and Nitinol/epoxy lamina could be increased by 73% as a result of the activation [37]. This solution was based on an assumption that the recovery tensile stress in embedded SMA fibers was equal to 280 MPa, while thermal effects on the composite material (thermally-induced stress and a degradation of the properties) could be disregarded. In an experimental study [40], the natural frequency of a graphite/epoxy beam was increased by 200% as a result of the activation of Nitinol wires that constituted only 15% of the beam volume fraction. A beneficial effect of SMA fibers on dynamic characteristics of beams was shown [41]. The problems associated with an application of SMA for an active vibration control in flexible structures were discussed [42]. SMA fibers were applied to control flexible linkage mechanisms using temperature controlled variations of the elasticity modulus of SMA [43]. One-dimensional constitutive theory of modeling the behavior of SMA and the first thermodynamic law were employed to illustrate that SMA wires can effectively reduce vibrations of a cantilever beam [44].

A novel design of SMA actuators for hybrid composites has been introduced [45]. The SMA wire (fiber) was placed in a resin sleeve eliminating a direct contact and bonding between the active material and the composite medium. The concept was applied to the active control of vibrations of composite beams. The solution incorporated thermal effects due to heating of SMA fibers. Finite element procedures have been developed and accounted for both thermal and mechanical effects and their interaction. Analytical results that were in a close agreement with experiments illustrated a potential for the control of natural frequencies. A utilization of both the stiffening and the energy-dissipation mechanisms of SMA fibers has been considered [46]. This enabled them to control vibrations of composite beams over a broad frequency spectrum optimally. Experimental and analytical research on dynamics of composite beams reinforced by Nitinol fibers embedded within resin sleeves have been continued [47]. In particular, the problem of an unintentional thermal activation of Nitinol fibers, as a result of the activation of selected fibers, and the consequences for dynamic characteristics of the structure has been discussed [48]. However, in the dynamic analysis of the particular team [46-48], the dependence of the material properties of SMA on the temperature and the thermal effects due to the change of temperature were not paid enough attention.

The active control of rotating open profile beams using SMA has been considered [49]. The beams considered in [49] included composite and SMA layers, the latter being constructed of SMA fibers embedded within a resin matrix (thermal effects on the composite material and thermally-induced compressive stresses were disregarded). As was indicated in the paper, even 13% volume fraction of SMA changed the fundamental frequency of a clamped graphite/epoxy beam by 34%. In addition, it was shown that SMA can guarantee constant frequencies of graphite/epoxy I-beams in the broad range of rotational velocities.

The experimental results for plates with SMA actuators mounted on the edges has been presented [50]. Such mounts suggested as an alternative to embedded SMA actuators represent an interesting approach that many enhance a feasibility of practical applications of SMA. One of the advantages of mounts is a possibility to reduce thermal effects on the main structure, while providing an easy access to SMA elements. The results presented for three different types of boundary conditions illustrated that the natural frequencies can be significantly increased as a result of the activation of the edge mounts. In particular, the fundamental frequencies increased in the range from 26% to 51%, dependent on the boundary conditions.

An effect of SMA fibers in silica tubes on the natural frequencies of composite beams has considered [51]. The analytical frequency solution that employed the stress-strain curves obtained experimentally was in a close agreement with experimental frequency results. The conclusions included a necessity to cycle SMA wires to achieve their stable performance as actuators. The fundamental frequency was increased by 22% even as a result of the activation of a single 22-mil diameter wire. The activation of 25 wires of the same diameter resulted in a 276% increase in the natural frequency.

The reduction of vibrations of rotating machinery by a "stiffness scheduling" achieved by changing the stiffness of SMA wires has been proposed [52]. The transmissibility of Nitinol springs and a utilization of their high intrinsic damping have recently been considered [53]. Experimental evidence reported in the paper indicates that significantly improved properties can be achieved in SMA springs compared to their counterparts manufactured from steel or INCONEL. The vibrations of a sandwich panel with SMA fibers embedded within resin sleeves and positioned at the middle plane has been considered [54]. It was shown that the fundamental frequency can be kept equal to or above the frequency at room temperature. An optimized nonuniform distribution of SMA fibers was even more beneficial for the control of the frequencies.

SMA material can be used in changing the dynamic characteristic of the structures. This makes SMA widely applied to various areas. However, for high-performance flight vehicles and aerospace sonic fatigue applications [55], the structures in most case undertake thermal and random loads. Thus the dynamic response of such structures subjected to the thermal and random loads becomes most important in evaluation of dynamic behavior of these structures. In the author's view, there is no literature existing to solve the dynamic problems for SMA fiber-reinforced composite structures under the thermal and random loads.

1.2.3 Nonlinear Material Properties

The material properties of SMA are nonlinear functions of temperature and prestrain. Large recovery stresses are induced in the constrained structures when SMA fibers are embedded and activated under a certain condition. This induced stress is also a nonlinear function of temperatures and prestrains. Thus approaches to solve structural problems with nonlinear material properties are needed when dealing with SMA applications. Many research results dealing with the deflection control using nonlinear material properties exist in the literature [56-61]. A finite element analysis procedure of large elastic-plastic transient deformations of simple structures has been proposed [56-58]. The assumed-displacement finite element approach, which is based on the principle of virtual work (displacement) and D'Alembert's principle, is applied to analyze the large-displacement, elastic-plastic, strain-harding, transient, Kirchhoff-type responses of general curved beam and the dynamic responses of cylindrical shells to transient loading. The finite element method has been applied to obtain solutions for two-dimensional (axisymmetric or plane) wave propagation problems including the effects of finite strain and material nonlinearities [59]. The finite element method which employs a convected co-ordinate technique and a direct nodal force computational scheme of considerable efficiency has been developed for the transient analysis of large-displacement, small-strain problems with material nonlinearities [60]. The detailed formulations were given for a plane, constant strain triangular element and a Euler-Bernoulli beam element. Several solution techniques such as Newton-Raphson method, direct minimization of the total potential, incremental stiffness procedure and static perturbation method have been discussed to apply on the nonlinear problems [61]. These methods and techniques are very helpful in the analysis of SMA applications.

1.3 Objective and Scope

The major objective of this dissertation is to investigate analytically the feasibility of using shape memory alloys to reduce the thermal deflection and random response at elevated temperatures for a hybrid composite laminate under thermal and acoustic loads.

The documentation of the present research is organized as follows. Chapter I presents an overview of characteristics of SMA and provides a review of using SMA to improve structural behaviors performed by other researchers. Chapter II presents the development of the constitutive relations for a SMA fiber reinforced lamina. These relations include the factors of SMA material properties and temperature effects on both SMA fibers and matrix materials. Also in Chapter II, the finite element formulation with the effects of nonlinear material properties is derived based on von Karman large deflection theory and the first order shear deformation theory. Chapter III presents a consistent two-step solution procedure for structural response for thermal and random excitation loads. This procedure results in solving two sets of equations, a set of nonlinear static equilibrium equations and a set of linear dynamic equations. For nonlinear material properties, the incremental method is used, that is the material properties are treated as constant within each small increment in temperature. The Newton-Raphson iterative method for solving nonlinear algebraic equation is employed for thermal deflection in each temperature increment. Chapter IV presents the numerical results and discussions for four types of analysis: thermal buckling, thermal deflection or postbuckling, vibrations about thermally buckled position, and random responses under acoustic excitation and thermal load. Chapter V presents conclusions and future work from this study.

CHAPTER II

FINITE ELEMENT FORMULATION

In this chapter, the equations of motion with consideration of large deflection and nonlinear material property are derived for a composite plate with embedded SMA subjected to a combined thermal and random excitation loads. The thermal load accounts for an arbitrary spatial distribution and steady-state temperature rise, i.e, $\Delta T=\Delta T(x, y, z)$. The random load is considered as a uniformly distributed stationary band-limited white noise. For the combined thermal and acoustic loads, a consistent two-step solution procedure is employed. In addition, because of the nonlinear material properties of SMA, the incremental method is used for the equilibrium equations in determining thermal deflections. For each small temperature increment, the thermal deflection and corresponding stress are first determined with the material properties which are approximated as constant. Then the thermal deflection and stress are updated and treated as initial deflection and stress for the next increment. Thus, the initial deflection and stress resultants are to be taken into account. The following theories are used and assumptions are made in deriving the equations:

1) Initial state of deformation, which consists of initial transverse deflection $w_o(x, y)$ and in-plane deflections $u_o(x, y)$, $v_o(x, y)$,
2) Initial state of stress $\{\sigma_o\}$, $\{\tau_o\}$,
3) In-plane recovery stress from SMA, $\{\sigma_r^*\}$,
4) Arbitrary temperature distribution $\Delta T(x, y, z)$,
5) von Karman large deflection theory, and
6) Composite materials with transverse shear deformation.

The three-node triangular Mindlin plate element (MIN3) with improved transverse shear is employed in this study. The linear stiffness and mass matrices for the MIN3 element were developed by Tessler and Hughes [62].

2.1 Displacement Functions

A typical MIN3 element is shown in Fig. 2.1. Generally, for a plate structure, the node displacement vector {w} consists of transverse bending, rotation, and membrane displacement components. In MIN3 element, the displacement functions of the middle surface are u, v, w and the normal rotations are ψ_x and ψ_y about x and y axes due to bending only. The displacement field can be written in the following form

$$\begin{aligned} u &= u(x,y,t) + z\psi_y(x,y,t) \\ v &= v(x,y,t) + z\psi_x(z,y,t) \\ w &= w(x,y,t) \end{aligned} \tag{2.1}$$

Thus, the nodal displacement vector is defined

$$\begin{aligned} \{w\}^T &= [[w_b],[\psi],[w_m]] \\ &= [[w_1,w_2,w_3],[\psi_{x1},\psi_{x2},\psi_{x3},\psi_{y1},\psi_{y2},\psi_{y3}],[u_1,u_2,u_3,v_1,v_2,v_3]] \end{aligned} \tag{2.2}$$

where the subscripts b and m denote transverse bending deflection and in-plane deflection components, respectively.

The displacement distribution within an element is described by interpolation functions and can be written in the form [62]

$$\begin{aligned} w(x,y,t) &= [H_w]\{w_b\} + [H_{w\psi}]\{\psi\} \\ &= [\xi_1,\xi_2,\xi_3]\{w_b\} + [L_1,L_2,L_3,M_1,M_2,M_3]\{\psi\} \end{aligned} \tag{2.3}$$

$$\begin{aligned}
\psi_x(x,y,t) &= [H_{\psi x}]\{\psi\} = [\xi_1,\xi_2,\xi_3,0,0,0]\{\psi\} \\
\psi_y(x,y,t) &= [H_{\psi y}]\{\psi\} = [0,0,0,\xi_1,\xi_2,\xi_3]\{\psi\} \\
u(x,y,t) &= [H_u]\{w_m\} = [\xi_1,\xi_2,\xi_3,0,0,0]\{w_m\} \\
v(x,y,t) &= [H_v]\{w_m\} = [0,0,0,\xi_1,\xi_2,\xi_3]\{w_m\}
\end{aligned} \tag{2.4}$$

where ξ_1,ξ_2,ξ_3 are the area coordinates , and the transformation between x, y and ξ_i is

$$\begin{Bmatrix} 1 \\ x \\ y \end{Bmatrix} = \begin{bmatrix} 1 & 1 & 1 \\ x_1 & x_2 & x_3 \\ y_1 & y_2 & y_3 \end{bmatrix} \begin{Bmatrix} \xi_1 \\ \xi_2 \\ \xi_3 \end{Bmatrix}$$

and hence, (2.5)

$$\begin{Bmatrix} \xi_1 \\ \xi_2 \\ \xi_3 \end{Bmatrix} = \frac{1}{2A} \begin{bmatrix} x_2y_3 - x_3y_2 & y_2 - y_3 & x_3 - x_2 \\ x_3y_1 - x_1y_3 & y_3 - y_1 & x_1 - x_3 \\ x_1y_2 - x_2y_1 & y_1 - y_2 & x_2 - x_1 \end{bmatrix} \begin{Bmatrix} 1 \\ x \\ y \end{Bmatrix}$$

where A is the area of the triangular element, (x_i, y_i) are the coordinates of the node i, and

$$\begin{aligned}
&2A = (x_2 - x_1)(y_3 - y_1) - (x_3 - x_1)(y_2 - y_1) \\
&L_1 = \frac{1}{8}(b_3N_4 - b_2N_6), \quad L_2 = \frac{1}{8}(b_1N_5 - b_3N_4) \\
&L_3 = \frac{1}{8}(b_2N_6 - b_1N_5), \quad M_1 = \frac{1}{8}(a_2N_6 - a_3N_4) \\
&M_2 = \frac{1}{8}(a_3N_4 - a_1N_5), \quad M_3 = \frac{1}{8}(a_1N_5 - a_2N_6) \\
&N_4 = 4\xi_1\xi_2, \quad N_5 = 4\xi_2\xi_3, \quad N_6 = 4\xi_3\xi_1 \\
&a_1 = x_{32}, \quad a_2 = x_{13}, \quad a_3 = x_{21} \\
&b_1 = y_{23}, \quad b_2 = y_{31}, \quad b_3 = y_{12} \\
&x_{ij} = x_i - x_j, \quad y_{ij} = y_i - y_j
\end{aligned} \tag{2.6}$$

$$\int_A \xi_1^k \xi_2^l \xi_3^m dA = 2A\frac{k!l!m!}{(2+k+l+m)!} \tag{2.7}$$

2.2 Nonlinear Strain-Displacement Relations

The strain-displacement relations in the von Karman sense are given as

$$\{\varepsilon\} = \begin{Bmatrix} \varepsilon_x \\ \varepsilon_y \\ \gamma_{xy} \end{Bmatrix} = \{\varepsilon^o\} + z\{\kappa\} \tag{2.8}$$

where $\{\varepsilon^o\}$ is the in-plane strain vector and $\{\kappa\}$ is the change in curvature vector such that

$$\begin{aligned} \{\varepsilon^o\} &= \begin{Bmatrix} u_{,x} \\ v_{,y} \\ u_{,y} + v_{,x} \end{Bmatrix} + \begin{Bmatrix} w_{,x}^2/2 \\ w_{,y}^2/2 \\ w_{,x}w_{,y} \end{Bmatrix} + \begin{Bmatrix} w_{,x}w_{o,x} \\ w_{,y}w_{o,y} \\ w_{,x}w_{o,y} + w_{o,x}w_{,y} \end{Bmatrix} \\ &= \{\varepsilon_m^o\} + \{\varepsilon_b^o\} + \{\varepsilon_o^o\} \end{aligned} \tag{2.9}$$

$$\{\kappa\} = \begin{Bmatrix} \psi_{y,x} \\ \psi_{x,y} \\ \psi_{y,y} + \psi_{x,x} \end{Bmatrix} \tag{2.10}$$

where the displacement functions of the middle surface, *u*, *v*, *w*, are measured from the initial deflection position shown in Fig. 2.2, and the subscripts m, b, and o denote the in-plane strain components due to membrane, bending, and initial deflection, respectively. The transverse shear strain-displacement relations are given by

$$\{\gamma\} = \begin{Bmatrix} \gamma_{yz} \\ \gamma_{xz} \end{Bmatrix} = \begin{Bmatrix} w_{,y} \\ w_{,x} \end{Bmatrix} + \begin{Bmatrix} \psi_x \\ \psi_y \end{Bmatrix} \tag{2.11}$$

where the "," denotes derivative with respect to the next subscript.

By using finite element displacement functions for MIN3 element, the membrane strain and curvature vectors can be expressed in terms of the nodal displacements. The linear membrane strains become

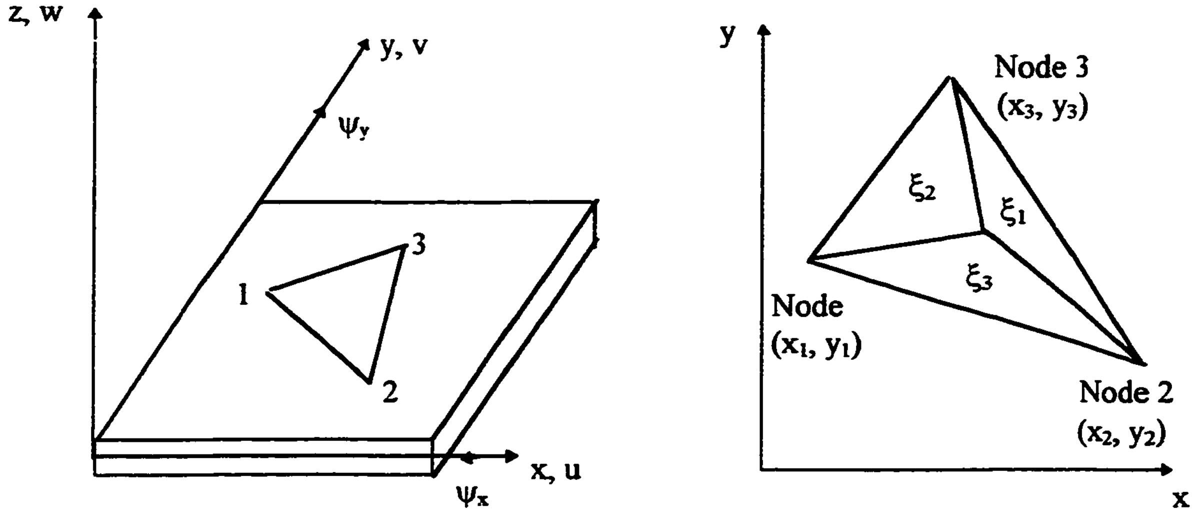

Fig. 2.1 A Mindlin Triangular Plate Element (MIN3)

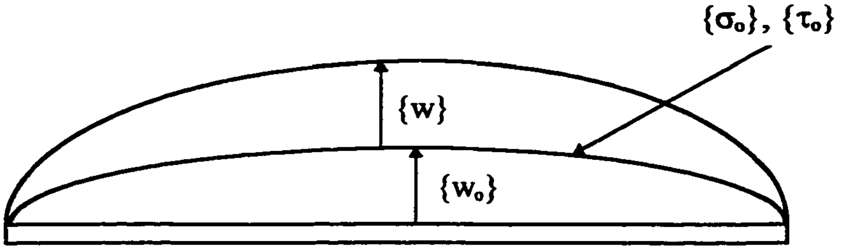

Fig. 2.2 An Initial Deflected and Stressed Plate

$$\{\varepsilon_m^o\} = \begin{bmatrix} \frac{\partial}{\partial x}[H_u] \\ \frac{\partial}{\partial y}[H_v] \\ \frac{\partial}{\partial x}[H_v] + \frac{\partial}{\partial y}[H_u] \end{bmatrix} \{w_m\} = [C_m]\{w_m\} \tag{2.12}$$

The nonlinear membrane strains become

$$\begin{aligned} \{\varepsilon_b^o\} &= \frac{1}{2}\begin{bmatrix} w_{,x} & 0 \\ 0 & w_{,y} \\ w_{,y} & w_{,x} \end{bmatrix} \begin{Bmatrix} w_{,x} \\ w_{,y} \end{Bmatrix} = \frac{1}{2}[\theta]\{G\} \\ &= \frac{1}{2}[\theta]([C_{wb}]\{w_b\} + [C_{w\psi}]\{\psi\}) \end{aligned} \tag{2.13}$$

and the membrane strains due to *w* and *w*ₒ are

$$\begin{aligned} \{\varepsilon_o^o\} &= \begin{bmatrix} w_{o,x} & 0 \\ 0 & w_{o,y} \\ w_{o,y} & w \end{bmatrix} \begin{Bmatrix} w_{,x} \\ w_{,y} \end{Bmatrix} \\ &= [\theta_o]([C_{wb}]\{w_b\} + [C_{w\psi}]\{\psi\}) \end{aligned} \tag{2.14}$$

where the slope matrices [θ] and [θₒ] and the slope vector {G} are

$$\begin{aligned} [\theta] &= \begin{bmatrix} w_{,x} & 0 \\ 0 & w_{,y} \\ w_{,y} & w_{,x} \end{bmatrix}, \qquad [\theta_o] = \begin{bmatrix} w_{o,x} & 0 \\ 0 & w_{o,y} \\ w_{o,y} & w_{o,x} \end{bmatrix} \\ \{G\} &= \begin{Bmatrix} w_{,x} \\ w_{,y} \end{Bmatrix} = \begin{bmatrix} \frac{\partial}{\partial x}[H_w] \\ \frac{\partial}{\partial y}[H_w] \end{bmatrix} \{w_b\} + \begin{bmatrix} \frac{\partial}{\partial x}[H_{w\psi}] \\ \frac{\partial}{\partial y}[H_{w\psi}] \end{bmatrix} \{\psi\} \\ &= [C_{wb}]\{w_b\} + [C_{w\psi}]\{\psi\} \end{aligned} \tag{2.15}$$

It is clear that the following relation exists

$$\begin{aligned} [\theta_o]\{G\} &= \begin{bmatrix} w_{o,x} & 0 \\ 0 & w_{o,y} \\ w_{o,y} & w_{o,x} \end{bmatrix} \begin{Bmatrix} w_{,x} \\ w_{,y} \end{Bmatrix} = \begin{bmatrix} w_{,x} & 0 \\ 0 & w_{,y} \\ w_{,y} & w_{,x} \end{bmatrix} \begin{Bmatrix} w_{o,x} \\ w_{o,y} \end{Bmatrix} \\ &= [\theta]\{G_o\} \\ &= [\theta]([C_{wb}]\{w_{bo}\} + [C_{w\psi}]\{\psi_o\}) \end{aligned} \tag{2.16}$$

The change in curvatures are

$$\{\kappa\} = \begin{bmatrix} \frac{\partial}{\partial x}\left[H_{\psi y}\right] \\ \frac{\partial}{\partial y}\left[H_{\psi x}\right] \\ \frac{\partial}{\partial x}\left[H_{\psi x}\right] + \frac{\partial}{\partial y}\left[H_{\psi y}\right] \end{bmatrix} \{\psi\} = \left[C_b\right]\{\psi\} \tag{2.17}$$

The transverse shear strains become

$$\{\gamma\} = \begin{bmatrix} \frac{\partial}{\partial y}\left[H_w\right] \\ \frac{\partial}{\partial x}\left[H_w\right] \end{bmatrix} \{w_b\} + \begin{bmatrix} \frac{\partial}{\partial y}\left[H_{w\psi}\right] + \left[H_{\psi x}\right] \\ \frac{\partial}{\partial x}\left[H_{w\psi}\right] + \left[H_{\psi y}\right] \end{bmatrix} \{\psi\} = [C_{\gamma b}]\{w_b\} + [C_{\gamma\psi}]\{\psi\} \tag{2.18}$$

where the strain interpolation matrices $[C_m],[C_{\psi b}],[C_{\psi\psi}],[C_b],[C_{\gamma b}]$ *and* $[C_{\gamma\psi}]$ are related to the area coordinates and the nodal coordinates. These matrices are given in Appendix A.

2.3 Stress-Strain Relations of a SMA Embedded Composite Lamina

A representative volume element of a SMA fiber-reinforced composite lamina is shown in Fig. 2.3. The element is taken to be in the plane of the plate. The composite matrix, for example graphite/epoxy, has the principal material directions 1 and 2, and the SMA fiber is embedded in the 1-direction.

In order to derive the constitutive relation for the 1-direction, it is assumed that a stress σ_1 acts alone on the element ($\sigma_2 = 0$) and that the SMA fiber and composite matrix are strained by the same amount, ε_1 (i.e., plane sections remain plane). The 1-direction stress-strain relation of the SMA fiber can be described as

$$\sigma_{1s} = E_s^* \varepsilon_1 + \sigma_r^*, \qquad T > T_s \tag{2.19}$$

or

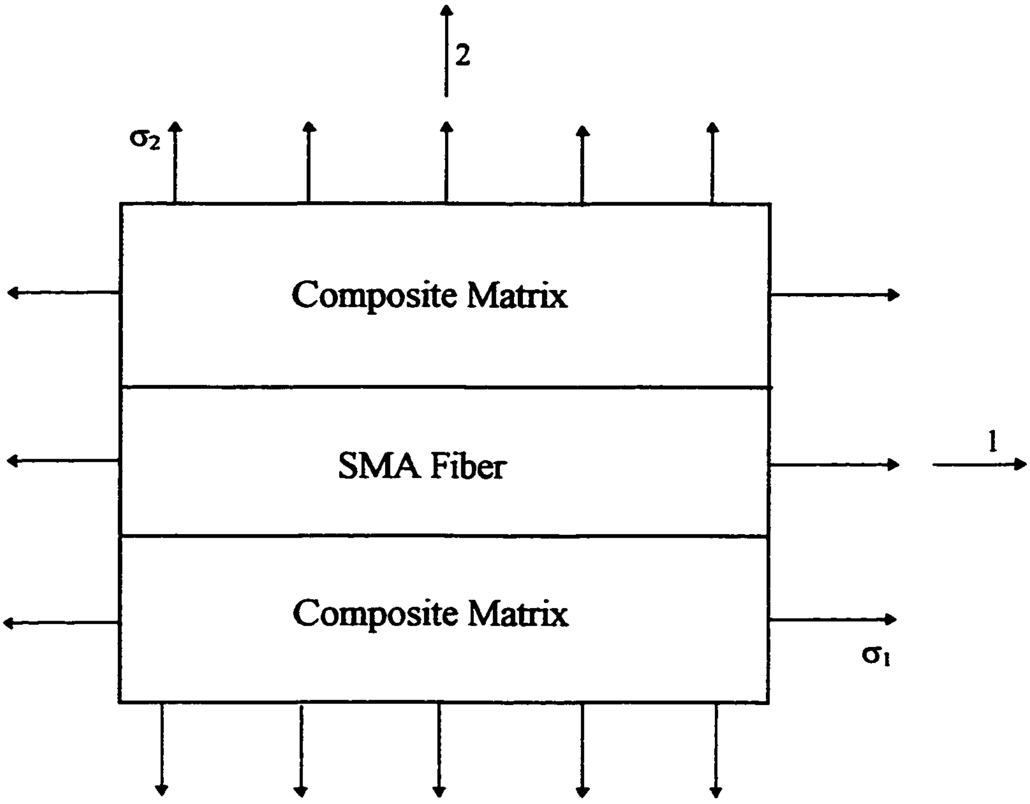

Fig. 2.3 Representative volume element for SMA fiber-reinforced composite lamina

$$\sigma_{1s} = E_s^*(\varepsilon_1 - \alpha_s \Delta T), \qquad T < T_s \tag{2.20}$$

where T_s is the austenite start temperature and α_s is the thermal expansion coefficient. The Young's Modulus E_s^* and the recovery stress σ_r^* are temperature dependent, indicated by superscript (*). The recovery stress σ_r^* is also dependent on the prestrain ε_r which relates to the recovery strain of SMA. For Nitinol, σ_r^* and E_s^* can be determined from Figs. 1.2 and 1.3, respectively. Similarly, the one-dimensional stress-strain relation in the 1-direction for the composite matrix can be expressed as

$$\sigma_{1m} = E_{1m}(\varepsilon_1 - \alpha_{1m}\Delta T) \tag{2.21}$$

The resultant force in the 1-direction $(\sigma_2 = 0)$ is distributed over the SMA fiber and composite matrix and can be written as

$$\sigma_1 A_1 = \sigma_{1s} A_{ss} + \sigma_{1m} A_m \tag{2.22}$$

where (σ_1, A_1), (σ_{1s}, A_{ss}) *and* (σ_{1m}, A_m) are the (stress, cross section area) of the entire element, SMA fiber, and composite matrix, respectively. Thus, the average stress σ_1 is

$$\sigma_1 = \sigma_{1s} v_s + \sigma_{1m} v_m \tag{2.23}$$

where $v_s = A_{ss} / A_1$ and $v_m = A_m / A_1$ are the volume fractions of SMA and composite matrix, respectively. When $T>T_s$, the SMA effect is activated and the one-dimensional stress-strain relation in the 1-direction becomes

$$\begin{aligned} \sigma_1 &= (E_s^*\varepsilon_1 + \sigma_r^*)v_s + E_{1m}(\varepsilon_1 - \alpha_{1m}\Delta T)v_m \\ &= E_1^*\varepsilon_1 + \sigma_r^* v_s - E_{1m}\alpha_{1m} v_m \Delta T \end{aligned} \tag{2.24}$$

where

$$E_1^* = E_{1m} v_m + E_s^* v_s \tag{2.25}$$

When T<Ts, the SMA effect is not activated and the stress σ_1 is

$$\begin{aligned}\sigma_1 &= E_1^* \varepsilon_1 - (E_s^* \alpha_s v_s + E_{1m} \alpha_{1m} v_m)\Delta T \\ &= E_1^*(\varepsilon_1 - \alpha_1^* \Delta T)\end{aligned} \tag{2.26}$$

where

$$\alpha_1^* = \frac{(E_{1m}\alpha_{1m}v_m + E_s^*\alpha_s v_s)}{E_1^*} \tag{2.27}$$

A similar constitutive relation may be derived for the 2-direction by assuming that the applied stress σ_2 acts upon both the fiber and the matrix $(\sigma_1 = 0)$. Thus, the one-dimensional stress-strain relations in the 2-direction for the SMA fiber and the composite matrix become

$$\sigma_{2s} = \sigma_2 = E_s^*(\varepsilon_{2s} - \alpha_s \Delta T) \tag{2.28}$$

and

$$\sigma_{2m} = \sigma_2 = E_{2m}(\varepsilon_{2m} - \alpha_{2m}\Delta T) \tag{2.29}$$

respectively. The recovery stress does not appear in Eq. (2.28), since the SMA fiber prestrain ε_r and recovery stress σ_r^* are considered to be a 1-direction effect only.

The total elongation is due to strain in the composite matrix and the SMA fiber and may be written in the form

$$A_1 \varepsilon_2 = A_m \varepsilon_{2m} + A_{ss} \varepsilon_{2s} \tag{2.30}$$

Thus, the total strain becomes

$$\varepsilon_2 = \varepsilon_{2m} v_m + \varepsilon_{2s} v_s \tag{2.31}$$

Since $\sigma_2 = E_s^*(\varepsilon_{2s} - \alpha_s \Delta T)$, Eqs. (2.28) and (2.29) may be substituted into Eq. (2.31) to give

$$\begin{aligned} \varepsilon_2 &= \frac{\sigma_2}{E_s^*} + \alpha_2 \Delta T \\ &= \frac{\sigma_2 v_s}{E_s^*} + \frac{\sigma_2 v_m}{E_{2m}} + (\alpha_s v_s + \alpha_{2m} v_m)\Delta T \end{aligned} \tag{2.32}$$

Therefore, the modulus and thermal expansion coefficient in the 2-direction become

$$E_2^* = \frac{E_{2m} E_s^*}{(E_{2m} v_s + E_s^* v_m)} \tag{2.33}$$

and

$$\alpha_2 = \alpha_{2m} v_m + \alpha_s v_s \tag{2.34}$$

Expressions for the hybrid composite Poisson's ratios and shear moduli follow from similar derivations.

The constitutive relations for a thin composite lamina with embedded SMA fibers can be derived using a similar engineering approach to give

$$\begin{Bmatrix} \sigma_1 \\ \sigma_2 \\ \tau_{12} \end{Bmatrix} = \begin{bmatrix} Q_{11}^* & Q_{12}^* & 0 \\ Q_{21}^* & Q_{22}^* & 0 \\ 0 & 0 & Q_{66}^* \end{bmatrix} \begin{Bmatrix} \varepsilon_1 \\ \varepsilon_2 \\ \gamma_{12} \end{Bmatrix} + \begin{Bmatrix} \sigma_r^* \\ 0 \\ 0 \end{Bmatrix} v_s - [Q]_m \begin{Bmatrix} \alpha_1 \\ \alpha_2 \\ 0 \end{Bmatrix}_m v_m \Delta T, \quad T > T_s \tag{2.35}$$

$$\begin{Bmatrix} \sigma_1 \\ \sigma_2 \\ \tau_{12} \end{Bmatrix} = \begin{bmatrix} Q_{11}^* & Q_{12}^* & 0 \\ Q_{21}^* & Q_{22}^* & 0 \\ 0 & 0 & Q_{66}^* \end{bmatrix} \left(\begin{Bmatrix} \varepsilon_1 \\ \varepsilon_2 \\ \gamma_{12} \end{Bmatrix} - \begin{Bmatrix} \alpha_1^* \\ \alpha_2 \\ 0 \end{Bmatrix} \Delta T \right), \quad T < T_s \tag{2.36}$$

and

$$\begin{Bmatrix} \tau_{23} \\ \tau_{13} \end{Bmatrix} = \begin{bmatrix} Q_{44}^* & 0 \\ 0 & Q_{55}^* \end{bmatrix} \begin{Bmatrix} \gamma_{23} \\ \gamma_{13} \end{Bmatrix}$$

where $[Q]_m$ and [Q*] are the reduced stiffness matrices of the composite matrix and the composite lamina, respectively. The [Q*] matrix is temperature dependent and is evaluated using the previously derived relations as

$$Q^{*}_{11} = \frac{E^{*}_{1}}{1-\mu_{12}\mu_{21}}$$

$$Q^{*}_{22} = \frac{\mu_{12}E^{*}_{2}}{1-\mu_{12}\mu_{21}} = \frac{\mu_{21}E^{*}_{1}}{1-\mu_{12}\mu_{21}}$$

$$Q^{*}_{22} = \frac{E^{*}_{2}}{1-\mu_{12}\mu_{21}}$$

$$Q^{*}_{66} = G^{*}_{12}$$

$$Q^{*}_{44} = G^{*}_{23}$$

$$Q^{*}_{55} = G^{*}_{13}$$

$$(E^{*}_{1}, \mu_{12}) = (E_{1m}, \mu_{12m})v_m + (E^{*}_{s}, \mu_s)v_s \tag{2.37}$$

and

$$(E^{*}_{2}, G^{*}_{12}, G^{*}_{23}, G^{*}_{13}) = \frac{(E_{2m}E^{*}_{s},\ G_{12m}G^{*}_{s},\ G_{23m}G^{*}_{s},\ G_{13m}G^{*}_{s})}{[(E_{2m}, G_{12m}, G_{23m}, G_{13m})v_s + (E^{*}_{s}, G^{*}_{s})v_m]} \tag{2.38}$$

where the μ's are Poisson's ratios and the G's are the shear moduli. The thermal expansion coefficients α^{*}_{1} and α_2 are derived in Eqs. (2.27) and (2.34).

The stress-strain relationships for a general orthotropic lamina with embedded SMA in nonprincipal coordinates such as *x* and *y* can be obtained using an engineering approach. The stress transformation equations for the stress in the *xy*-coordinate system can be written as

$$\begin{Bmatrix} \sigma_x \\ \sigma_y \\ \tau_{xy} \end{Bmatrix} = \begin{bmatrix} \cos^2\theta & \sin^2\theta & -2\cos\theta\sin\theta \\ \sin^2\theta & \cos^2\theta & 2\cos\theta\sin\theta \\ \cos\theta\sin\theta & -\cos\theta\sin\theta & \cos^2\theta - \sin^2\theta \end{bmatrix} \begin{Bmatrix} \sigma_1 \\ \sigma_2 \\ \tau_{12} \end{Bmatrix} = [T]^{-1} \begin{Bmatrix} \sigma_1 \\ \sigma_2 \\ \tau_{12} \end{Bmatrix} \tag{2.39}$$

where θ is the lamina orientation angle.

The strain transformation equations for the strain in the *xy*-coordinate system can be written as

$$\begin{Bmatrix} \varepsilon_x \\ \varepsilon_y \\ \gamma_{xy}/2 \end{Bmatrix} = \begin{bmatrix} \cos^2\theta & \sin^2\theta & -2\cos\theta\sin\theta \\ \sin^2\theta & \cos^2\theta & 2\cos\theta\sin\theta \\ \cos\theta\sin\theta & -\cos\theta\sin\theta & \cos^2\theta-\sin^2\theta \end{bmatrix} \begin{Bmatrix} \varepsilon_1 \\ \varepsilon_2 \\ \gamma_{12}/2 \end{Bmatrix} = [T]^{-1} \begin{Bmatrix} \varepsilon_1 \\ \varepsilon_2 \\ \gamma_{12}/2 \end{Bmatrix} \tag{2.40}$$

thus

$$\begin{Bmatrix} \sigma_x \\ \sigma_y \\ \tau_{xy} \end{Bmatrix} = [T]^{-1}[Q^*][T] \begin{Bmatrix} \varepsilon_x \\ \varepsilon_y \\ \gamma_{xy}/2 \end{Bmatrix} = \begin{bmatrix} \overline{Q}^*_{11} & \overline{Q}^*_{12} & \overline{Q}^*_{16} \\ \overline{Q}^*_{12} & \overline{Q}^*_{22} & \overline{Q}^*_{26} \\ \overline{Q}^*_{16} & \overline{Q}^*_{26} & \overline{Q}^*_{66} \end{bmatrix} \begin{Bmatrix} \varepsilon_x \\ \varepsilon_y \\ \gamma_{xy} \end{Bmatrix}$$

$$\begin{Bmatrix} \tau_{yz} \\ \tau_{xz} \end{Bmatrix} = \begin{bmatrix} \overline{Q}^*_{44} & \overline{Q}^*_{45} \\ \overline{Q}^*_{45} & \overline{Q}^*_{55} \end{bmatrix} \begin{Bmatrix} \gamma_{23} \\ \gamma_{13} \end{Bmatrix} \tag{2.41}$$

where the $\overline{Q}^*_{ij}$ are the components of the reduced transformed lamina stiffness matrix $[\overline{Q}^*]$, which are defined as follows:

$$\overline{Q}^*_{11} = Q^*_{11}\cos^4\theta + Q^*_{22}\sin^4\theta + 2(Q^*_{12} + 2Q^*_{66})\sin^2\theta\cos^2\theta$$

$$\overline{Q}^*_{12} = (Q^*_{11} + Q^*_{22} - 4Q^*_{66})\sin^2\theta\cos^2\theta + Q^*_{12}(\cos^4\theta + \sin^4\theta)$$

$$\overline{Q}^*_{13} = Q^*_{13}\cos^2\theta + Q^*_{23}\sin^2\theta$$

$$\overline{Q}^*_{16} = (Q^*_{11} - Q^*_{12} - 2Q^*_{66})\cos^3\theta\sin\theta - (Q^*_{22} - Q^*_{12} - 2Q^*_{66})\cos\theta\sin^3\theta$$

$$\overline{Q}^*_{22} = Q^*_{11}\sin^4\theta + Q^*_{22}\cos^4\theta + 2(Q^*_{12} + 2Q^*_{66})\sin^2\theta\cos^2\theta$$

$$\overline{Q}^*_{23} = Q^*_{13}\sin^2\theta + Q^*_{23}\cos^2\theta$$

$$\overline{Q}^*_{26} = (Q^*_{11} - Q^*_{12} - 2Q^*_{66})\cos\theta\sin^3\theta - (Q^*_{22} - Q^*_{12} - 2Q^*_{66})\cos^3\theta\sin\theta$$

$$\overline{Q}^*_{33} = Q^*_{33}$$

$$\overline{Q}^*_{36} = (Q^*_{23} - Q^*_{13})\sin\theta\cos\theta$$

$$\begin{aligned}
\overline{Q}^*_{44} &= Q^*_{44}\cos^2\theta + Q^*_{55}\sin^2\theta \\
\overline{Q}^*_{45} &= (Q^*_{44} - Q^*_{55})\sin\theta\cos\theta \\
\overline{Q}^*_{55} &= Q^*_{44}\sin^2\theta + Q^*_{55}\cos^2\theta \\
\overline{Q}^*_{66} &= (Q^*_{11} + Q^*_{22} - 2Q^*_{12} - 2Q^*_{66})\sin^2\theta\cos^2\theta + Q^*_{66}(\sin^4\theta + \cos^4\theta) \\
\overline{Q}^*_{14} &= \overline{Q}^*_{15} = \overline{Q}^*_{24} = \overline{Q}^*_{25} = \overline{Q}^*_{34} = \overline{Q}^*_{35} = \overline{Q}^*_{46} = \overline{Q}^*_{56} = 0
\end{aligned} \tag{2.42}$$

or

$$[\overline{Q}^*] = [T]^{-1}[Q^*][T]^{-T} \tag{2.43}$$

Similarly,

$$\begin{Bmatrix} \alpha_x^* \\ \alpha_y^* \\ \alpha_{xy}^* \end{Bmatrix} = \begin{bmatrix} \cos^2\theta & \sin^2\theta & -\cos\theta\sin\theta \\ \sin^2\theta & \cos^2\theta & \cos\theta\sin\theta \\ 2\cos\theta\sin\theta & -2\cos\theta\sin\theta & \cos^2\theta - \sin^2\theta \end{bmatrix} \begin{Bmatrix} \alpha_1^* \\ \alpha_2^* \\ 0 \end{Bmatrix} \tag{2.44}$$

2.4 Constitutive Relations and Resultant Laminate Forces and Moments

Consider a thin composite lamina; for example, graphite-epoxy, having an arbitrary orientation angle θ and with SMA fibers embedded in the same direction as the graphite fibers. The stress-strain relations for such a lamina in the principal material directions are derived in Section 2.3. The stress-strain relations for a general k-th layer with an orientation angle θ, become

$$\{\sigma\}_k - \{\sigma_o\}_k = \left[\overline{Q^*}\right]_k \begin{Bmatrix} \varepsilon_x \\ \varepsilon_y \\ \gamma_{xy} \end{Bmatrix} + \begin{Bmatrix} \sigma_x^* \\ \sigma_y^* \\ \tau_{xy}^* \end{Bmatrix}_k v_{sk} - \left(\left[\overline{Q}\right]_m \begin{Bmatrix} \alpha_x \\ \alpha_y \\ \alpha_{xy} \end{Bmatrix}_m v_m \right)_k \Delta T, T > T_s \tag{2.45}$$

and

$$\{\sigma\}_k - \{\sigma_o\}_k = \left[\overline{Q^*}\right]_k \left(\begin{Bmatrix} \varepsilon_x \\ \varepsilon_y \\ \gamma_{xy} \end{Bmatrix} - \begin{Bmatrix} \alpha_x^* \\ \alpha_y^* \\ \alpha_{xy}^* \end{Bmatrix}_k \Delta T \right), \qquad T < T_s \tag{2.46}$$

$$\{\tau\}_k - \{\tau_o\}_k = \begin{bmatrix} \overline{Q_{44}^*} & \overline{Q_{45}^*} \\ \overline{Q_{45}^*} & \overline{Q_{55}^*} \end{bmatrix}_k \begin{Bmatrix} \gamma_{yz} \\ \gamma_{xz} \end{Bmatrix} = [\overline{Q_s^*}]_k \{\gamma\} \tag{2.47}$$

where $[\overline{Q^*}]$, $[\overline{Q_s^*}]$ and $[\overline{Q}]_m$ are the transformed reduced stiffness matrices of the composite lamina and the composite matrix, and $\{\sigma_o\}$ and $\{\tau_o\}$ are the initial stress vectors, respectively.

The resultant force and moment vectors of the SMA fiber-reinforced composite plate are defined as

$$\begin{aligned} (\{N\},\{M\}) &= \int_{-h/2}^{h/2} \{\sigma\}_k (1,z) dz \\ \{R\} &= \int_{-h/2}^{h/2} \begin{Bmatrix} \tau_{yz} \\ \tau_{xz} \end{Bmatrix}_k dz \end{aligned} \tag{2.48}$$

or

$$\begin{aligned} \begin{Bmatrix} N \\ M \end{Bmatrix} &= \begin{bmatrix} A^* & B^* \\ B^* & D^* \end{bmatrix} \begin{Bmatrix} \varepsilon^o \\ \kappa \end{Bmatrix} + \begin{Bmatrix} N_r^* \\ M_r^* \end{Bmatrix} - \begin{Bmatrix} N_{\Delta T} \\ M_{\Delta T} \end{Bmatrix} + \begin{Bmatrix} N_\sigma \\ M_\sigma \end{Bmatrix} \\ \{R\} &= [A_s^*]\{\gamma\} + \{R_\sigma\} \end{aligned} \tag{2.49}$$

where the laminate stiffness [A*], [B*], [D*] and shear stiffness $[A_s^*]$ are all temperature dependent. The elements of these matrices, assuming midplane as the reference surface, are defined as

$$A_{ij}^* = \int_{-h/2}^{h/2} (\overline{Q_{ij}^*})_k dz, \qquad i,j = 1,2,6$$

$$B_{ij}^* = \int_{-h/2}^{h/2} (\overline{Q_{ij}^*})_k z dz, \qquad i,j = 1,2,6$$

$$D_{ij}^{*} = \int_{-h/2}^{h/2} (\overline{Q_{ij}^{*}})_k z^2 dz, \qquad i,j = 1,2,6$$

$$A_{sij}^{*} = \int_{-h/2}^{h/2} (\overline{Q_{sij}^{*}})_k dz, \qquad i,j = 4,5 \qquad (2.50)$$

The recovery in-plane force $\{N_r^*\}$ and moment $\{M_r^*\}$ vectors are dependent on temperature and prestrain (see Fig. 1.3). The vectors $\{N_\sigma\}$, $\{M_\sigma\}$ and $\{R_\sigma\}$ are the force, moment, and shear force vectors due to initial stress $\{\sigma_o\}$, respectively. The recovery and the thermal in-plane forces and moments due to the SMA recovery stress and the temperature change, respectively, are

$$\left(\{N_r^*\},\{M_r^*\}\right) = \int_{-h/2}^{h/2} \begin{Bmatrix} \sigma_x^* \\ \sigma_y^* \\ \tau_{xy}^* \end{Bmatrix}_k v_{sk}(1,z)dz, \qquad T > T_s$$
$$= 0 \qquad\qquad T < T_s \qquad (2.51)$$

$$\left(\{N_{\Delta T}\},\{M_{\Delta T}\}\right) = \int_{-h/2}^{h/2} \left(\left[\overline{Q}\right]_m \begin{Bmatrix} \alpha_x \\ \alpha_y \\ \alpha_{xy} \end{Bmatrix}_m v_m \right)_k \Delta T(1,z)dz, \qquad T > T_s \qquad (2.52)$$

$$\left(\{N_{\Delta T}\},\{M_{\Delta T}\}\right) = \int_{-h/2}^{h/2} \left(\left[\overline{Q^*}\right] \begin{Bmatrix} \alpha_x^* \\ \alpha_y^* \\ \alpha_{xy}^* \end{Bmatrix} \right)_k \Delta T(1,z)dz, \qquad T < T_s \qquad (2.53)$$

2.5 The Principle of Virtual Work

The virtual work done by internal and external forces is written as

$$\delta W_{int} = \int_a (\{\delta\varepsilon^o\}^T \{N\} + \{\delta\kappa\}^T \{M\} + \beta\{\delta\gamma\}^T \{R\}) dA \qquad (2.54)$$

and

$$\delta W_{ext} = \int_A [\delta w(p(x,y,t) - \rho h w_{,tt}) + \delta u(-\rho h u_{,tt}) + \delta v(-\rho h v_{,tt})] dA \qquad (2.55)$$

where *p(x, y, t)* is the external force, ρ is the mass density of the laminate and β is a shear correction factor which is defined later.

As mentioned in Section 2.3, superscript (*) indicates temperature dependent. The laminate stiffness [A*], [B*], [D*] and $[A_s^*]$ are all temperature dependent. In the following deductive procedure, the (*) is dropped for convenience. The virtual in-plane strains, curvature and shear strains can be expressed as

$$\{\varepsilon_b^o\} = \frac{1}{2}[\theta]\{G\}, \qquad \{\delta\varepsilon_b^o\} = \frac{1}{2}\delta([\theta]\{G\}) = [\theta]\{\delta G\} \tag{2.56}$$

$$\begin{aligned}\{\delta\varepsilon^o\} = {} & \{\delta w_m\}^T[C_m]^T + \{\delta w_b\}^T[C_{\psi b}]^T[\theta]^T + \{\delta\psi\}^T[C_{\psi\psi}]^T[\theta]^T \\ & + \{\delta w_b\}^T[C_{\psi b}]^T[\theta_o]^T + \{\delta\psi\}^T[C_{\psi\psi}]^T[\theta_o]^T\end{aligned} \tag{2.57}$$

$$\begin{aligned}\{N\} & = [A]\{\varepsilon^o\} + [B]\{\kappa\} - \{N_{\Delta T}\} + \{N_r^*\} + \{N_\sigma\} \\ & = [A][C_m]\{w_m\} + \frac{1}{2}[A][\theta]([C_{\psi b}]\{w_b\} + [C_{\psi\psi}]\{\psi\}) + [A][\theta][C_{\psi b}]\{w_{bo}\} \\ & + [A][\theta][C_{\psi\psi}]\{\psi_o\} + [B][C_b]\{\psi\} - \{N_{\Delta T}\} + \{N_r^*\} + \{N_\sigma\}\end{aligned} \tag{2.58}$$

$$\{\delta\kappa\}^T = \{\delta\psi\}^T[C_b]^T \tag{2.59}$$

$$\begin{aligned}\{M\} & = [B]\{\varepsilon^o\} + [D]\{\kappa\} - \{M_{\Delta T}\} + \{M_r^*\} + \{M_\sigma\} \\ & = [B][C_m]\{w_m\} + \frac{1}{2}[B][\theta]([C_{\psi b}]\{w_b\} + [C_{\psi\psi}]\{\psi\}) + [B][\theta][C_{\psi b}]\{w_{bo}\} \\ & + [B][\theta][C_{\psi\psi}]\{\psi_o\} + [D][C_b]\{\psi\} - \{M_{\Delta T}\} + \{M_r^*\} + \{M_\sigma\}\end{aligned} \tag{2.60}$$

$$\{\delta\gamma\}^T = \{\delta w_b\}^T[C_{\gamma b}]^T + \{\delta\psi\}^T[C_{\gamma\psi}]^T \tag{2.61}$$

$$\{R\} = [A_s][C_{\gamma b}]\{w_b\} + [A_s][C_{\gamma\psi}]\{\psi\} + \{R_\sigma\} \tag{2.62}$$

The virtual work principle gives

$$\delta W_{int} = \delta W_{ext} \tag{2.63}$$

where after substituting the appropriate expressions the following results are obtained:

$$
\begin{aligned}
&\delta W_{\text{int}} = \\
&\int_A (\{\delta\varepsilon^o\}^T\{N\} + \{\delta\kappa\}^T\{M\} + \beta\{\delta\gamma\}^T\{R\})dA \\
&= \int_A \{\{\delta w_m\}^T[C_m]^T([A][C_m]\{w_m\} + \frac{1}{2}[A][\theta][C_{\psi b}]\{w_b\} + \frac{1}{2}[A][\theta][C_{\psi\psi}]\{\psi\} \\
&+[A][\theta][C_{\psi b}]\{w_{bo}\} + [A][\theta][C_{\psi\psi}]\{\psi_o\} + [B][C_b]\{\psi\} - \{N_{\Delta T}\} + \{N_r^*\} + \{N_\sigma\}) \\
&+\{\delta w_b\}^T[C_{\psi b}]^T[\theta]^T([A][C_m]\{w_m\} + \frac{1}{2}[A][\theta][C_{\psi b}]\{w_b\} + \frac{1}{2}[A][\theta][C_{\psi\psi}]\{\psi\} \\
&+[A][\theta][C_{\psi b}]\{w_{bo}\} + [A][\theta][C_{\psi\psi}]\{\psi_o\} + [B][C_b]\{\psi\} - \{N_{\Delta T}\} + \{N_r^*\} + \{N_\sigma\}) \\
&+\{\delta\psi\}^T[C_{\psi\psi}]^T[\theta]^T([A][C_m]\{w_m\} + \frac{1}{2}[A][\theta][C_{\psi b}]\{w_b\} + \frac{1}{2}[A][\theta][C_{\psi\psi}]\{\psi\} \\
&+[A][\theta][C_{\psi b}]\{w_{bo}\} + [A][\theta][C_{\psi\psi}]\{\psi_o\} + [B][C_b]\{\psi\} - \{N_{\Delta T}\} + \{N_r^*\} + \{N_\sigma\}) \\
&+\{\delta w_b\}^T[C_{\psi b}]^T[\theta_o]^T([A][C_m]\{w_m\} + \frac{1}{2}[A][\theta][C_{\psi b}]\{w_b\} + \frac{1}{2}[A][\theta][C_{\psi\psi}]\{\psi\} \\
&+[A][\theta][C_{\psi b}]\{w_{bo}\} + [A][\theta][C_{\psi\psi}]\{\psi_o\} + [B][C_b]\{\psi\} - \{N_{\Delta T}\} + \{N_r^*\} + \{N_\sigma\}) \\
&+\{\delta\psi\}^T[C_{\psi\psi}]^T[\theta_o]^T([A][C_m]\{w_m\} + \frac{1}{2}[A][\theta][C_{\psi b}]\{w_b\} + \frac{1}{2}[A][\theta][C_{\psi\psi}]\{\psi\} \\
&+[A][\theta][C_{\psi b}]\{w_{bo}\} + [A][\theta][C_{\psi\psi}]\{\psi_o\} + [B][C_b]\{\psi\} - \{N_{\Delta T}\} + \{N_r^*\} + \{N_\sigma\}) \\
&+\{\delta\psi\}^T[C_b]^T([B][C_m]\{w_m\} + \frac{1}{2}[B][\theta][C_{\psi b}]\{w_b\} + \frac{1}{2}[B][\theta][C_{\psi\psi}]\{\psi\} \\
&+[B][\theta][C_{\psi b}]\{w_{bo}\} + [B][\theta][C_{\psi\psi}]\{\psi_o\} + [D][C_b]\{\psi\} - \{M_{\Delta T}\} + \{M_r^*\} + \{M_\sigma\}) \\
&+\beta\{\delta w_b\}^T[C_{\gamma b}]^T([A_s][C_{\gamma b}]\{w_b\} + [A_s][C_{\gamma\psi}]\{\psi\} + \{R_\sigma\}) \\
&+\beta\{\delta\psi\}^T[C_{\gamma\psi}]^T([A_s][C_{\gamma b}]\{w_b\} + [A_s][C_{\gamma\psi}]\{\psi\} + \{R_\sigma\})\}dA
\end{aligned}
\tag{2.64}
$$

and

$$
\begin{aligned}
&\delta W_{ext} = \int_A [\delta w(p(x,y,t) - \rho h w_{,tt}) + \delta u(-\rho h u_{,tt}) + \delta v(-\rho h v_{,tt})]dA \\
&= \int_A \{(\{\delta w_b\}^T\{H_w\} + \{\delta\psi\}^T\{H_{w\psi}\})(p(x,y,t) - \rho h([H_w]\{\ddot{w}_b\} + \{H_{w\psi}\}\{\ddot{\psi}\})) \\
&- \rho h\{\delta w_m\}^T(\{H_u\}[H_u]\{\ddot{w}_m\}) - \rho h(\delta w_m\}^T(\{H_v\}[H_v]\{\ddot{w}_m\})\}dA
\end{aligned}
\tag{2.65}
$$

2.6 Element Equation of Motion and System Finite Element Equation

Using virtual work principle Eqs. (2.54), (2.55), (2.63), the equation of motion for the MIN3 plate element can be derived as

$$
\begin{aligned}
&\begin{bmatrix} [m]_b & [m]_{b\psi} & 0 \\ [m]_{\psi b} & [m]_{\psi} & 0 \\ 0 & 0 & [m]_m \end{bmatrix}
\begin{Bmatrix} \ddot{w}_b \\ \ddot{\psi} \\ \ddot{w}_m \end{Bmatrix}
+\left(\begin{bmatrix} 0 & 0 & 0 \\ 0 & [k]_{\psi} & [k]_{\psi m} \\ 0 & [k]_{m\psi} & [k]_m \end{bmatrix}
+\begin{bmatrix} [k_o]_b & [k_o]_{b\psi} & [k_o]_{bm} \\ [k_o]_{\psi b} & [k_o]_{\psi} & [k_o]_{\psi m} \\ [k_o]_{mb} & [k_o]_{m\psi} & 0 \end{bmatrix}\right)
\begin{Bmatrix} w_b \\ \psi \\ w_m \end{Bmatrix} \\
&-\left(\begin{bmatrix} [k_{N\Delta T}]_b & [k_{N\Delta T}]_{b\psi} & 0 \\ [k_{N\Delta T}]_{\psi b} & [k_{N\Delta T}]_{\psi} & 0 \\ 0 & 0 & 0 \end{bmatrix}
-\begin{bmatrix} [k_r^*]_b & [k_r^*]_{b\psi} & 0 \\ [k_r^*]_{\psi b} & [k_r^*]_{\psi} & 0 \\ 0 & 0 & 0 \end{bmatrix}
-\begin{bmatrix} [k_\sigma]_b & [k_\sigma]_{b\psi} & 0 \\ [k_\sigma]_{\psi b} & [k_\sigma]_{\psi} & 0 \\ 0 & 0 & 0 \end{bmatrix}\right)
\begin{Bmatrix} w_b \\ \psi \\ w_m \end{Bmatrix} \\
&+\left(\frac{1}{2}\begin{bmatrix} [n1_o]_b & [n1_o]_{b\psi} & 0 \\ [n1_o]_{\psi b} & [n1_o]_{\psi} & 0 \\ 0 & 0 & 0 \end{bmatrix}
+\beta\begin{bmatrix} [k_s]_b & [k_s]_{b\psi} & 0 \\ [k_s]_{\psi b} & [k_s]_{\psi} & 0 \\ 0 & 0 & 0 \end{bmatrix}\right)
\begin{Bmatrix} w_b \\ \psi \\ w_m \end{Bmatrix} \\
&+\frac{1}{2}\left(\begin{bmatrix} [n1_{Nm}]_b & [n1_{Nm}]_{b\psi} & 0 \\ [n1_{Nm}]_{\psi b} & [n1_{Nm}]_{\psi} & 0 \\ 0 & 0 & 0 \end{bmatrix}
+\begin{bmatrix} [n1_{Nb}]_b & [n1_{Nb}]_{b\psi} & 0 \\ [n1_{Nb}]_{\psi b} & [n1_{Nb}]_{\psi} & 0 \\ 0 & 0 & 0 \end{bmatrix}
+\begin{bmatrix} 0 & [n1_l]_{b\psi} & [n1_l]_{bm} \\ [n1_l]_{\psi b} & [n1_l]_{\psi} & [n1_l]_{\psi m} \\ [n1_l]_{mb} & [n1_l]_{m\psi} & 0 \end{bmatrix}\right)
\begin{Bmatrix} w_b \\ \psi \\ w_m \end{Bmatrix} \\
&+\frac{1}{3}\begin{bmatrix} [n2]_b & [n2]_{b\psi} & 0 \\ [n2]_{\psi b} & [n2]_{\psi} & 0 \\ 0 & 0 & 0 \end{bmatrix}
\begin{Bmatrix} w_b \\ \psi \\ w_m \end{Bmatrix} \\
&=\begin{Bmatrix} \{p_p(t)\}_b \\ \{p_p(t)\}_{\psi} \\ 0 \end{Bmatrix}
+\begin{Bmatrix} 0 \\ \{p_{\Delta T}\}_{\psi} \\ \{p_{\Delta T}\}_m \end{Bmatrix}
-\begin{Bmatrix} 0 \\ \{p_r^*\}_{\psi} \\ \{p_r^*\}_m \end{Bmatrix}
-\begin{Bmatrix} 0 \\ \{p_\sigma\}_{\psi} \\ \{p_\sigma\}_m \end{Bmatrix}
-\beta\begin{Bmatrix} \{p_\tau\}_b \\ \{p_\tau\}_{\psi} \\ 0 \end{Bmatrix}
+\begin{Bmatrix} \{p_{\Delta To}\}_b \\ \{p_{\Delta To}\}_{\psi} \\ 0 \end{Bmatrix}
-\begin{Bmatrix} \{p_{ro}^*\}_b \\ \{p_{ro}^*\}_{\psi} \\ 0 \end{Bmatrix}
-\begin{Bmatrix} \{p_{\sigma o}\}_b \\ \{p_{\sigma o}\}_{\psi} \\ 0 \end{Bmatrix}
\end{aligned}
\tag{2.66}
$$

or in the compact form

$$
\begin{aligned}
&[m]\{\ddot{w}\}+([k]+[k_o]-[k_{N\Delta T}]+[k_r^*]+[k_\sigma]+\tfrac{1}{2}[n1_o]+\beta[k_s])\{w\} \\
&+\tfrac{1}{2}([n1_{Nm}]+[n1_{Nb}]+[n1_l])\{w\}+\tfrac{1}{3}[n2]\{w\} \qquad (2.67) \\
&=\{p_p(t)\}+\{p_{\Delta T}\}-\{p_r^*\}-\{p_\sigma\}-\{p_\tau\}+\{p_{\Delta To}\}-\{p_{ro}^*\}-\{p_{\sigma o}\}
\end{aligned}
$$

where [m], [k] and {p} denote the element mass, linear stiffness matrices and load vector, respectively, and $[n1_o]$, $[n1_{Nm}]$, $[n1_{Nb}]$, $[n1_l]$ and [n2] denote the first- and second-order nonlinear stiffness matrices, respectively. The subscripts b, ψ and m denote the transverse, rotation and in-plane components, respectively. The subscripts s, τ, o, σ, r, NΔT and ΔT, Nm, Nb, l and p denote the stiffness matrices and load vectors which are related to transverse shear, initial shear stress $\{\tau_o\}$, $w_o(x,y)$, $\{\sigma_o\}$, $\{\sigma_r^*\}$, $\{N_{\Delta T}\}$ and ΔT, $\{N_m\}(=[A]\{\varepsilon_m^o\})$, $\{N_b\}(=[B]\{\kappa\})$, and distributed load p(x, y, t), respectively. The shear correction factor is defined as [62]

$$\beta=\frac{1}{1+0.5\dfrac{\sum\limits_{i=4,9}k_{sii}}{\sum\limits_{i=4,9}k_{bii}}} \qquad (2.68)$$

It is assumed that the rotary inertia effect is negligible for relatively thin plate (a/h>50). The expressions for element linear and nonlinear stiffness and mass matrices and load vectors are given in Appendix B.

Summing or assembly of the contributions from all elements (matrices with lower case letter) results in the global matrices (denoted by capital letter). The system finite element equations after applying the kinematic boundary conditions can be written as

$$\begin{bmatrix} [M]_b & [M]_{b\psi} & 0 \\ [M]_{\psi b} & [M]_{\psi} & 0 \\ 0 & 0 & [M]_m \end{bmatrix} \begin{Bmatrix} \ddot{W}_b \\ \ddot{\Psi} \\ \ddot{W}_m \end{Bmatrix} + \left(\begin{bmatrix} 0 & 0 & 0 \\ 0 & [K]_{\psi} & [K]_{\psi m} \\ 0 & [K]_{m\psi} & [K]_m \end{bmatrix} + \begin{bmatrix} [K_o]_b & [K_o]_{b\psi} & [K_o]_{bm} \\ [K_o]_{\psi b} & [K_o]_{\psi} & [K_o]_{\psi m} \\ [K_o]_{mb} & [K_o]_{m\psi} & 0 \end{bmatrix} \right) \begin{Bmatrix} W_b \\ \Psi \\ W_m \end{Bmatrix}$$

$$- \left(\begin{bmatrix} [K_{N\Delta T}]_b & [K_{N\Delta T}]_{b\psi} & 0 \\ [K_{N\Delta T}]_{\psi b} & [K_{N\Delta T}]_{\psi} & 0 \\ 0 & 0 & 0 \end{bmatrix} - \begin{bmatrix} [K_r^*]_b & [K_r^*]_{b\psi} & 0 \\ [K_r^*]_{\psi b} & [K_r^*]_{\psi} & 0 \\ 0 & 0 & 0 \end{bmatrix} - \begin{bmatrix} [K_\sigma]_b & [K_\sigma]_{b\psi} & 0 \\ [K_\sigma]_{\psi b} & [K_\sigma]_{\psi} & 0 \\ 0 & 0 & 0 \end{bmatrix} \right) \begin{Bmatrix} W_b \\ \Psi \\ W_m \end{Bmatrix}$$

$$+ \left(\frac{1}{2} \begin{bmatrix} [N1_o]_b & [N1_o]_{b\psi} & 0 \\ [N1_o]_{\psi b} & [N1_o]_{\psi} & 0 \\ 0 & 0 & 0 \end{bmatrix} + \begin{bmatrix} [K_s]_b & [K_s]_{b\psi} & 0 \\ [K_s]_{\psi b} & [K_s]_{\psi} & 0 \\ 0 & 0 & 0 \end{bmatrix} \right) \begin{Bmatrix} W_b \\ \Psi \\ W_m \end{Bmatrix}$$

$$+ \frac{1}{2} \left(\begin{bmatrix} [N1_{Nm}]_b & [N1_{Nm}]_{b\psi} & 0 \\ [N1_{Nm}]_{\psi b} & [N1_{Nm}]_{\psi} & 0 \\ 0 & 0 & 0 \end{bmatrix} + \begin{bmatrix} [N1_{Nb}]_b & [N1_{Nb}]_{b\psi} & 0 \\ [N1_{Nb}]_{\psi b} & [N1_{Nb}]_{\psi} & 0 \\ 0 & 0 & 0 \end{bmatrix} \right) \begin{Bmatrix} W_b \\ \Psi \\ W_m \end{Bmatrix}$$

$$+ \frac{1}{2} \begin{bmatrix} 0 & [N1_l]_{b\psi} & [N1_l]_{bm} \\ [N1_l]_{\psi b} & [N1_l]_{\psi} & [N1_l]_{\psi m} \\ [N1_l]_{mb} & [N1_l]_{m\psi} & 0 \end{bmatrix} \begin{Bmatrix} W_b \\ \Psi \\ W_m \end{Bmatrix} + \frac{1}{3} \begin{bmatrix} [N2]_b & [N2]_{b\psi} & 0 \\ [N2]_{\psi b} & [N2]_{\psi} & 0 \\ 0 & 0 & 0 \end{bmatrix} \begin{Bmatrix} W_b \\ \Psi \\ W_m \end{Bmatrix}$$

$$= \begin{Bmatrix} \{P_p(t)\}_b \\ \{P_p(t)\}_{\psi} \\ 0 \end{Bmatrix} + \begin{Bmatrix} 0 \\ \{P_{\Delta T}\}_{\psi} \\ \{P_{\Delta T}\}_m \end{Bmatrix} - \begin{Bmatrix} 0 \\ \{P_r^*\}_{\psi} \\ \{P_r^*\}_m \end{Bmatrix} - \begin{Bmatrix} 0 \\ \{P_\sigma\}_{\psi} \\ \{P_\sigma\}_m \end{Bmatrix} - \begin{Bmatrix} \{P_\tau\}_b \\ \{P_\tau\}_{\psi} \\ 0 \end{Bmatrix} + \begin{Bmatrix} \{P_{\Delta To}\}_b \\ \{P_{\Delta To}\}_{\psi} \\ 0 \end{Bmatrix} - \begin{Bmatrix} \{P_{ro}^*\}_b \\ \{P_{ro}^*\}_{\psi} \\ 0 \end{Bmatrix} - \begin{Bmatrix} \{p_{\sigma o}\}_b \\ \{P_{\sigma o}\}_{\psi} \\ 0 \end{Bmatrix} \tag{2.69}$$

or it can be written as

$$\begin{aligned} &\{\Phi(W,\ddot{W})\} \\ &= [M]\{\ddot{W}\} + ([K]+[K_o]-[K_{N\Delta T}]+[K_r^*]+[K_\sigma]+[K_s])\{W\} \\ &+ \tfrac{1}{2}[N1]\{W\} + \tfrac{1}{3}[N2]\{W\} \\ &- \{P_p(t)\} - \{P_{\Delta T}\} + \{P_r^*\} + \{P_\sigma\} + \{P_\tau\} - \{P_{\Delta To}\} + \{P_{ro}^*\} + \{P_{\sigma o}\} \\ &= 0 \end{aligned} \tag{2.70}$$

where $\{W\}^T = [W_b, \Psi, W_m]$ and the other subscripts have been specified. The transverse shear $[K_s]$ and the first order nonlinear [N1] stiffness matrices can be written in the form as

$$[K_s] = \sum_{\substack{\text{assembly+}\\ \text{boundary}\\ \text{condition}}} (\beta[k_s]) \tag{2.71}$$

$$[N1] = \sum_{\substack{\text{assembly+}\\ \text{boundary}\\ \text{condition}}} ([n1_{Nm}] + [n1_{Nb}] + [n1_l] + [n1_o]) \tag{2.72}$$

CHAPTER III

SOLUTION PROCEDURE

In this chapter, the governing equations for the four types of analyses are derived from the system equations of motion, Eq. (2.70), and they are solved in sequence. The four types of analyses are: 1) thermal buckling; 2) thermal postbuckling deflection; 3) vibration of buckled plate, and 4) random response about the buckled position.

3.1 Static and Dynamic Equations

The system of equations, Eq. (2.70), is a set of nonlinear ordinary differential equations with respect to time t. A novel solution procedure is presented in the following to determine thermal postbuckling deflection and random vibration of thermally buckled composite plates with embedded SMA fibers. The solution of a set of differential equations, Eq. (2.70), is thus assumed as the sum of a time-dependent solution and a time-independent solution, that is

$$\{W\} = \{W\}_s + \{W(t)\}_t \tag{3.1}$$

where $\{W(t)\}_t$ is the time-dependent solution whose physical meaning is the small oscillations about the thermal postbuckled position $\{W\}_s$, where $\{W\}_s$ is the time-independent solution whose physical meaning is the large thermal postbuckled deflection. Substituting Eq. (3.1) into Eq. (2.70) and neglecting the higher order terms of $\{W(t)\}_t$ for small amplitude random vibration, the following two sets of equations are obtained as

$$\begin{aligned}&([K]+[K_o]-[K_{N\Delta T}]+[K_r^*]+[K_\sigma]+[K_s])\{W\}_s+\frac{1}{2}[N1]_s\{W\}_s+\frac{1}{3}[N2]_s\{W\}_s\\&=\{P_{\Delta T}\}-\{P_r^*\}-\{P_\sigma\}-\{P_\tau\}+\{P_{\Delta To}\}-\{P_{ro}^*\}-\{P_{\sigma o}\}\end{aligned} \tag{3.2}$$

and

$$\begin{aligned}&[M]\{\ddot{W}\}_t + ([K]+[K_o]-[K_{N\Delta T}]+[K_r^*]+[K_\sigma]+[K_s])\{W\}_t + [N1]_s\{W\}_t + [N2]_s\{W\}_t \\ &= \{P_p(t)\}\end{aligned} \tag{3.3}$$

where the nonlinear stiffness matrices, $[N1]_s$ and $[N2]_s$ depend linearly and quadratically upon the thermal static displacement $\{W\}_s$. The detailed derivations to obtain Eqs. (3.2) and (3.3) are given in Appendix C.

The total plate response is at any time t the sum of $\{W\}_s$ and $\{W\}_t$ according to Eqs. (2.70) and (3.1). A close examination of Eqs. (3.2) and (3.3) reveals three aspects of the solution process. First, Eq. (3.2) is a set of nonlinear algebraic equations which represents a time-independent solution for the governing equation, Eq. (2.70). Second, Eq. (3.3) is a set of linear differential equations which represents a time-dependent solution for the governing equation, Eq. (2.70). Finally, Eq. (3.2) has to be solved first to determine the thermal postbuckling deflection $\{W\}_s$. The dynamic response $\{W\}_t$ can be obtained from solving Eq. (3.3).

3.2 Increment Stability Equations

It is necessary to study the stability of the composite plates with embedded SMA because the temperature effects cause a stability problem in the plates. The adjacent-equilibrium criterion [63] can be used to investigate the stability of a given equilibrium configuration, $\{W_e\}$. For given small increments to the adjacent equilibrium position

$$\{W\}\rightarrow\{W_e\}+\{\Delta W\} \tag{3.4}$$

$\{\Phi(W_e+\Delta W)\}$ can be expanded by using a truncated Taylor series as

$$\begin{aligned}&\{\Phi(W_e+\Delta W)\} \\ &= \{\Phi(W_e)\} + \left[\tfrac{d\Phi}{dW}(W_e)\right]\{\Delta W\} \\ &= 0\end{aligned} \tag{3.5}$$

where the incremental quantities $\{\Delta W\}$ are arbitrarily small and $\{\Phi(W_e)\}$, Eq. (2.70), is in an equilibrium configuration. From Eq. (2.70), the total differential of $\{\Phi(W)\}$ is

$$\{d\Phi(W)\} = ([K]+[K_o]-[K_{N\Delta T}]+[K_r^*]+[K_\sigma]+[K_s])\{dW\}+d(\frac{1}{2}[N1]\{W\}+\frac{1}{3}[N2]\{W\}) \tag{3.6}$$

The term $d(\frac{1}{2}[N1]\{W\}+\frac{1}{3}[N2]\{W\})$ had been proven to have the following form [63]

$$d(\frac{1}{2}[N1]\{W\}+\frac{1}{3}[N2]\{W\}) = ([N1]+[N2])\{dW\} \tag{3.7}$$

Thus based on Taylor expansion, the stability equation for the system equation, Eq. (3.5) of equilibrium can be derived as

$$([K]+[K_o]-[K_{N\Delta T}]+[K_r^*]+[K_\sigma]+[K_s])\{\Delta W\}+([N1]_e+[N2]_e)\{\Delta W\} = 0 \tag{3.8}$$

or

$$[K_{tan}]_e\{\Delta W\} = 0 \tag{3.9}$$

where the tangent stiffness matrix $[K_{tan}]_e$ is

$$[K_{tan}]_e = ([K]+[K_o]-[K_{N\Delta T}]+[K_r^*]+[K_\sigma]+[K_s]+[N1]_e+[N2]_e)$$

and the tangent stiffness matrix $[K_{tan}]_e$, $[N1]_e$ and $[N2]_e$ are evaluated at the equilibrium configuration $\{W\}_e$.

3.3 Thermal Buckling

A linear thermal buckling analysis is carried out first to determine the critical buckling temperature $T_{cr} = \Delta T_{cr} + T_o$, where T_o is the reference or ambient temperature. Equations governing the thermal buckling are obtained by first neglecting the extension-bending coupling, the nonlinear bending force, the initial deflection and the initial stress terms from Eq. (3.8), thereby giving

$$([K_b]-[K_{N\Delta T}]+[K_r^*]+[N1_{Nm}]_e+[K_s]_b)\begin{Bmatrix}\Delta W_b \\ \Delta\Psi\end{Bmatrix}=0 \tag{3.10}$$

Furthermore, from the linear system equation in membrane (see Eqs. (2.69) and (3.2)), the following relationship is established

$$[K_m]\{W_m\}=\{P_{\Delta T}\}_m-\{P_r^*\}_m \tag{3.11}$$

where

$$[K_b]=\begin{bmatrix}0 & 0 \\ 0 & K_\psi\end{bmatrix}, \qquad [K_s]_b=\begin{bmatrix}K_{sb} & K_{sb\psi} \\ K_{s\psi b} & K_{s\psi}\end{bmatrix}$$

The first-order nonlinear stiffness matrix $[N1_{Nm}]_e$ is linearly dependent upon the in-plane displacement $\{W_e\}$ which can be expressed from Eq. (3.11) at a given ΔT(x, y) as

$$\begin{aligned}\{W_m\}&=[K_m]^{-1}(\{P_{\Delta T}\}_m-\{P_r^*\}_m)\\&=\{W_m(\Delta T)\}-\{W_m\}_c\end{aligned} \tag{3.12}$$

where $\{W_m(\Delta T)\}=[K_m]^{-1}\{P_{\Delta T}\}_m$ is linearly dependent upon ΔT, and $\{W_m\}_c=[K_m]^{-1}\{P_r^*\}_m$ is a constant vector, and it is independent of temperature change. Thus the matrix $[N1_{Nm}]_e$ is the difference of two matrices. The first matrix $[N1_{Nm}]_{\Delta T}$, which is linearly dependent upon ΔT, is evaluated with $\{W_m(\Delta T)\}$, and the second matrix $[N1_{Nm}]_c$, which is a constant matrix and independent of temperature change, is evaluated with $\{W_m\}_c$ as

$$[N1_{Nm}]_e=[N1_{Nm}]_{\Delta T}-[N1_{Nm}]_c \tag{3.13}$$

Since both matrices $[K_{N\Delta T}]$ and $[N1_{Nm}]_{\Delta T}$ depend linearly upon ΔT, Eq. (3.10) can be expressed as an eigen-problem

$$([K_b]+[K_r^*]-[N1_{Nm}]_c+[K_s]_b)\{\phi\}=\lambda([K_{N\Delta T}]-[N1_{Nm}]_{\Delta T})\{\phi\} \tag{3.14}$$

The critical temperature change corresponds to the lowest eigenvalue λ and is given by $\Delta T_{cr} = \lambda \Delta T$, and {ϕ} is the corresponding thermal buckling mode. The following items are directed for special attention: 1) Since the matrices in Eq. (3.14) are all temperature dependent, an iterative scheme has to be implemented to achieve a converged ΔT_{cr} at $\lambda=1.000\pm0.001$; 2) For antisymmetric angle-ply and symmetrically laminated composite plates with non-zero thermal bending load, and unsymmetrically laminated composite plates, the solution from Eq. (3.14) is referred to as a reference critical temperature, $(\Delta T_{cr})_{ref}$.

3.4 Thermal Postbuckling/Deflection

Equation (3.5) is the governing equation to determine the thermal postbuckling or thermal deflection with a certain thermal load for $\Delta T > \Delta T_{cr}$ or $(\Delta T_{cr})_{ref}$, and it contains both temperature dependent material effects due to SMA and geometrical nonlinearity due to large thermal deflection. With consideration of nonlinear material properties of SMA, the incremental computational method is employed. That is, in each small temperature increment, the material properties of SMA are considered as constant. The initial deflection and stress are updated shown in Table 3.1.

Table 3.1 Incremental solution procedure for thermal deflection

Increment number	Initial deflection $\{W_o\}$	Initial stress $\{\sigma_o\}$	Newton-Raphson Process	Converged deflection $\{W\}$	Stress in increment $\{\sigma\}$
1	0	0	→	$\{W\}_1$	$\{\sigma\}_1$
2	$\{W\}_1$	$\{\sigma\}_1$	→	$\{W\}_2$	$\{\sigma\}_2$
3	$\{W\}_1+\{W\}_2$	$\{\sigma\}_1+\{\sigma\}_2$	→	$\{W\}_3$	$\{\sigma\}_3$
:	:	:	:	:	:
k	$\{W\}_1+...+\{W\}_{k-1}$	$\{\sigma\}_1+...+\{\sigma\}_{k-1}$	→	$\{W\}_k$	$\{\sigma\}_k$

With the consideration of large thermal deflection, the nonlinear stiffness matrices, $[N1]_s$ and $[N2]_s$, linearly and quadratically depend upon the thermal displacement. One effective approach involves the application of Newton-Raphson iterative method within each small temperature increment. Thus, for i-th iteration, the Newton form of Eq. (3.2) or Eq. (3.5) can be written as

$$[K_{tan}]_i(\{\Delta W\}_s)_{i+1} = \{\Delta P\}_i \tag{3.15}$$

then $[K_{tan}]_{i+1}$ and $\{\Delta P\}_{i+1}$ are updated by using

$$(\{W\}_s)_{i+1} = (\{W\}_s)_i + (\{\Delta W\}_s)_{i+1} \tag{3.16}$$

The solution process seeks to reduce the imbalance load vector $\{\Delta P\}$, and consequently $\{\Delta W\}_s$, to a specified small quantity (10^{-6}). The iteration tangent stiffness matrix and the imbalance load vector are

$$[K_{tan}]_i = [K] + [K_o] - [K_{N\Delta T}] + [K_r^*] + [K_\sigma] + [K_s] + [N1]_{si} + [N2]_{si} \tag{3.17}$$

and

$$\begin{aligned} \{\Delta P\}_i = {} & \{P_{\Delta T}\} - \{P_r^*\} - \{P_\sigma\} - \{P_\tau\} + \{P_{\Delta To}\} - \{P_{ro}^*\} - \{P_{\sigma o}\} \\ & - ([K] + [K_o] - [K_{N\Delta T}] + [K_r^*] + [K_\sigma] + [K_s])\{W\}_{si} \\ & - \frac{1}{2}[N1]_{si}\{W\}_{si} - \frac{1}{3}[N2]_{si}\{W\}_{si} \end{aligned} \tag{3.18}$$

The linear buckling mode shape, Eqs. (3.12) and (3.14), normalized by a scale factor for symmetric laminates, or the linear thermal deflection (by dropping the nonlinear terms) from Eq. (3.2) for unsymmetric laminates is usually taken to be the initial trial solution for Eq. (3.15). A flowchart for determining the thermal postbuckling deflection is shown in Fig. 3.2.

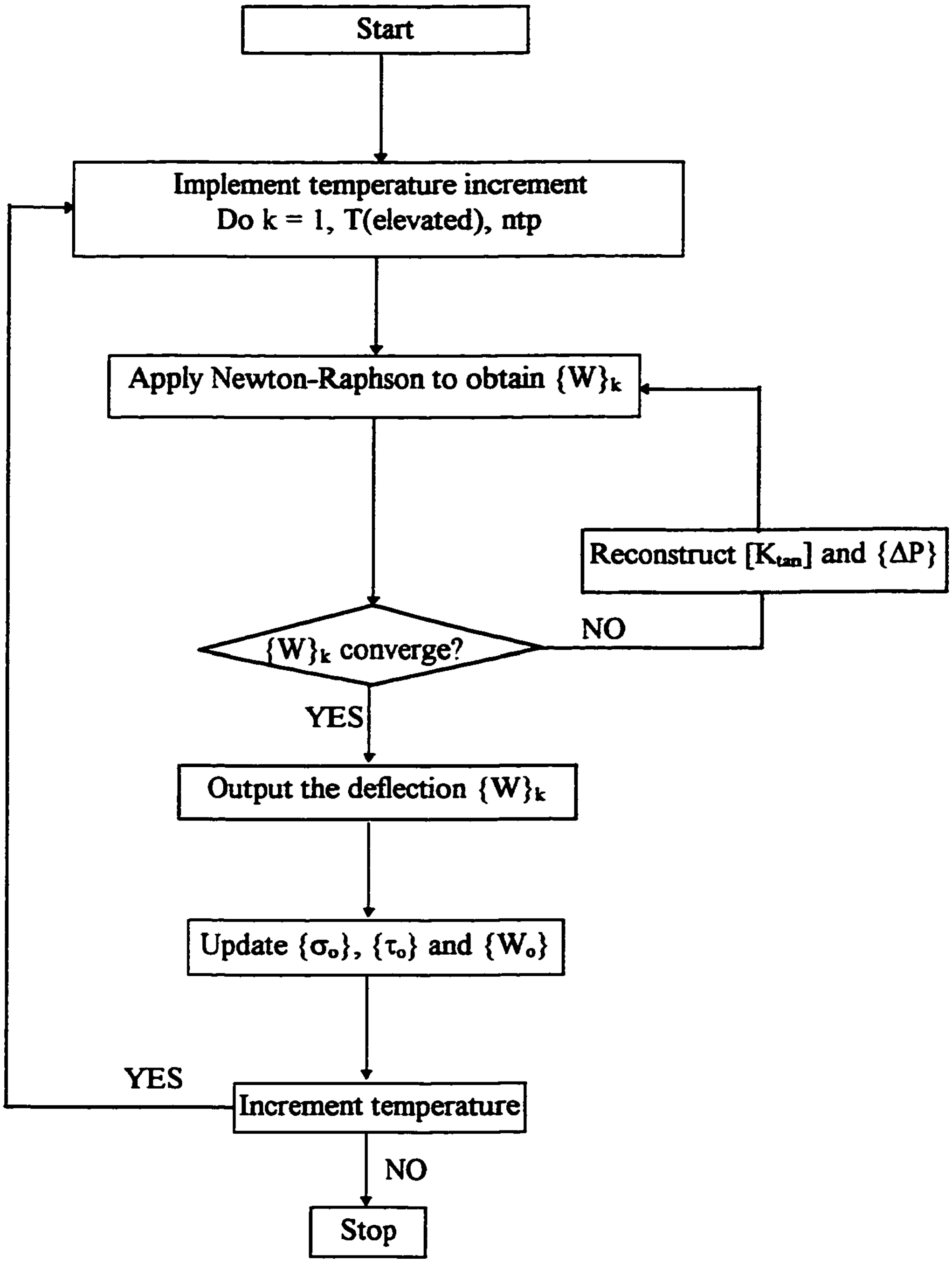

Fig. 3.2 Computational Method for Determining Thermal Deflection.

3.5 Vibration of Buckled/Deformed Plate

Equation (3.3) is the governing equation for dynamic response of composite plates with embedded SMA fibers. It can be seen that the converged tangent stiffness matrix $[K_{tan}]$ as shown in Eq. (3.17) is exactly identical to the sum of stiffness matrices in the dynamic equation, Eq. (3.3). Thus the vibration equation about the thermally buckled position $\{W\}_s$ becomes

$$[M]\{\ddot{W}\}_t + [K_{tan}]\{W\}_t = \{P_p(t)\} \tag{3.19}$$

This feature gives a great advantage of solving the dynamic equation, Eq. (3.19), only the mass matrix [M] needs to be formed. There is no need to assemble system stiffness matrices by considering the effects of SMA recovery stress, thermal stress and thermal deflection from each element using the conventional approach. The computational time is greatly reduced. For free vibration, dynamic equation, Eq. (3.19), is a generalized linear eigenvalue problem and can be written as

$$\omega_r^2[M]\{\phi_r\} = [K_{tan}]\{\phi_r\} \tag{3.20}$$

where ω_r and $\{\phi_r\}$ are the natural frequencies and mode shapes of vibration. Thus the natural frequencies of vibration and mode shapes about the thermally buckled/deformed position $\{W\}_s$ are obtained from the solution of Eq. (3.20).

3.6 Random Response of Buckled Plate

3.6.1 Random Displacement Response

The random displacement analysis of a thermally buckled plate with embedded SMA is performed to determine the root-mean-square (RMS) maximum deflection and power spectral density (PSD) functions. The dynamic equation is shown in Eq. (3.19), and the natural frequencies ω_r and mode shapes $\{\phi_r\}$ of vibration are obtained from the eigenvalue problem, Eq. (3.20). The truncated modal transformation form, using the lowest N modes, can be written in the following form

$$\{W\}_t = \sum_{r=1}^{N} \{\phi_r\} q_r = [\phi]\{q\} \tag{3.21}$$

Substituting Eq. (3.21) into Eq. (3.19) and considering the modal damping simultaneously, a set of uncoupled modal equations with reduced degrees of freedom can thus be derived as

$$\ddot{q}_r + 2\varsigma_r \omega_r \dot{q}_r + \omega_r^2 q_r = f_r, \quad r = 1,2,\ldots,N \tag{3.22}$$

where the modal mass, stiffness and force are

$$\begin{aligned} m_r &= \{\phi_r\}^T [M] \{\phi_r\} \\ k_r &= \{\phi_r\}^T [K_{\tan}] \{\phi_r\} \\ f_r &= \{\phi_r\}^T \{P_p(t)\} / m_r \end{aligned} \tag{3.23}$$

and ς_r is the modal damping ratio which can be obtained experimentally or estimated from similarly supported structures.

The plate is assumed to be subjected to Gaussian white noise uniform random load $P_p(t)$, the cross-correlation of modal amplitudes can be determined from Eq. (3.22) as

$$\begin{aligned} E[q_r q_s] &= \int_{-\infty}^{\infty} S_p(\omega) H_r(\omega) H_s(-\omega) d\omega \\ &= \int_0^{\infty} G_p(f) H_r(f) H_s(-f) df \end{aligned} \tag{3.24}$$

where $S_p(\omega)$ and $G_p(f)$ are the two-sided and one-sided spectral density functions of the uniformly distributed acoustic excitation $P_p(t)$, respectively, and the relation is

$$G_p(f) = 4\pi S_p(\omega), \qquad for\ \omega = 2\pi f \qquad (f \geq 0) \tag{3.25}$$

The one-sided spectral density function of the acoustic excitation $P_p(t)$ has a transformation from a sound spectral level (SSL) as

$$G_p(f) = 8.4216 \times 10^{(0.1 \times SSL - 18.0)} \tag{3.26}$$

where the unit for sound spectral level is dB and the unit for $G_p(f)$ is $(psi)^2/Hz$.

The complex frequency response function is

$$H_r(\omega) = \frac{1}{m_r(\omega_r^2 - \omega^2 + 2i\varsigma_r\omega_r\omega)} \tag{3.27}$$

The cross-correlation of modal amplitudes from Eq. (3.24) is

$$E[q_r q_s] = \frac{G_p(f)(\varsigma_r\omega_r + \varsigma_s\omega_s)}{m_r m_s\{(\omega_r^2 - \omega_s^2)^2 + 4[\varsigma_r\varsigma_s\omega_r\omega_s(\omega_r^2 + \omega_s^2) + (\varsigma_r^2 + \varsigma_s^2)\omega_r^2\omega_s^2]\}} \tag{3.28}$$

and the correlation matrix of the system nodal amplitude becomes

$$E[\{W\}_t\{W\}_t^T] = [\phi]E[\{q\}\{q\}^T][\phi]^T \tag{3.29}$$

The root-mean-square nodal deflection can be obtained from the diagonal value of the above correlation matrix, and the root-mean-square maximum deflection is determined from

$$RMS[W_{\max}^2] = \max.(\sqrt{E\left[(W_t)_j^2\right]}) \tag{3.30}$$

where $E[(W_t)_j^2]$ are the diagonal terms of Eq. (3.29).

The power/deflection spectrum density can be determined from the following equation

$$G_{q_r q_s} = G_p(f) H_r(f) H_s(-f)$$
$$[G_w] = [\phi][G_{q_r q_s}][\phi]^T \tag{3.31}$$

3.6.2 Random Strain Response

As the displacement random response is determined in Section 3.6.1 for a given combination of thermal and random loads, the element strains can be obtained using Eqs. (2.8), (2.9), (2.10) and (2.11). For a linear random vibration of thermally buckled plate, the strain-displacement relations can be expressed as

$$\{\varepsilon\} = \begin{Bmatrix} u_{,x} \\ v_{,y} \\ u_{,y} + v_{,x} \end{Bmatrix} + z \begin{Bmatrix} \psi_{y,x} \\ \psi_{x,y} \\ \psi_{y,y} + \psi_{x,x} \end{Bmatrix} = \{\varepsilon_m^o\} + z\{\kappa\}$$
$$= [C_m]\{w_m\} + z[C_b]\{\psi\} \tag{3.32}$$

$$\{\gamma\} = \begin{Bmatrix} \gamma_{yz} \\ \gamma_{xz} \end{Bmatrix} = \begin{Bmatrix} w_{,y} \\ w_{,x} \end{Bmatrix} + \begin{Bmatrix} \psi_x \\ \psi_y \end{Bmatrix}$$
$$= [C_{\gamma b}]\{w_b\} + [C_{\gamma\psi}]\{\psi\} \tag{3.33}$$

where the strain interpolation matrices $[C_m]$, $[C_b]$, $[C_{\gamma b}]$ *and* $[C_{\gamma\psi}]$ are defined in Appendix A.

By using truncated modal transformation, the modal equations for element strain can be derived as

$$\{\varepsilon\} = [C_m]\{w_m\} + z[C_b]\{\psi\} = \sum_{r=1}^{N} ([C_m]\{\phi_m\}_r + z[C_b]\{\phi_\psi\}_r) q_r$$
$$= \sum_{r=1}^{N} \{\varepsilon\}_r q_r \tag{3.34}$$

$$\begin{aligned}\{\gamma\} &= [C_{\gamma b}]\{w_b\} + [C_{\gamma\psi}]\{\psi\} = \sum_{r=1}^{N}([C_{\gamma b}]\{\phi_b\}_r + [C_{\gamma\psi}]\{\phi_\psi\}_r)q_r \\ &= \sum_{r=1}^{N}\{\gamma\}_r q_r\end{aligned} \tag{3.35}$$

where the modal vectors $\{\phi_b\}_r$, $\{\phi_\psi\}_r$ *and* $\{\phi_m\}_r$ can be obtained from the r-th mode $\{\phi_r\}$ shown in Eq. (3.20).

Thus the random response of element strains can be determined as

$$E[\{\varepsilon\}\{\varepsilon\}^T] = \sum_{r=1}^{N}\sum_{s=1}^{N}\{\varepsilon\}_r\{\varepsilon\}_s^T E[q_r q_s] \tag{3.36}$$

$$E[\{\gamma\}\{\gamma\}^T] = \sum_{r=1}^{N}\sum_{s=1}^{N}\{\gamma\}_r\{\gamma\}_s^T E[q_r q_s] \tag{3.37}$$

CHAPTER IV

NUMERICAL RESULTS AND DISCUSSION

4.1 Computer Program Validation and Mesh Convergence

4.1.1 Thermal Buckling and Thermal Deflection

For the computational test, an eight-layer simply supported rectangular graphite/epoxy composite plate with stacking sequence $(0/90/90/0)_s$ is considered. The dimension of the plate is 15×12×0.048 in., and the ambient temperature is 70°F. The critical buckling temperature and postbuckling deflections are compared with the results in [64]. The same data are obtained.

For thermal buckling: $\Delta T_{cr}=12.36°F$

For maximum thermal postbuckling deflection: $\frac{\Delta T}{\Delta T_{cr}}=1.13$ $\frac{W_{\Delta T}}{h}=0.244$

$\frac{\Delta T}{\Delta T_{cr}}=1.46$ $\frac{W_{\Delta T}}{h}=0.451$

$\frac{\Delta T}{\Delta T_{cr}}=1.62$ $\frac{W_{\Delta T}}{h}=0.524$

4.1.2 Random Response and Strain Validation

The plate used in [65] was analyzed as a validation example. The dimension of the plate is 15×12×0.04 in., and the material properties are:

Young's modulus	$E=10.5\times10^6$ psi
Mass density	$\rho=0.2588\times10^{-3}$ lb-sec^2/in.^{4}
Damping ratio	$\zeta=0.01$
Poisson's ratio	$\nu=0.33$

The results obtained by the present study and in [65] are shown in Table 4.1. The random results from [65] are shown for comparison. Because different elements are used, there are small differences between the results for maximum transverse deflections. However, it is demonstrated that the computer program for thermal buckling, deflection and random response analyses is valid.

4.1.3 Mesh Convergence

In order to guarantee the accuracy of the result in computation, mesh convergence is studied. A quarter plate model of the eight-layer simply supported rectangular orthotropic laminate (15×12×0.048 in.) with the stacking sequence of $(0/90/90/0)_s$ is considered. The ambient temperature is 70°F. The results of critical buckling temperature, maximum thermal deflection, and the lowest two natural frequencies at 170°F are shown in Table 4.2. It can be seen that the results are very close and the difference is less than 5% for 4×4, 5×5 and 6×6 mesh.

4.2 Thermal Buckling and Postbuckling/Deflection Results

The results shown in this dissertation were generated for an SMA fiber-reinforced composite laminate, where the graphite/epoxy composite was treated as the matrix. The in-plane support boundary conditions are that the in-plane displacements, u and v, are equal to zero on all edges of the rectangular and triangular plates. The following material properties were used in the analysis:

SMA-Nitinol [2]		Graphite/Epoxy	
T_s	100°F (37.78°C)	E_1	22.5 (155)
T_f	145°F (62.78)	E_2	1.17 (8.07)
E^*	From Fig. 1.2	G_{12}	0.66 (4.55); G_{23} 0.40 (2.76)
G^*	3.604 Msi (24.86 GPa), $T < T_s$ 3.712 (25.6), $T > T_s$	ν_{12}	0.22
ν	0.3	ρ	$0.1458 \times 10^{-3} (1550.07)$
ρ	$0.6067 \times 10^{-3} lb - s^2 / in.^4 (6450 kg / m^3)$	α_1	$-0.04 \times 10^{-6} (-0.07 \times 10^{-6})$
α	$5.7 \times 10^{-6} /^{\circ} F (10.26 \times 10^{-6} /^{\circ} C)$	α_2	$16.7 \times 10^{-6} (30.1 \times 10^{-6})$

4.2.1 Thermal Buckling

The thermal buckling problems for the composite plate with and without SMA have been solved first. The eight-layer simply supported rectangular orthotropic laminate (15×12×0.048 in.) with the stacking sequence of $(0/90/90/0)_s$ is considered. The full-plate is modeled with a 10×8×2 mesh (160 MIN3 elements) as shown in Fig 4.1. Results shown in Table 4.3 are presented for a laminate with no SMA fibers (v_s=0) and for three SMA prestrain values ε_r=3, 4 and 5% for each nonzero SMA volume fraction (v_s=10, 20 and 30%). It is seen that when the austenite start temperature T_s is 100°F, the critical buckling temperatures of the plate with SMA fibers are lower than the plate without SMA. This is caused by the relatively low modulus of the SMA fibers in relation to the graphite/epoxy matrix they are replacing, and the SMA fibers are not activated when the temperature is lower than T_s. However, the austenite start temperature can be altered to 70°F by changing the Nickel composition in the SMA fibers as shown in Figure 1.1. Thus the critical buckling temperature of the plate with SMA becomes higher than the plate without SMA. This is due to the activation of SMA. The results show that the shape memory effect has a great influence on the critical buckling temperatures of composite structures.

4.2.2 Thermal Postbuckling Deflection

The thermal postbuckling deflections of the composite structures with and without SMA have also been investigated in this section. The composite plates with different stacking sequences, volume fractions of SMA, prestrains of SMA and boundary conditions are studied.

4.2.2.1 Orthotropic laminate

The simply supported eight-layer graphite/epoxy orthotropic rectangular laminate with the stacking sequence of $(0/90/90/0)_s$ is considered first. The dimension of the plate is 15×12×0.048 in. The plate is simulated with 10×8×2 mesh (160 MIN3 elements). The austenite start temperature is 100°F. Figure 4.2 shows the maximum thermal postbuckling deflection behavior of the composite plate without SMA. It is seen that the maximum normalized deflection (W_{max}/h) reaches about 1.923 at 200°F. The maximum deflection results presented in Figs. 4.3, 4.4 and 4.5 are for a laminate with three prestrain values ε_r=3, 4, 5% for each nonzero SMA volume fraction (v_s=10, 20 and 30%). Comparing to the plate without SMA, the thermal deflections of the plate with SMA are much smaller. The W_{max}/h is 0.672 for v_s=10% and 0.193 for v_s=30% at 200°F while the prestrain is 3%.

4.2.2.2 Non-Orthotropic Laminate

The simply supported rectangular 15×12×0.048 in. laminate with a stacking sequence $(0/45/\text{-}45/90)_s$ is considered. The full plate is modeled with 10×8×2 mesh or 160 MIN3 elements. The austenite start temperature is 100°F. The maximum plate deflection versus temperature of the plate without SMA is presented in Fig. 4.6. In Fig. 4.7, the maximum thermal deflection versus temperature for a laminate with prestrain ε_r=3% and SMA volume v_s=10% is presented. It is seen that the thermal deflection of the plate with SMA has much reduction after the SMA is activated.

4.2.2.3 Unsymmetric Laminate

For unsymmetric laminates ([B]≠0), the linear stiffness and the first-order nonlinear stiffness matrices due to [B] and the thermal and recovery bending loads are taken into account. The thermal deflection curves are no longer bifurcation for the plates with or without SMA. These are demonstrated clearly in Fig. 4.8 for the (0/90) laminate. The simply supported rectangular plate is modeled with 10×8×2 mesh, and the dimension of the plate is 15×12×0.048 in. The austenite start temperature of SMA is 100°F.

4.2.2.4 Boundary Conditions

In this section, the rectangular laminates are modeled with 10×8×2 mesh and the austenite start temperature of SMA is 100°F. Figure 4.9 shows the maximum thermal deflection versus temperature for a 15×12×0.048 in. rectangular $(0/90/90/0)_s$ laminate in clamped and simply supported boundary conditions. The clamped plate is stiffer than a simply supported plate. The critical buckling temperature for the clamped plate is higher, and the thermal deflection is smaller. Maximum deflections for the same plate with SMA in clamped condition are shown in Fig. 4.10. It is noticed that the deflection peaks for the simply supported plates around 100°F shown in Figs.4.3, 4.4, and 4.5 no longer exist for the clamped case. In addition, the critical buckling temperatures for the clamped laminates with SMA are much higher as shown in Fig 4.10. For the High-Speed Civil Transport (HSCT) presently under development, the skin panel temperatures would potentially reach

350°F at cruising. It is thus clear from Fig. 4.10 that the thermal deflection can be completely eliminated with v_s=10% and ε_r=5% (or v_s=20% and ε_r=3% which has a critical buckling temperature T_{cr}= 456.42°F).

Figures 4.11 and 4.12 show the maximum thermal deflection versus temperature for a 15×12×0.048 in. rectangular $(0/45/\text{-}45/90)_s$ laminate in simply supported and clamped boundary conditions, respectively. Compared to the simply supported condition in which there is a deflection peak at T_s for the plate with SMA, there is no deflection peak shown in Fig. 4.12 for the case of clamped plate with and without SMA. The case of the SMA embedded plate with 3% prestrain and 20% volume fraction is also studied. The critical buckling temperature is so high that the thermal deflection does not exist when the temperature is below 350°F.

4.2.2.5 Isosceles Triangle

The isosceles right triangles with stacking sequence of (0/45/-45/90)s with all edges simply supported and all edges clamped are studied. The plate is simulated with 144 MIN3 elements as shown in Fig. 4.13, and the austenite start temperature is 100°F. For simply supported edges, the critical buckling temperatures are 40.5 and 230.5°F for the laminate with no SMA, and 10% SMA fibers and 3% prestrain, respectively. The critical buckling temperatures are 130.9 and 320.6 °F, respectively, for the clamped boundary condition. The maximum thermal deflections versus temperature are shown in Figs. 4.14 and 4.15. Thermal deflections do not appear for temperature below 300 and 390 °F for the simply supported and clamped cases, respectively.

4.2.2.6 Effect of SMA Transformation Temperature T_s

In Section 4.2.2.1, the thermal postbuckling behaviors of the SMA embedded orthotropic rectangular laminate with stacking sequence of (0/90/90/0)s and simply supported boundary condition have been presented. It is seen that the existing thermal deflection peaks around 100°F limits the application of the SMA hybrid composite structures for the high speed flight vehicles subjected to combined acoustic and thermal loads between ambient and 350°F (use HSCT as an example). However, those deflection peaks can be eliminated.

As mentioned earlier, the transformation temperature T_s (austenite temperature) can be altered with the changing of the weight percentage of Nickel in SMA. From Fig. 2.1, when the weight percentage of Nickel is at 55.625%, the transformation temperature is shifted to 70°F. The alter of transformation temperature results in the change of critical buckling temperature. Thus the thermal deflection behavior is affected. Figure 4.16 shows the maximum thermal deflections versus temperature for the simply supported rectangular $(0/90/90/0)_s$ SMA embedded plate with the prestrain ε_r=3, 4 and 5% for the SMA volume fraction v_s=10%. The dimension of the plate and the mesh size are the same as in the Section 4.2.2.1. The transformation temperature is 70°F rather than 100°F. The thermal deflection peaks around 100°F as shown in Figs. 4.3, 4.4 and 4.5 have been completely eliminated here. The cases in which SMA prestrains are 3, 4 and 5% and the volume fraction is 20% have also been studied, and the critical buckling temperatures are much higher than 350°F (see Table 4.3), and the thermal deflections disappear in these cases when the operating temperature is lower than 350°F. Thus, the SMA which contains 55.625% Nickel, has the potential use in the applications for HSCT.

4.3 Vibration of Thermal Buckled Plate

4.3.1 Simply Supported Rectangular Laminate

A simply supported 15×12×0.048 in., rectangular (0/90/90/0)s laminate with and without SMA fibers is studied in detail. The mesh size is 10×8×2 for the full plate and the transformation temperature is 100°F. Figure 4.17 shows the first two natural frequencies versus temperature for a laminate without SMA. Between the ambient and the critical buckling temperature, the plate remains flat and the two natural frequencies decrease. The fundamental frequency reaches zero at the critical buckling temperature where the plate losses the stiffness. When the temperature is higher than the critical buckling temperature, the thermal deflection increase in bifurcation form and the first two natural frequencies also increase. There is a crosspoint of the natural frequencies between 120 and 125°F, and the frequency corresponding to mode (2,1) becomes the lowest frequency. Higher frequencies and modes can also be obtained from the Eq. (3.20).

The vibration behavior of the same composite plate with SMA has been studied in three cases which include 3% prestrain with 10% volume fraction, 4% prestrain with 20% volume fraction and 5% prestrain with 30% volume fraction. The austenite start temperature is 100°F. The first two natural frequencies versus temperature are shown in Figs. 4.18, 4.19 and 4.20. It is observed that the thermal deflection of the plate, prestrain and volume fraction of SMA, Young's modulus and recovery stress of SMA and temperature all play a very important role in the dynamic response of the structures. When the in-plane force, which is affected by the above factors, becomes tensile, the stiffness of the structure increases and so do the frequencies. Otherwise the stiffness and the frequencies of the structure decrease. In addition, during the complete temperature range studied, the lowest frequency is always corresponding to mode (1,1) rather than mode (2,1) for plate without SMA.

4.3.2 Clamped Rectangular Laminate

The thermal deflections versus temperature for the clamped 15×12×0.048 in. rectangular $(0/90/90/0)_s$ laminate have been shown in Figs. 4.9 and 4.10. The austenite start temperature is 100°F. It is clear that the clamped plate is more stiff than the simply supported. The critical buckling temperature is much higher and the thermal deflection is smaller for clamped case. The first two lowest natural frequencies versus temperature for the clamped plate without SMA and with 10% SMA fibers and 3% prestrain are shown in Figs. 4.21 and 4.22. For plate with SMA, it is seen that the lowest natural frequency never goes to zero before T_s, since the tensile in-plane force induced by the SMA recovery stress can overcome the compressive in-plane force induced by the change of temperature at T_s. Both natural frequencies increase when the temperature is greater than T_s until the in-plane compressive force from the change of temperature becomes dominant. The overwhelming compressive in-plane force causes the decrease of the natural frequencies until the critical buckling temperature is reached. For the plate without SMA, the mode corresponding to the lowest frequency has changed from mode (1,1) to mode (2,1) between 150 and 175°F.

4.3.3 Isosceles Triangle Laminate

Dynamic response for an isosceles right triangle 12×12×0.048 in. plate with stacking sequence of $(0/45/-45/90)_s$ shown in Fig. 4.13 is studied. The full plate is modeled with 144 MIN3 elements. All three edges with simply supported and all three edges with clamped boundary conditions are considered.

Figures 4.23 and 4.24 show the first two natural frequencies versus temperature for the simply supported laminate without SMA and with 10% SMA fibers and 3% prestrain. It can be seen that there is no crosspoint of the two lowest frequencies during the complete temperature range. For the plate with SMA fibers, the lowest natural frequency does not go to zero before and at T_s=100°F.

The natural frequencies for the clamped case are shown in Figs. 4.25 and 4.26. Because of the rather high critical buckling temperature for the plate with SMA, the lowest natural frequency never goes to zero during the complete temperature range studied. This implies that the plate is rather stiff with the SMA effect. Thus the dynamic response of the plate from external excitation would be greatly reduced within the temperature range.

4.4 Random Response

4.4.1 Effect of Number of Modes

In order to evaluate the convergence characteristics of the present modal analysis formulation and determine the required number of modes for accurate random response predictions, an eight-layer simply supported graphite/epoxy rectangular laminate with the stacking sequence of $(0/90/90/0)_s$ is analyzed. The dimension of the laminate is 15×12×0.048 in. The mode numbers N=1, N=2 and N=4 are used in study. Because the uniformly distributed pressure load p(x, y, t)=p(t) is applied to the plate, the anti-symmetric modes are not included. The quarter plate is modeled with 5×4×2 mesh or 40 MIN3 elements. The material properties, mass density and damping ratio used in the study are:

Young's moduli	$E_1=22.5\times10^6$, $E_2=1.17\times10^6$ psi
Shear moduli	$G_{12}=G_{23}=G_{13}=0.66\times10^6$ psi
Poisson's ratio	$\nu_{12}=0.22$
mass density	$\rho=1.45\times10^{-4}$ lb-sec^2/in.^{4}
damping ratio	$\zeta=0.02$

The RMS(Wmax/h) at 100dB are shown in Table. 4.4. The first 10 frequencies and corresponding mode shapes are shown in Table 4.5. The result shows that the use of four modes obtains converged displacement and strain results. Therefore, four modes are used in the following analysis.

4.4.2 Simply Supported Rectangular Laminate

The random response of a simply supported rectangular laminate with a graphite/epoxy matrix is investigated. The dimension of the laminate is 15×12×0.048 in., and the layup is symmetric $(0/90/90/0)_s$. The SMA transformation temperature is 100°F. The full plate is modeled with 10×8×2 meshes. For the plates with SMA, the dynamic response is affected by the components of stiffness due to SMA ($[K]$) and due to recovery stress of SMA ($[K_r^*]$). The test data shown in Fig. 1.2 indicate that the Young's modulus of SMA is lower than that of the composite matrix. This results in the plate becoming less stiff when SMA fibers are embedded. The increase in the dynamic response, observed in some cases, is due to the relatively lower modulus and higher mass density of the SMA. On the other hand, large in-plane tensile forces are induced by the recovery stress of SMA, and this effect will reduce the dynamic response of the plate. For the simply supported rectangular plate with SMA discussed here, the minimum thermal deflections occur at about 170°F (see Figs. 4.3 to 4.5). Thus the random response of plates at 170 °F may become more important for the potential use of the SMA. The root-mean-square (RMS) of the maximum deflection versus sound spectrum level (SSL) for the plate without SMA, with 3%, 4% and 5% prestrain and 10%, 20% and 30% volume fraction of SMA are shown in Figs. 4.27, 4.28 and 4.29. It is seen that the dynamic response Wmax/h of the plate with some of the lower SMA volume fractions and prestrain, such as the case with 10% volume fraction and 3%, 4% and 5% prestrain of SMA, is actually greater than that of the plate without SMA . In these cases, the recovery forces induced by SMA are not sufficient to overcome the loss of stiffness due to the lower modulus and higher mass density of SMA fibers. However, the plate with 20% and 30% SMA fibers and 3%, 4% and 5% prestrain provide ample recovery forces to significantly reduce the dynamic response of the plate. It is shown that significant dynamic response attenuation can be achieved with SMA volume fraction of twenty percent or more.

The power spectral density (PSD) of the maximum deflections and strains at 170°F and 100dB are shown in Figs. 4.30-4.35 for ten cases: no SMA, 3% prestrain with 10%, 20% and 30% SMA, 4% prestrain with 10%, 20% and 30%, and 5% prestrain with 10%, 20% and 30% SMA. Although the plate with SMA is less stiff than the plate without SMA at temperature less than T_s, the modes of the SMA fiber-reinforced plate exhibit the amplitude reduction gradually and have shifted to high frequencies at temperature higher than T_s.

Figure 4.36 shows the total maximum deflection of plate with no SMA fibers and for three SMA prestrain values ε_r=3, 4, and 5% for each nonzero SMA volume fraction (v_s=10, 20 and 30%) at 170°F and SSL=100 dB. It clearly indicates that the six graphite/epoxy plate with SMA volume fraction of either 20% or 30% and ε_r=3, 4, and 5% are all acceptable designs. Compared to the plate with no SMA fibers, those plates all give smaller amount of maximum RMS random deflections as well as thermal deflections.

4.4.3 Effect of Transformation Temperature T_s

As indicated in Section 4.2.2.5, the alter of the transformation temperature results in the critical buckling temperature change and affects the thermal deflection behavior of the plate. It is thus expected that the behavior of dynamic response of the plate with SMA will be affected also. Figures 4.37, 4.38 and 4.39 show the RMS maximum deflections versus temperature at 300°F for the simply supported rectangular $(0/90/90/0)_s$ SMA embedded plate with the prestrain value ε_r=3, 4, and 5% for the SMA volume fraction v_s=10 and 20%. The dimension of the plate is the same as the one in previous section. The transformation temperature is 70°F rather than 100°F. It is seen that the plate without SMA fibers exhibits significantly reduction of dynamics response because of the additional stiffness due to the fact that the plate is thermally buckled. Adding 10% SMA with 3, 4 and 5% prestrain to the plate increases the dynamic response since the recovery forces can not make compensation on the loss of stiffness due to the modulus deficiency of SMA. However, addition of the 20% SMA provides ample recovery forces to reduce significantly the dynamic response, even though the plate is no longer thermally buckled.

The power spectral density (PSD) of the maximum deflections and strains at 300°F and 100dB are shown in Figs. 4.40-4.45 for seven cases: no SMA and prestrain 3, 4 and 5% for 10 and 20% SMA fiber. It is seen that the SMA finer-reinforced plates tend to reduce the amplitude of dynamic response gradually and shift the response to high frequencies.

The total maximum deflection of plate with no SMA fibers and for three SMA prestrain values ε_r=3, 4, and 5% for each nonzero SMA volume fraction (v_s=10 and 20%) at 300°F and SSL=100 dB is shown in Fig. 4.46. Although the large thermal buckling deflection of the plate without SMA results in the enhancing of the stiffness of the plate, the continuously increased thermal deflection, however, limits many aerospace applications. With 20% SMA are embedded in the composite plate, it not only completely eliminates the thermal deflection and also significantly reduces the dynamics response with 5% SMA prestrain at this temperature. It is shown that the composite structures with twenty or more percent of SMA fibers can greatly reduce the random response due to acoustic excitations. Thus it can enhance the service life of high speed flight vehicles.

The applications of composite structure with embedded SMA are dependent on the volume fraction, prestrain, and temperature range of SMA. In most general cases, the change of volume fraction and prestrain of SMA can improve the behavior of SMA hybrid composite structures and thus alter the application range. The RMS of the maximum deflection versus temperature at 100 dB for the plate without SMA, with 3% prestrain and 10% volume fraction, and with 5% prestrain and 20% volume fraction of SMA are shown in Figs. 4.47 and 4.48. The transformation temperature is 70°F and the dimension of the plate is 15×12×0.048 inch. It is seen that the RMS of the maximum deflection of the plate with 3% prestrain and 10% volume fraction of SMA is larger than that of the plate without SMA in most temperature ranges. This is due to the difference of the modulus between matrix and SMA material and the recovery stresses induced from SMA fibers are not enough to make compensation. The appearance of the peak of the RMS of the maximum deflection limits the application range only between ambient temperature and

120°F. However, for the plate with 5% prestrain and 20% volume fraction of SMA, the RMS (Wmax/h) is smaller than that of the plate without SMA within the entire operating temperature range. There is no peak of RMS (Wmax/h) and thermal deflection existing within the operating temperature range. Thus this optimal configuration can be potently used for high-performance flight vehicles.

Table 4.1 RMS (Wmax/h) and maximum Micro-strain for simply supported isotropic plate

SSL	N=1		N=2		N=4		
(dB)	Wmax/h	Max. Micro-strain	Wmax/h	Max. Micro-strain	Wmax/h	Max. Micro-strain	
110	1.04	64.5	1.04	80.5	1.07	77.7	[65]
	1.03	87.4	——	——	1.03	112.0	present
120	1.89	213.2	1.89	274.5	1.96	259.2	[65]
	1.90	256.5	——	——	1.91	361.0	present

N=number of lowest modes

Table 4.2 Mesh convergence study for the simply supported $(0/90/90/0)_s$ plate (at 170°F for thermal deflection and frequencies)

mesh	3x3	4x4	5x5	6x6
ΔT_{cr}	12.431	12.367	12.332	12.311
$W_{\Delta T}/h$	1.283	1.671	1.796	1.839
ω_1	179.38	167.38	167.42	172.80
ω_2	277.70	272.60	273.36	273.54

Table 4.3 Critical buckling temperatures ΔT_{cr} for the simply support $(0/90/90/0)_s$ plate

v_s, %	ε_r, %	T_s, °F	
		100	70
0	0	12.36	12.36
10	3	10.36	179.1
	4	10.36	214.2
	5	10.36	269.8
20	3	8.78	390.2
	4	8.78	466.4
	5	8.78	591.4
30	3	7.52	----
	4	7.52	----
	5	7.52	----

Table 4.4 Convergence of RMS (Wmax/h) and maximum micro-strain at 100dB with number of modes for simply supported $(0/90/90/0)_s$ plate

No. of Modes	N=1	N=2	N=4
RMS(Wmax/h)	0.9648	0.9484	0.9484
Max. Micro-strain RMS ε_{max}	87.69	84.82	84.82

Table 4.5 Natural Frequencies (Hz) and mode shapes for simply supported $(0/90/90/0)_s$ plate

1st	2nd	3rd	4th	5th
47.988	273.22	355.32	467.82	616.61
(1,1)	(2,1)	(1,2)	(2,2)	(3,1)
6th	7th	8th	9th	10th
765.15	799.67	906.23	1065.2	1144.9
(3, 2)	(2, 3)	(1, 3)	(3, 3)	(1, 5)

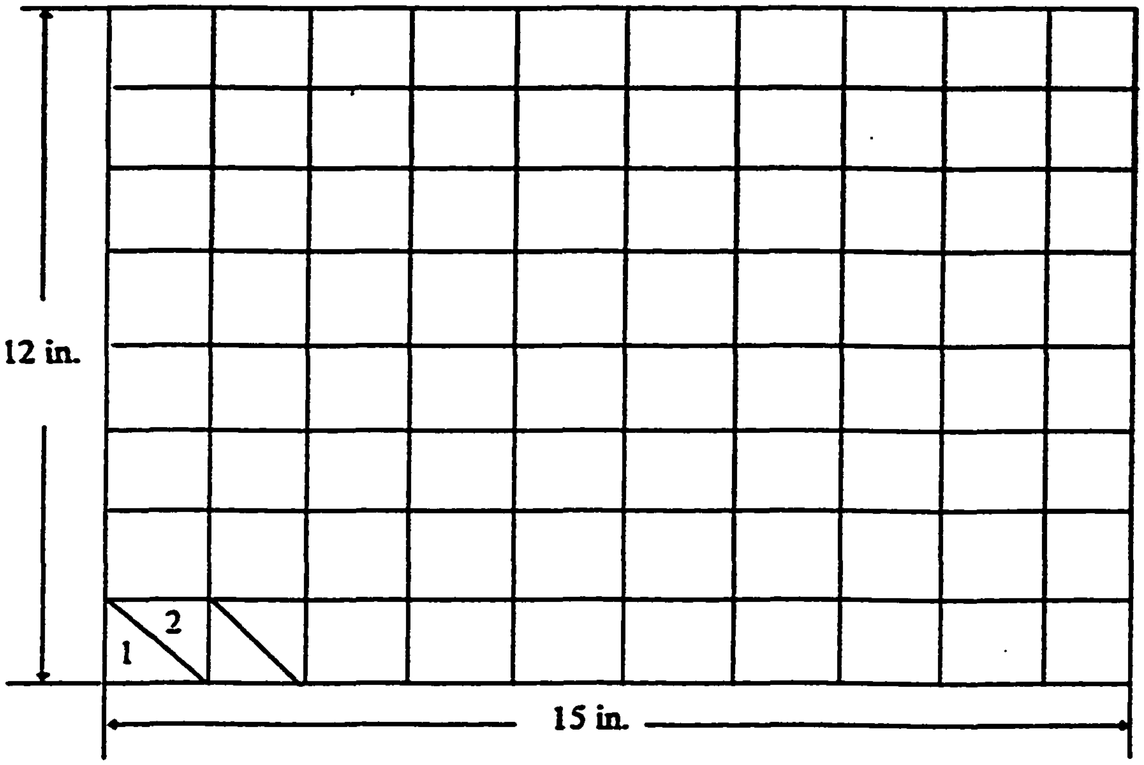

Fig 4.1 Mesh Size for Rectangular Plate

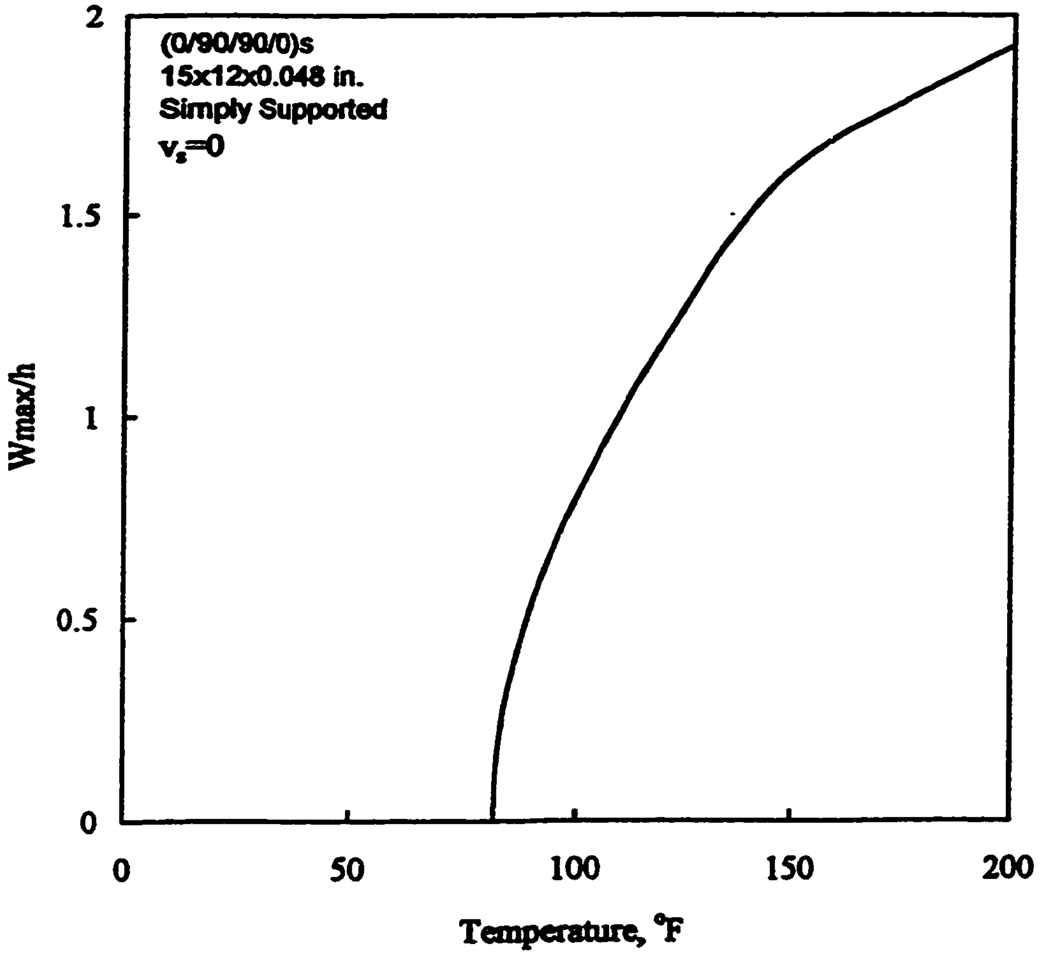

Fig. 4.2 Maximum Thermal Deflection versus Temperature

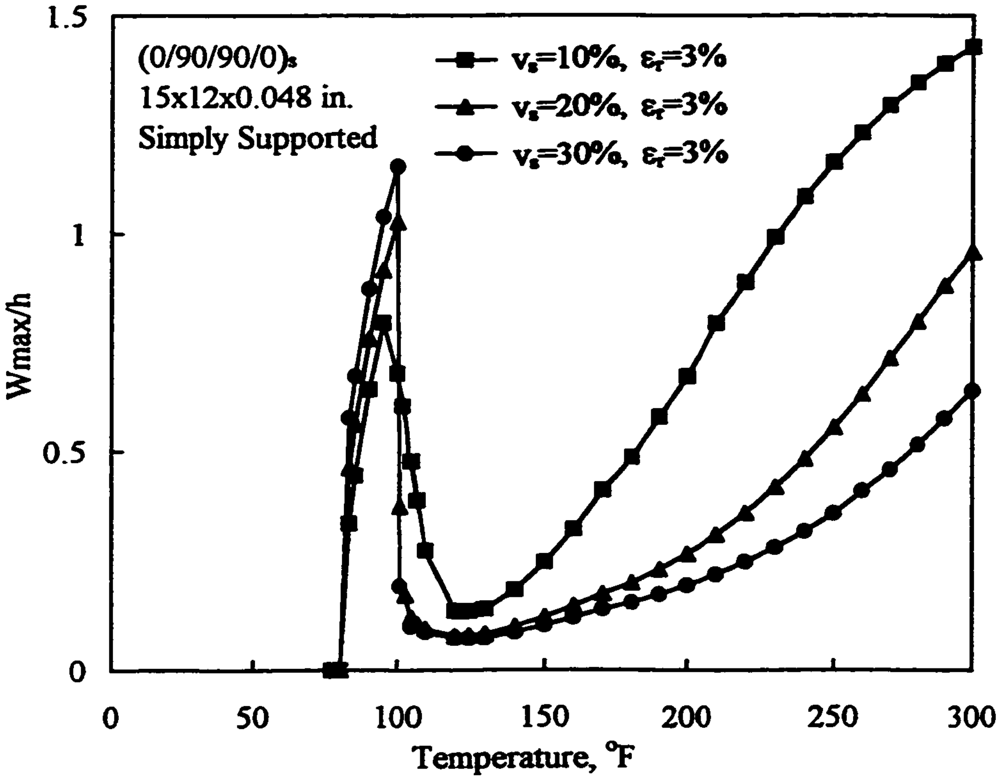

Fig. 4.3 Maximum Thermal Deflection versus Temperature (v_s=10, 20, 30%, ε_r=3%)

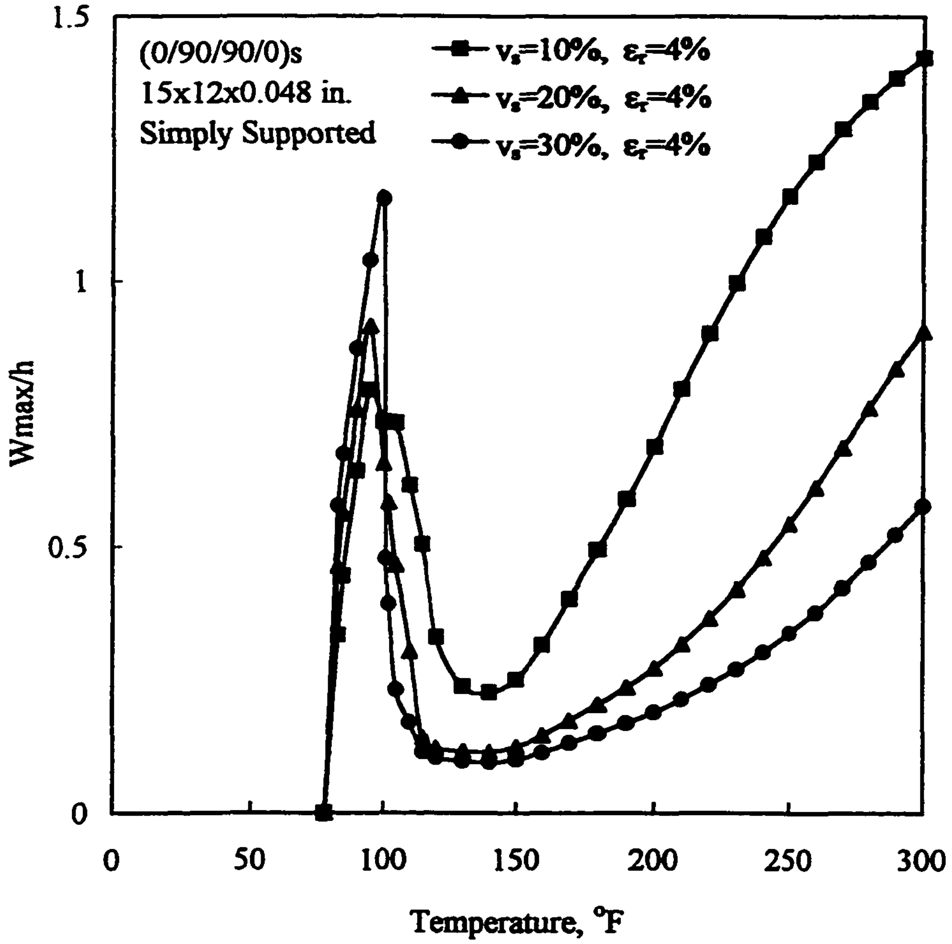

Fig. 4.4 Maximum Thermal Deflection versus Temperature (v_s=10, 20, 30%, ε_r=4%)

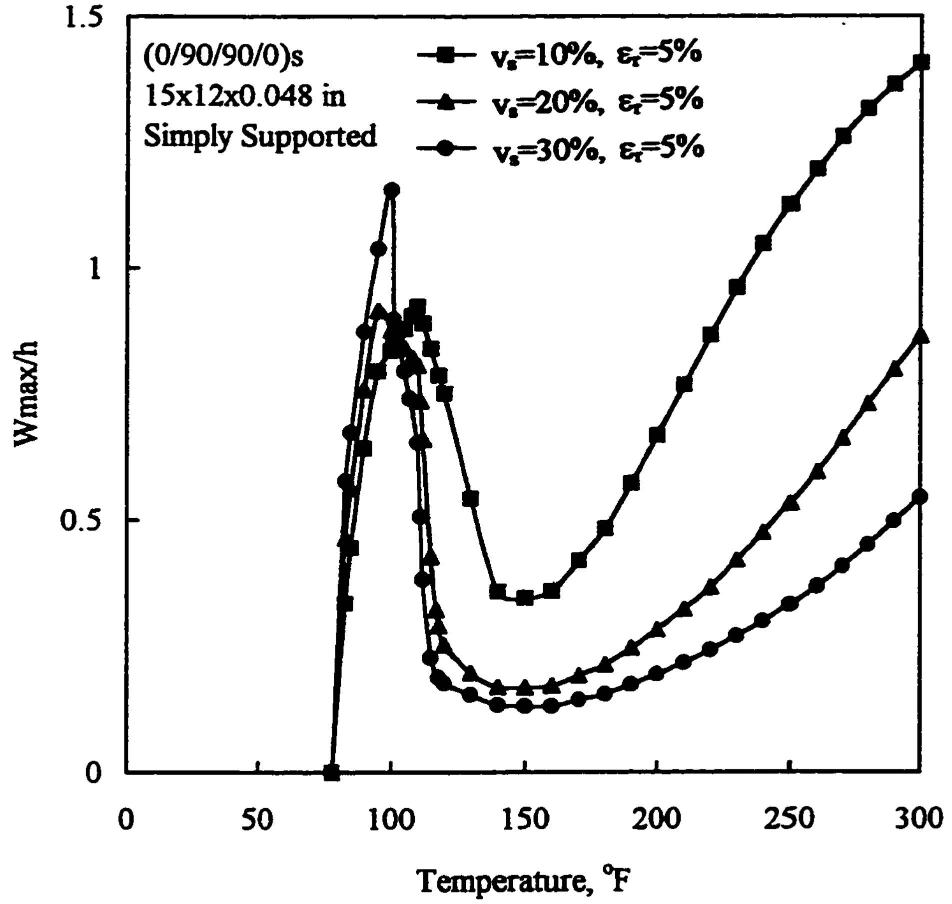

Fig. 4.5 Maximum Thermal Deflection versus Temperature (v_s=10, 20, 30%, ε_T=5%)

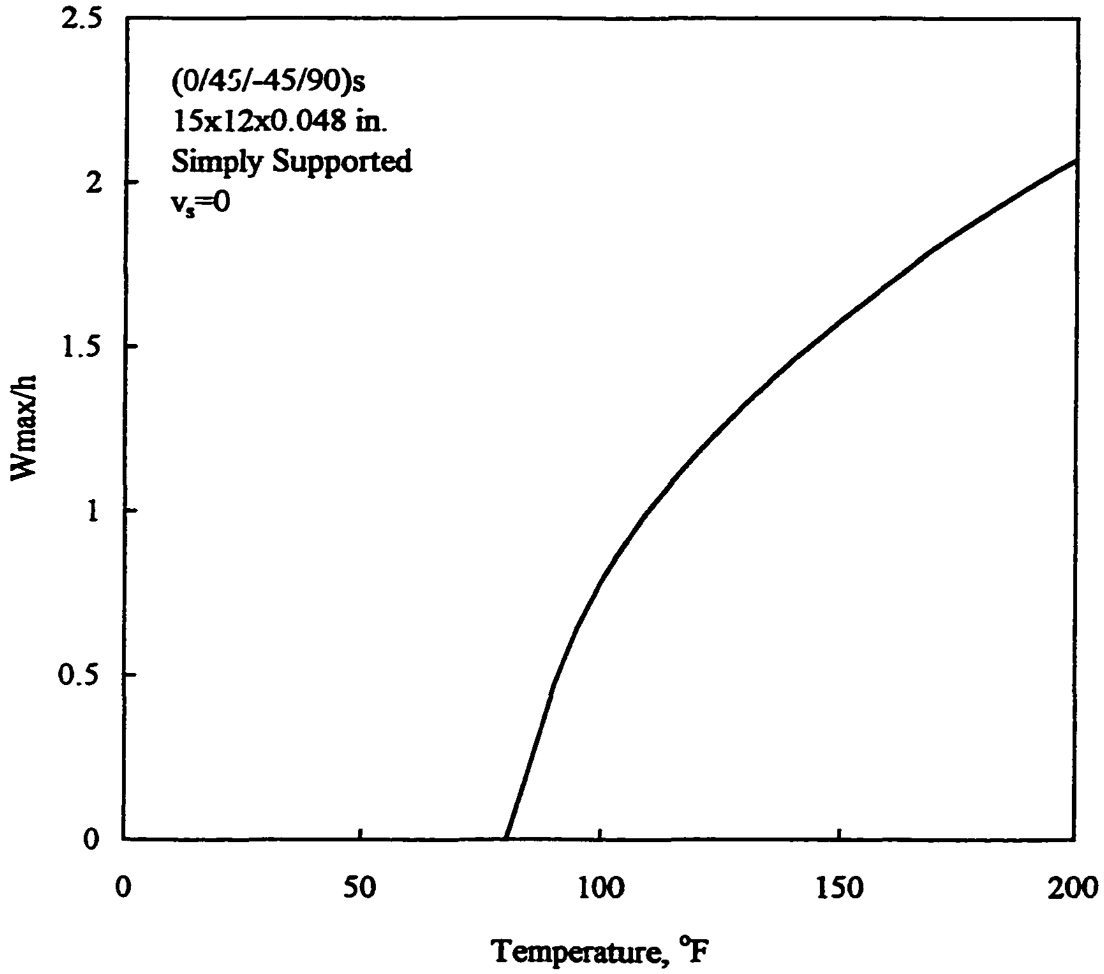

Fig. 4.6 Maximum Thermal Deflection versus Temperature $(0/45/-45/90)_s$

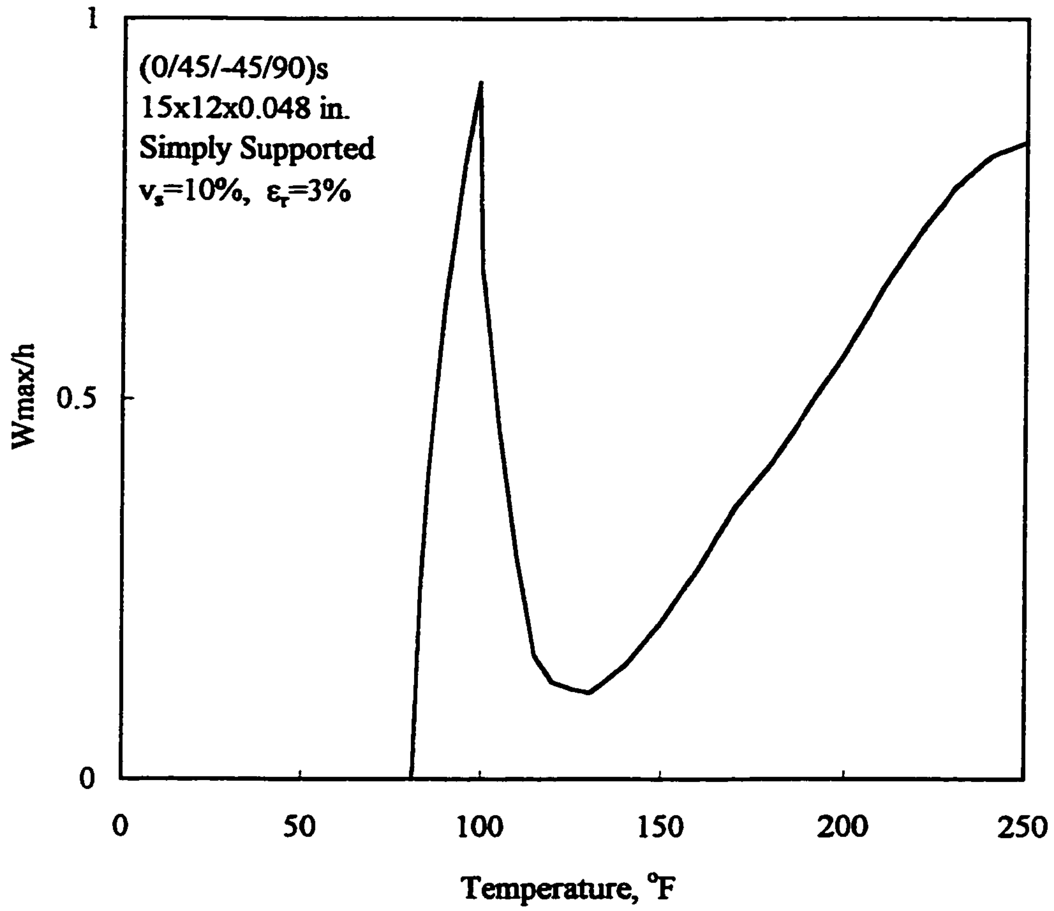

Fig.4.7 Maximum Thermal Deflection versus Temperature
((0/45/-45/90)$_s$, v_s=0, 30%, ε_T=3%)

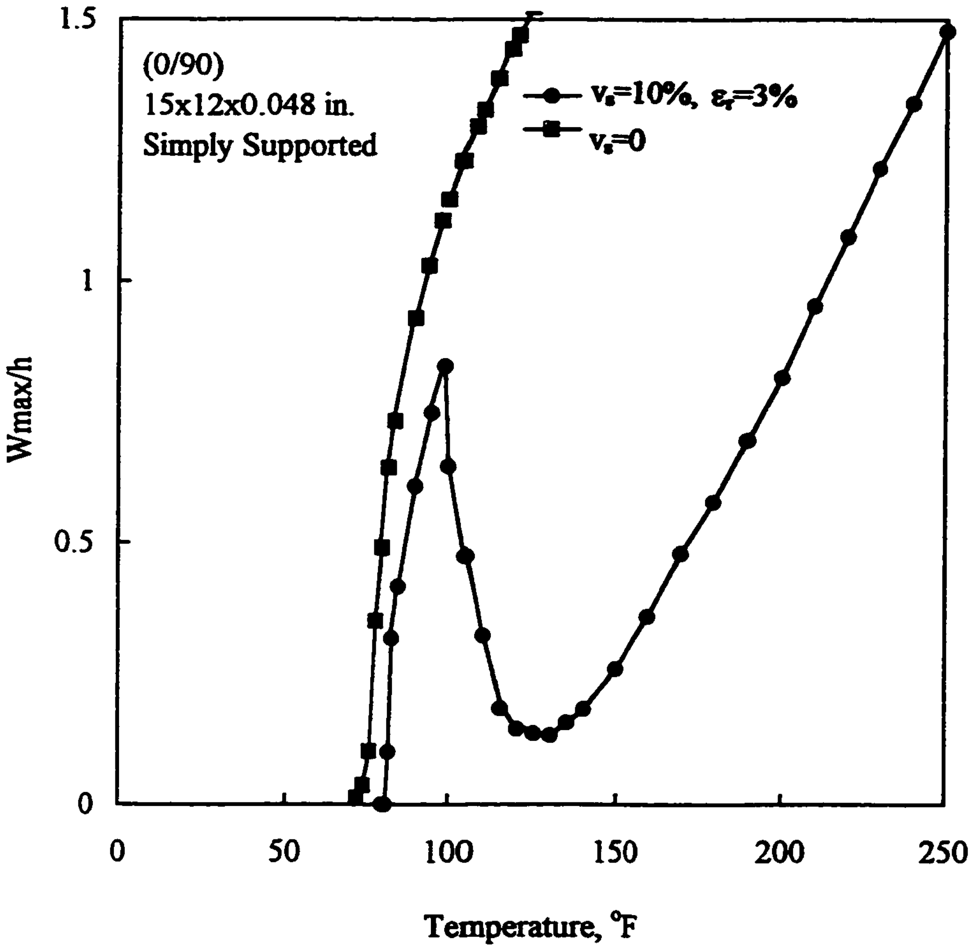

Fig. 4.8 Maximum Thermal Deflection versus Temperature
((0/90), v_s=0, 10%, ε_r=3%)

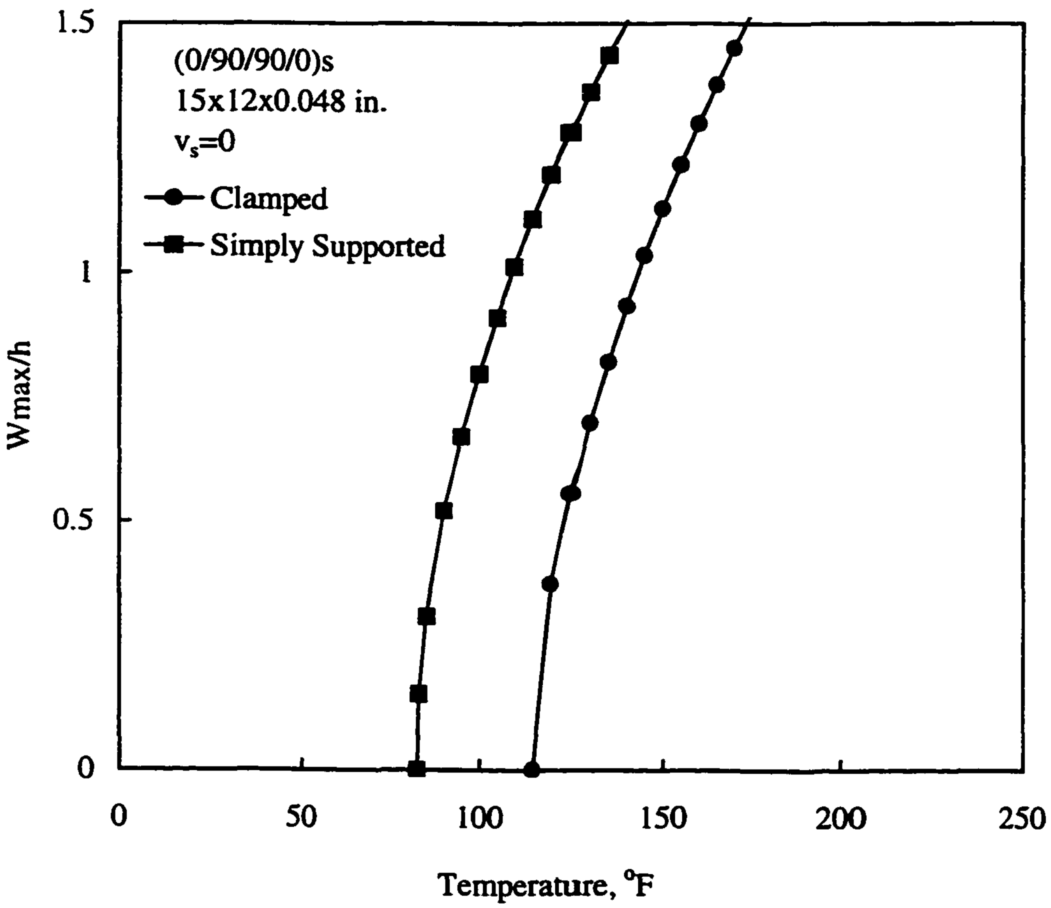

Fig. 4.9 Maximum Thermal Deflection versus Temperature
(Boundary conditions)

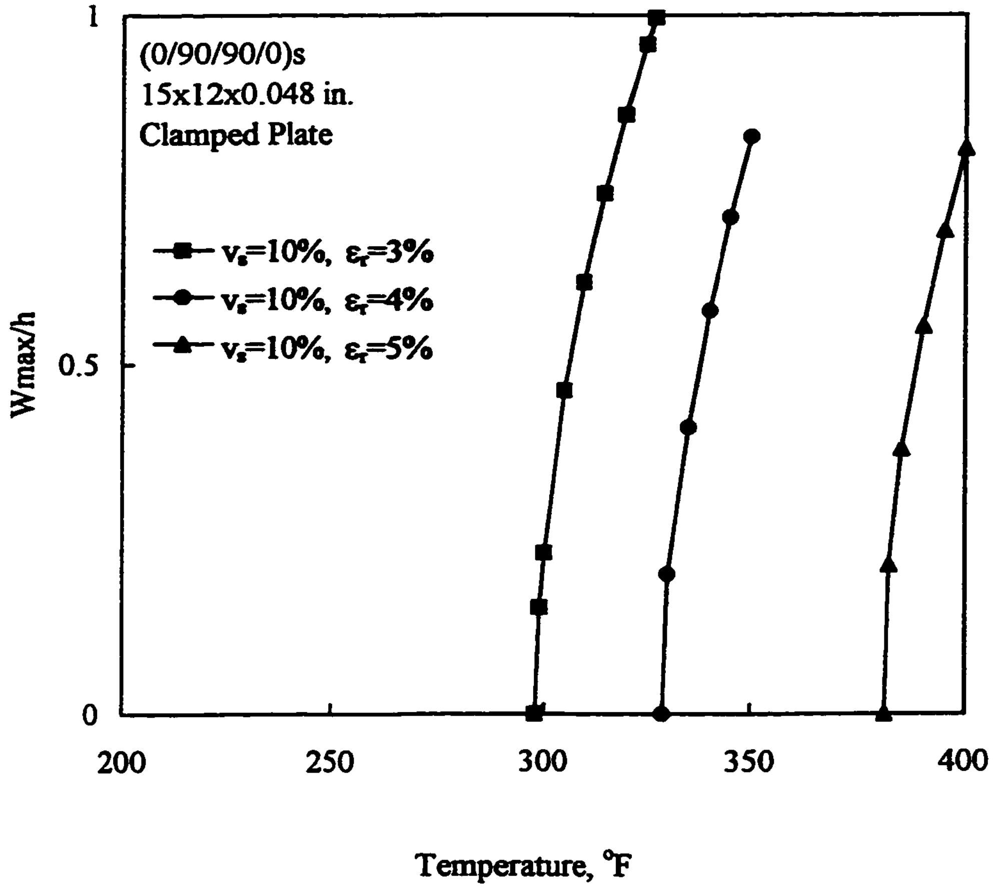

Fig. 4.10 Maximum Thermal Deflection versus Temperature
(Clamped, v_s=10%, ε_T=3, 4, 5%)

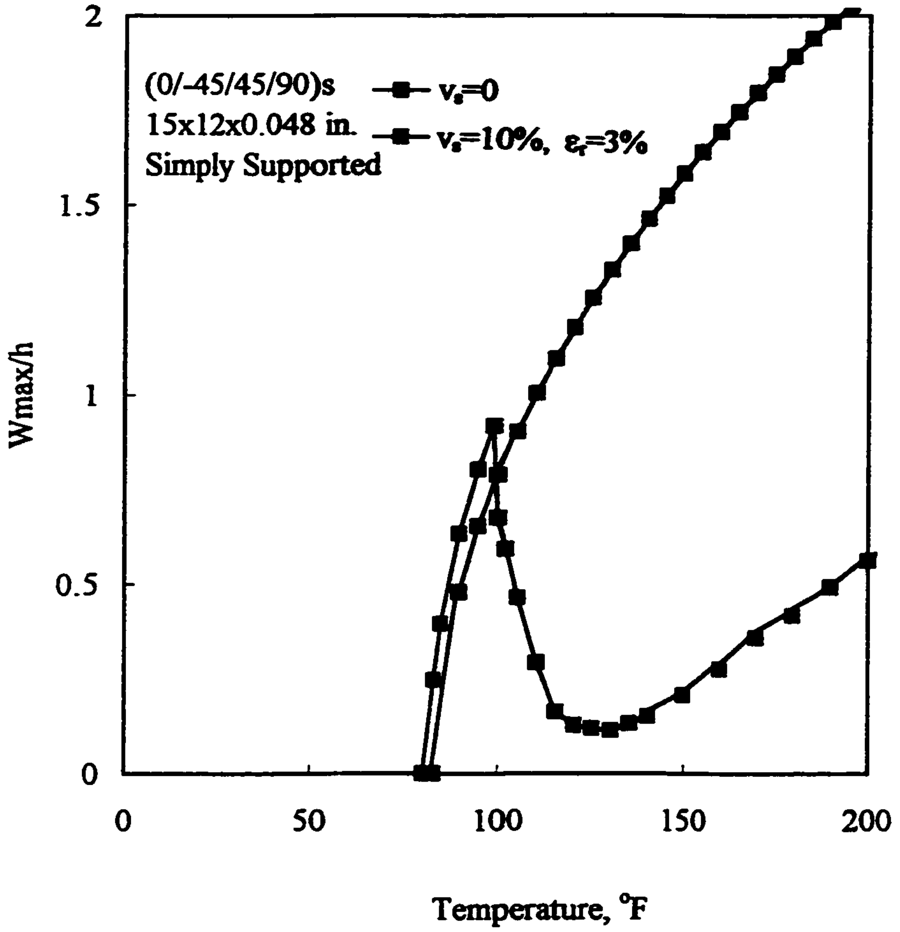

Fig. 4.11 Maximum Thermal Deflection versus Temperature ((0/45/-45/90)$_s$, Simply Supported)

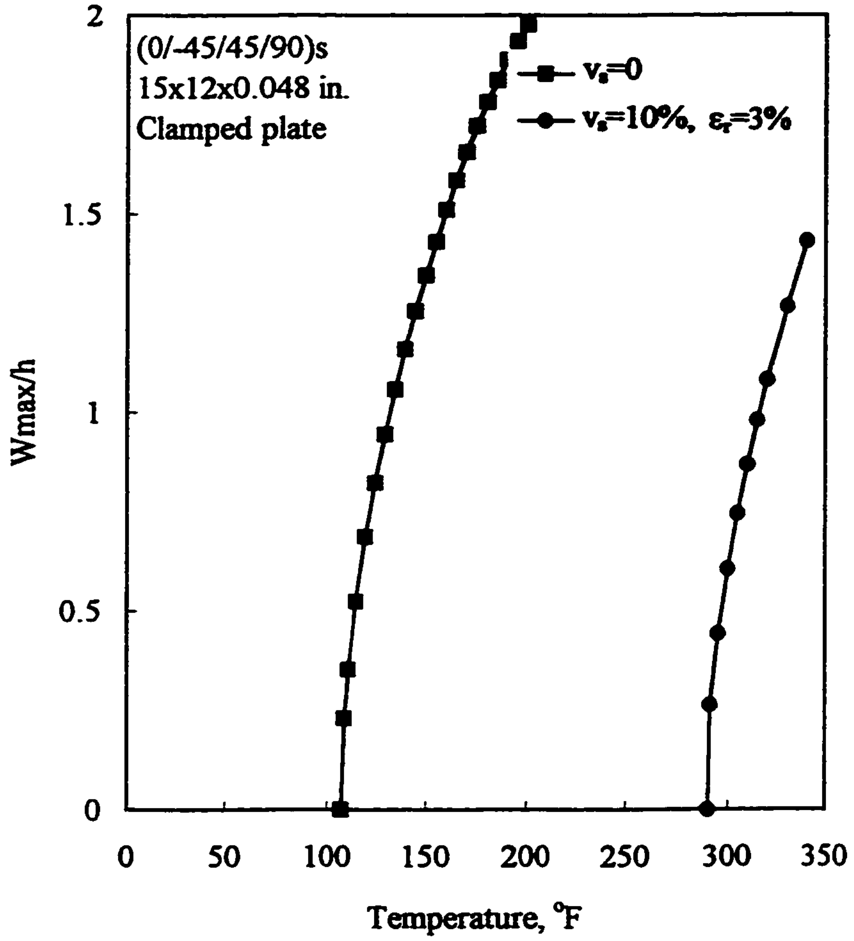

Fig. 4.12 Maximum Thermal Deflection versus Temperature
((0/45/-45/90)$_s$, Clamped)

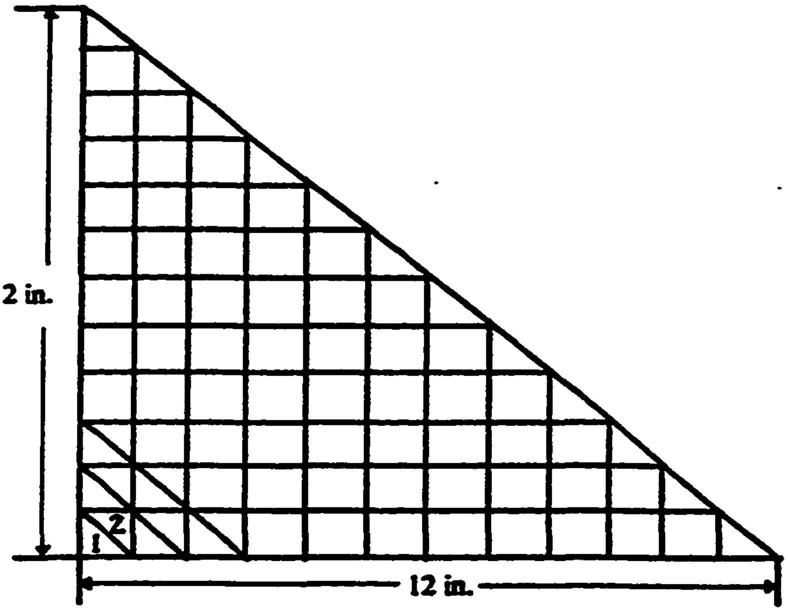

Fig. 4.13 Mesh size for Isosceles Triangular Plate

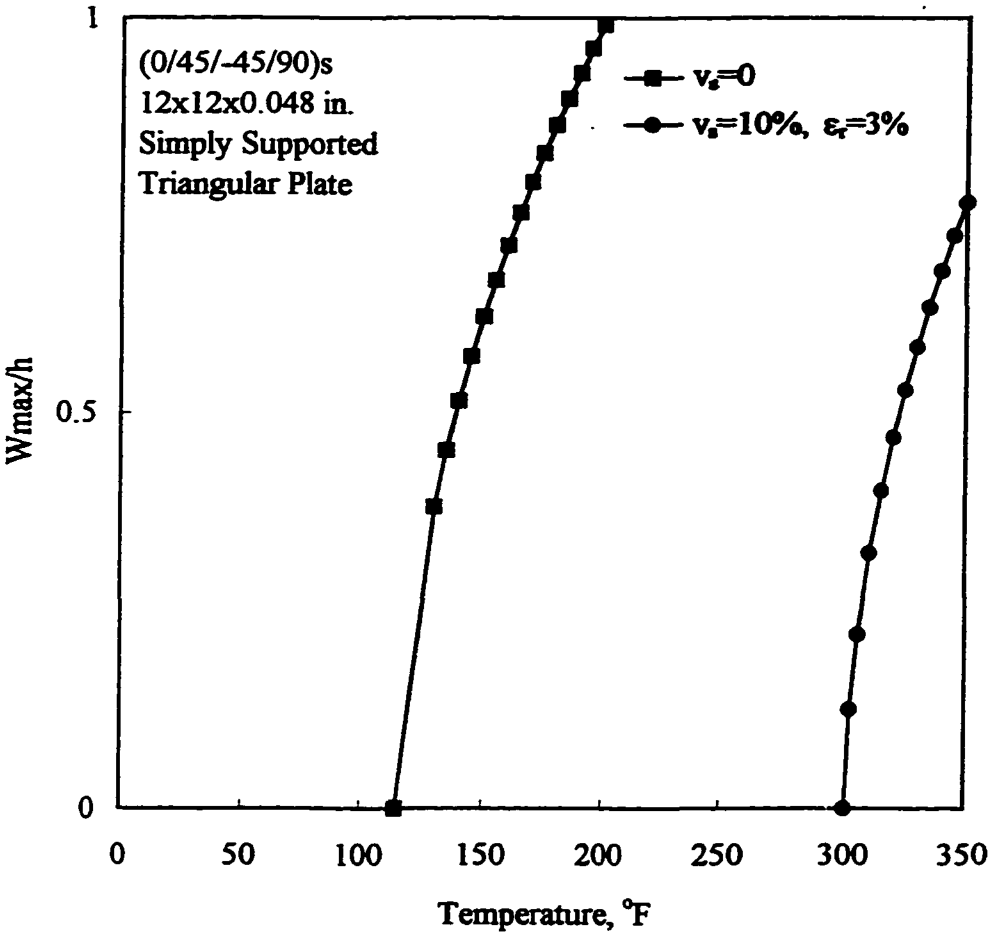

Fig. 4.14 Maximum Thermal Deflection versus Temperature (Triangle, Simply Supported)

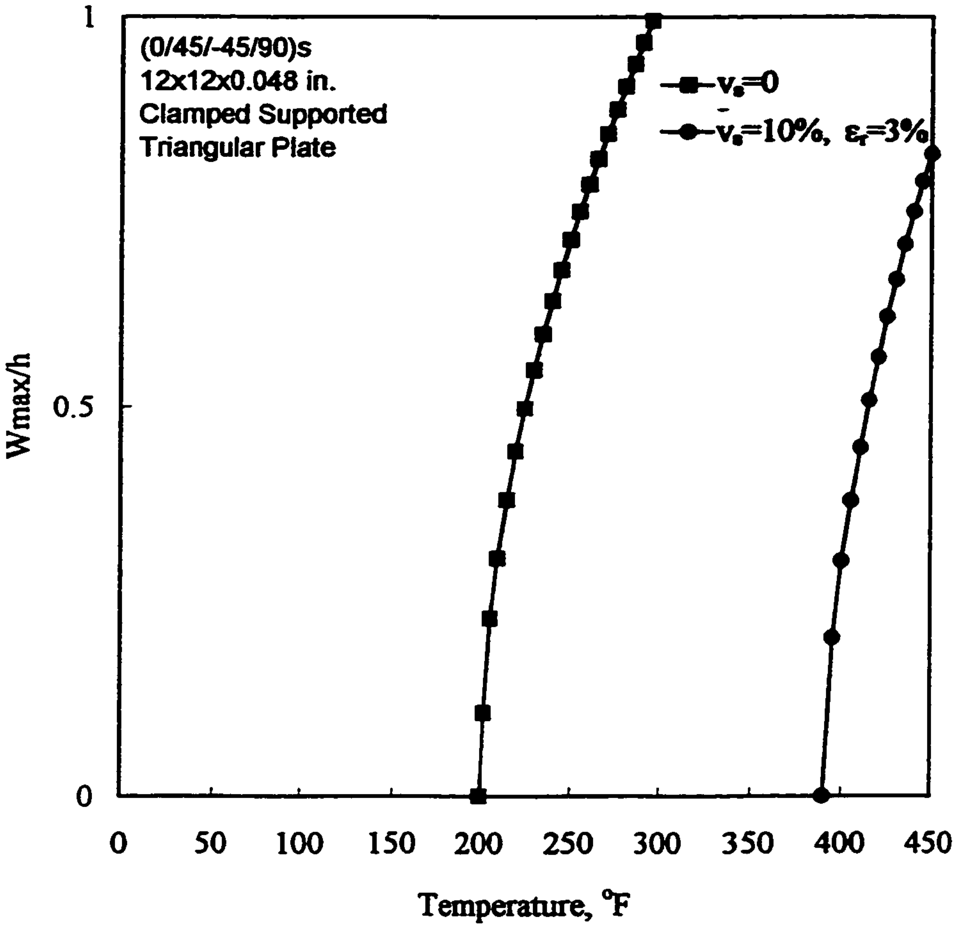

Fig. 4.15 Maximum Thermal Deflection versus Temperature
(Triangle, Clamped)

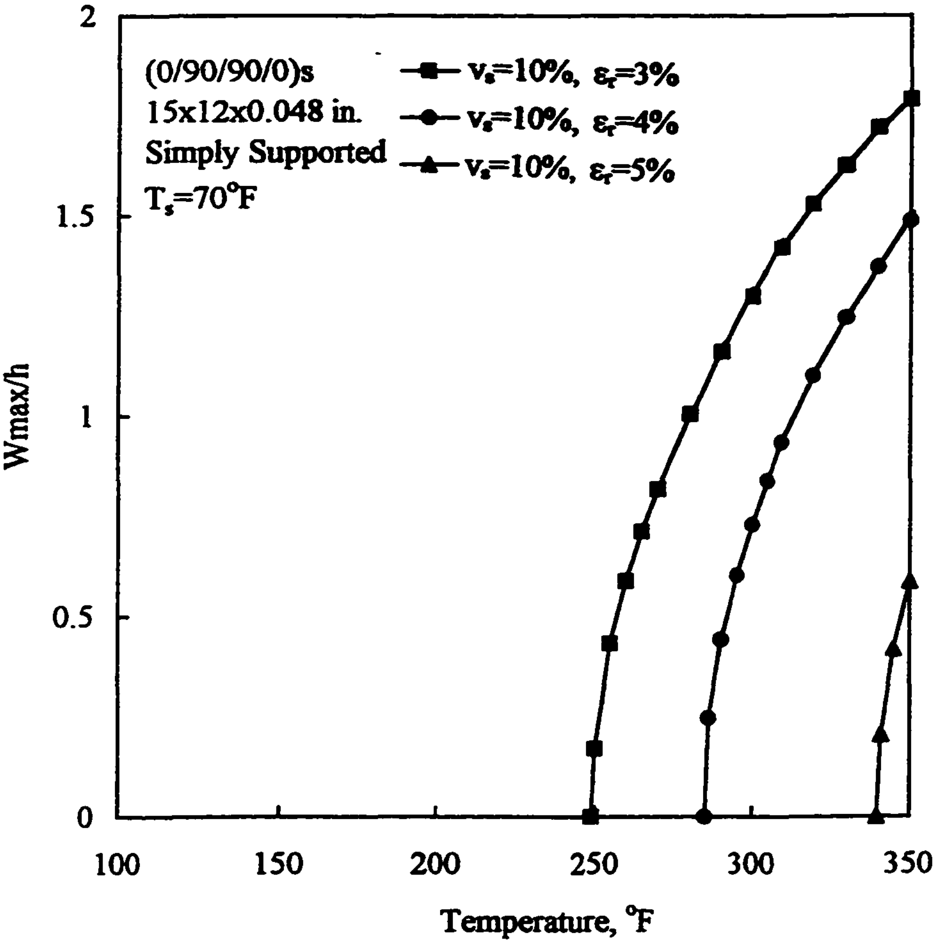

Fig. 4.16 Maximum Thermal Deflection versus Temperature (v_s=10%, ε_r=3, 4, 5%, T_s=70°F)

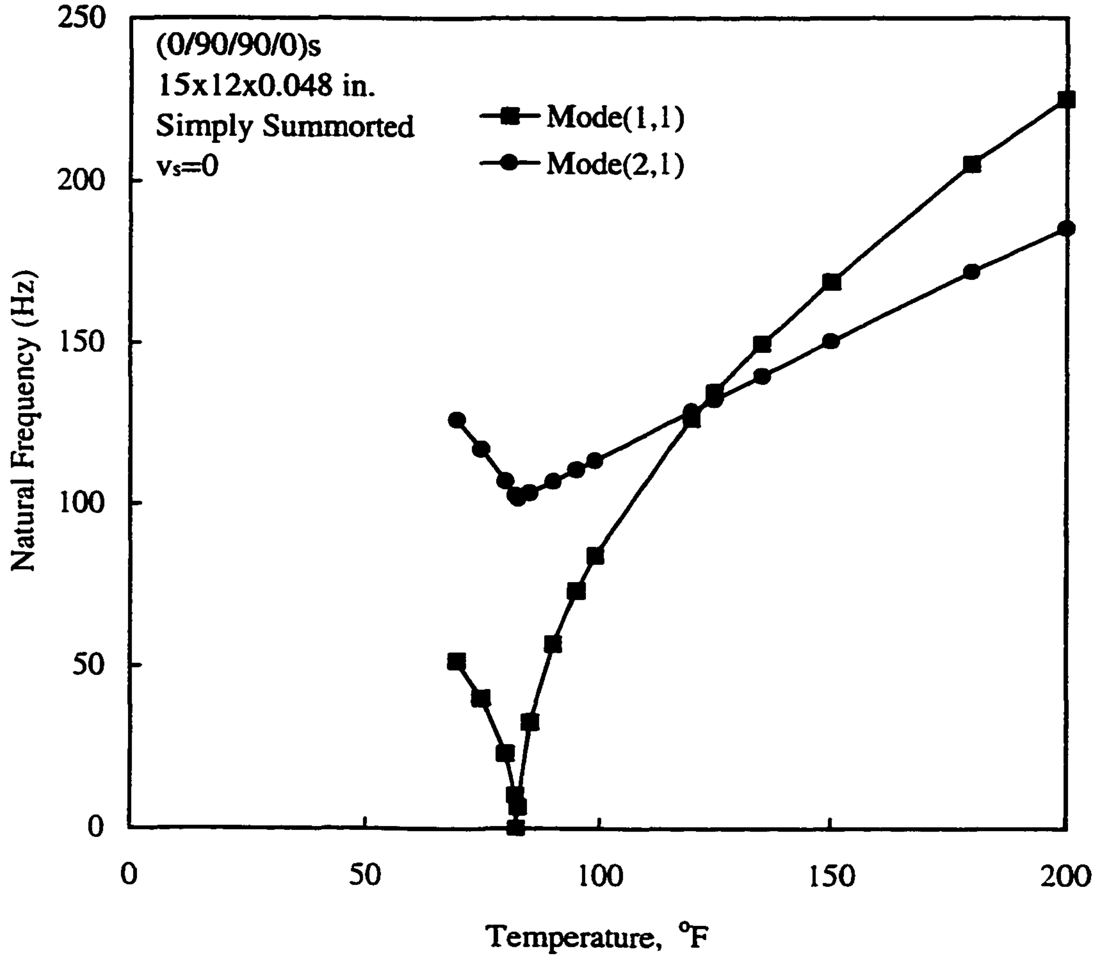

Fig 4.17 Natural Frequencies versus Temperature

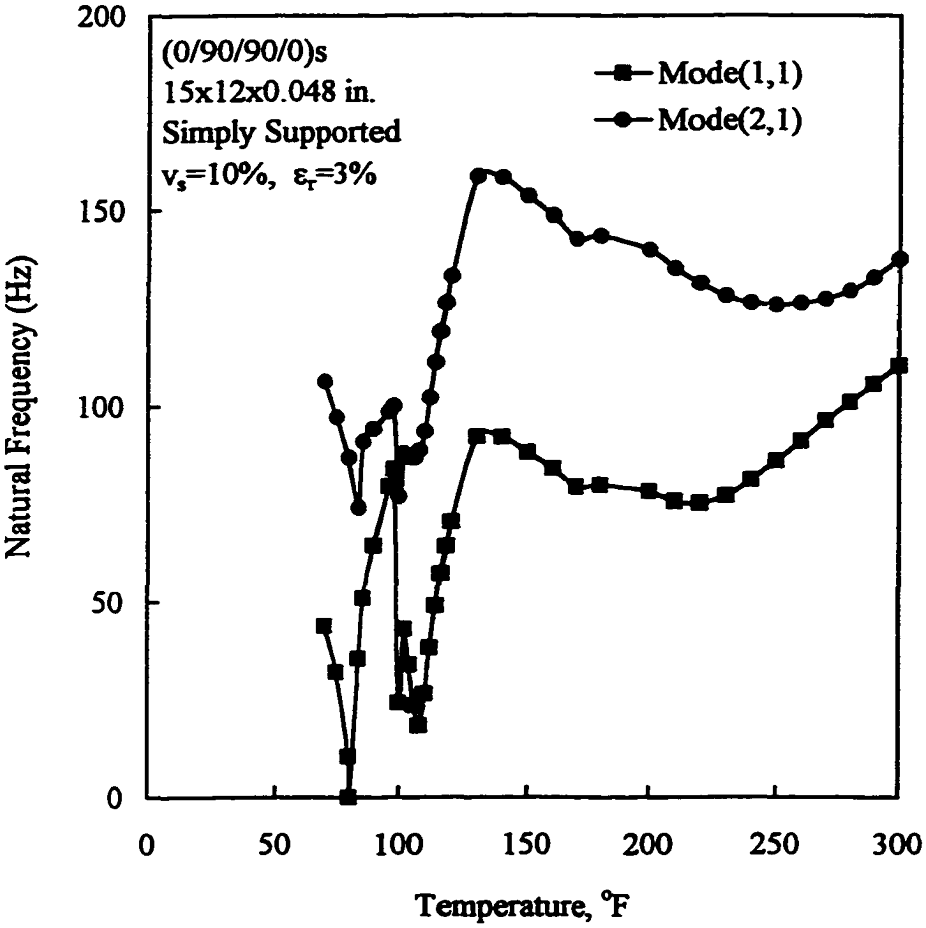

Fig. 4.18 Natural Frequencies versus Temperature
(v_s=10%, ε_r=3%)

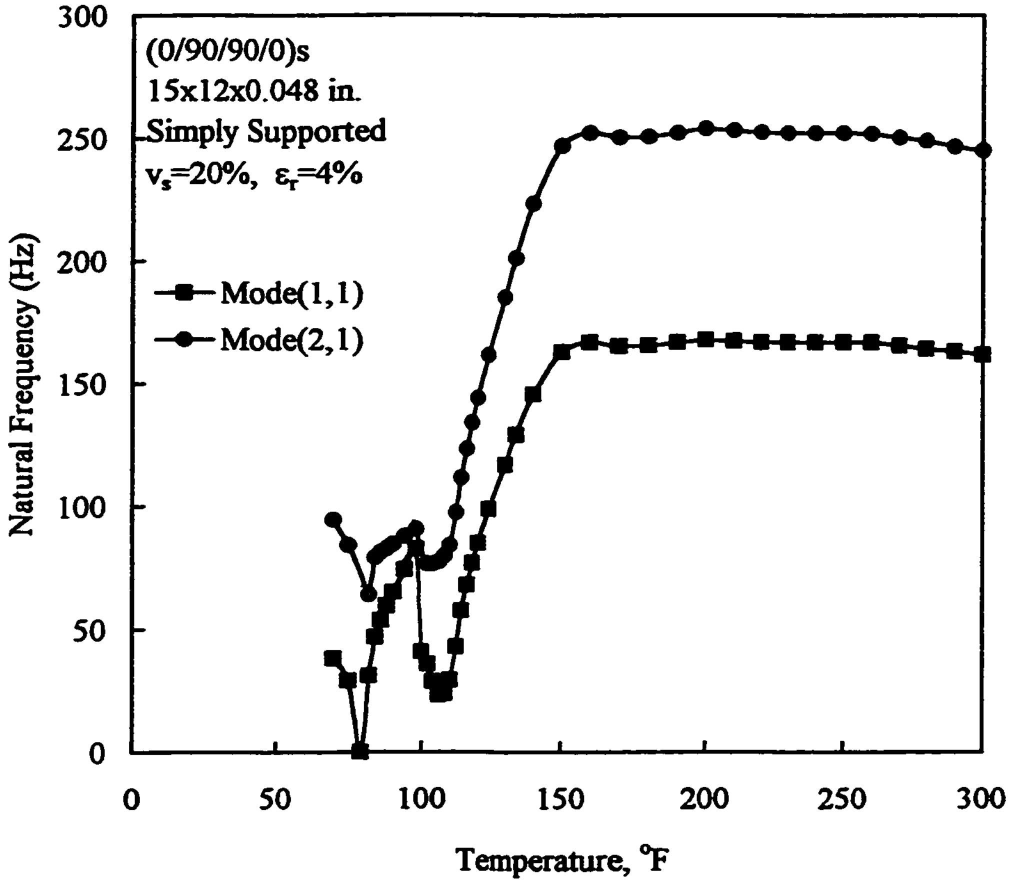

Fig. 4.19 Natural Frequencies versus Temperature
(v_s=20%, ε_r=4%)

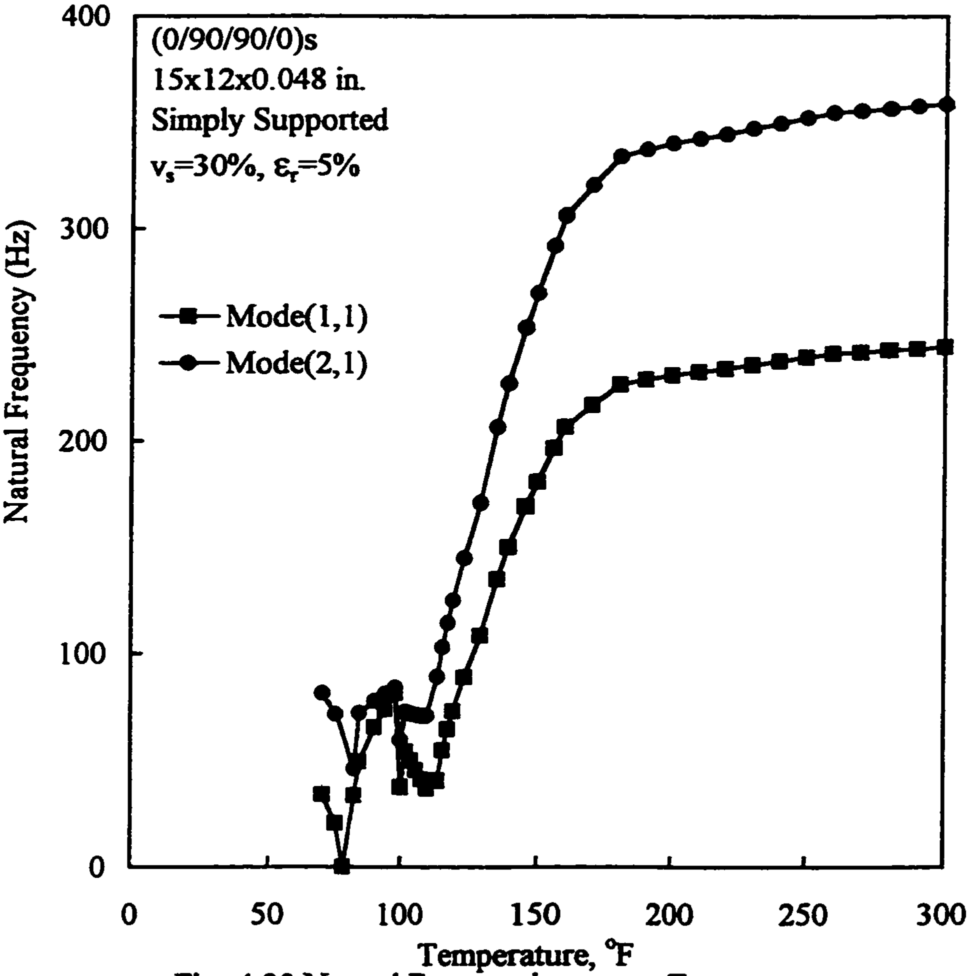

Fig. 4.20 Natural Frequencies versus Temperature
(v_s=30%, ε_r=5%)

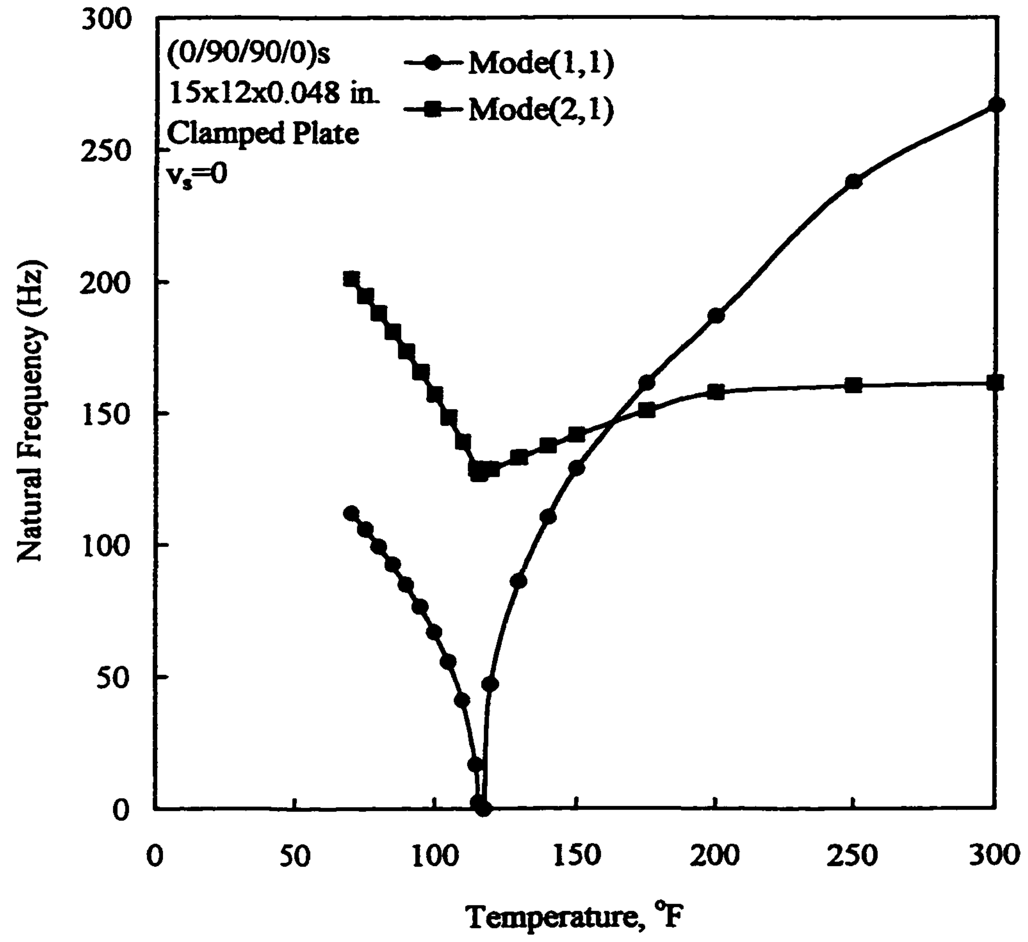

Fig. 4.21 Natural Frequencies versus Temperature (Clamped)

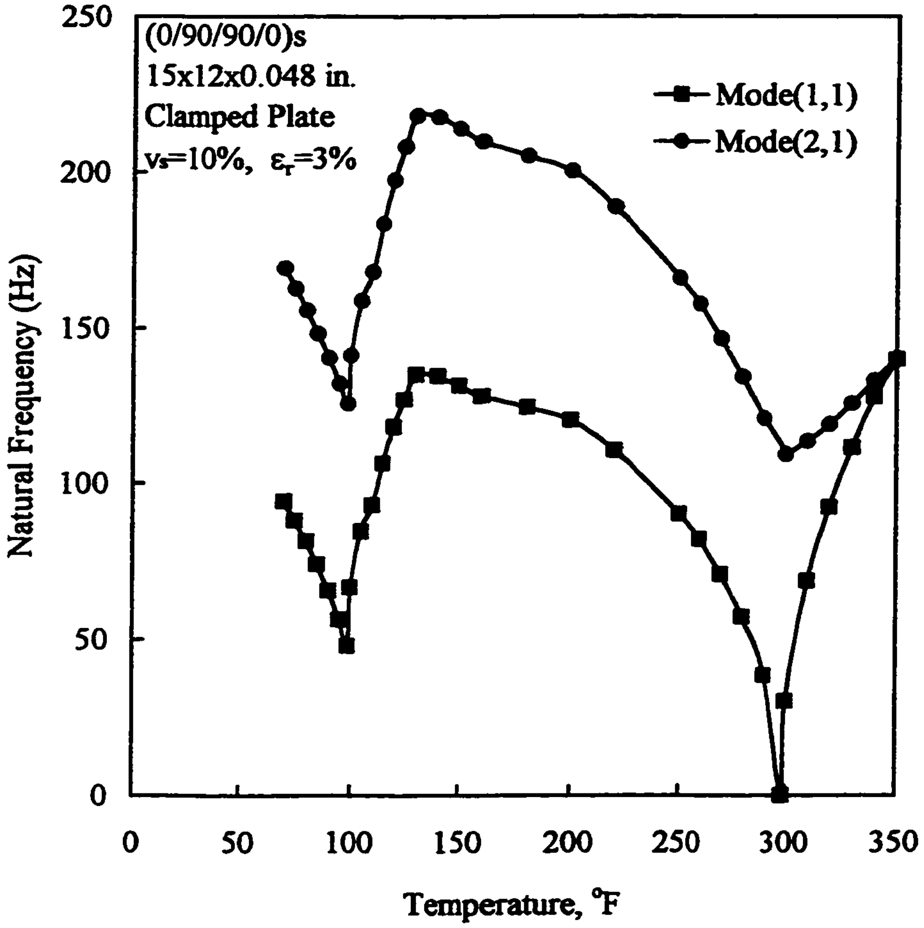

Fig. 4.22 Natural Frequencies versus Temperature
(Clamped, v_s=10%, ε_T=3%)

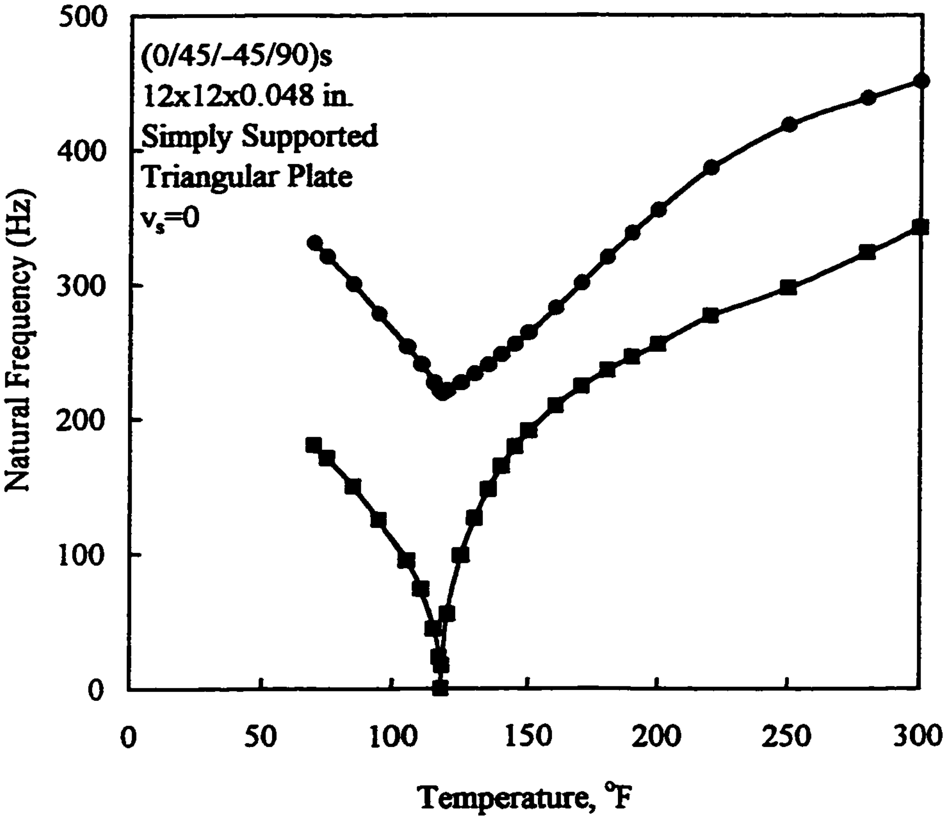

Fig. 4.23 Natural Frequencies versus Temperature
(Triangle, Simply Supported)

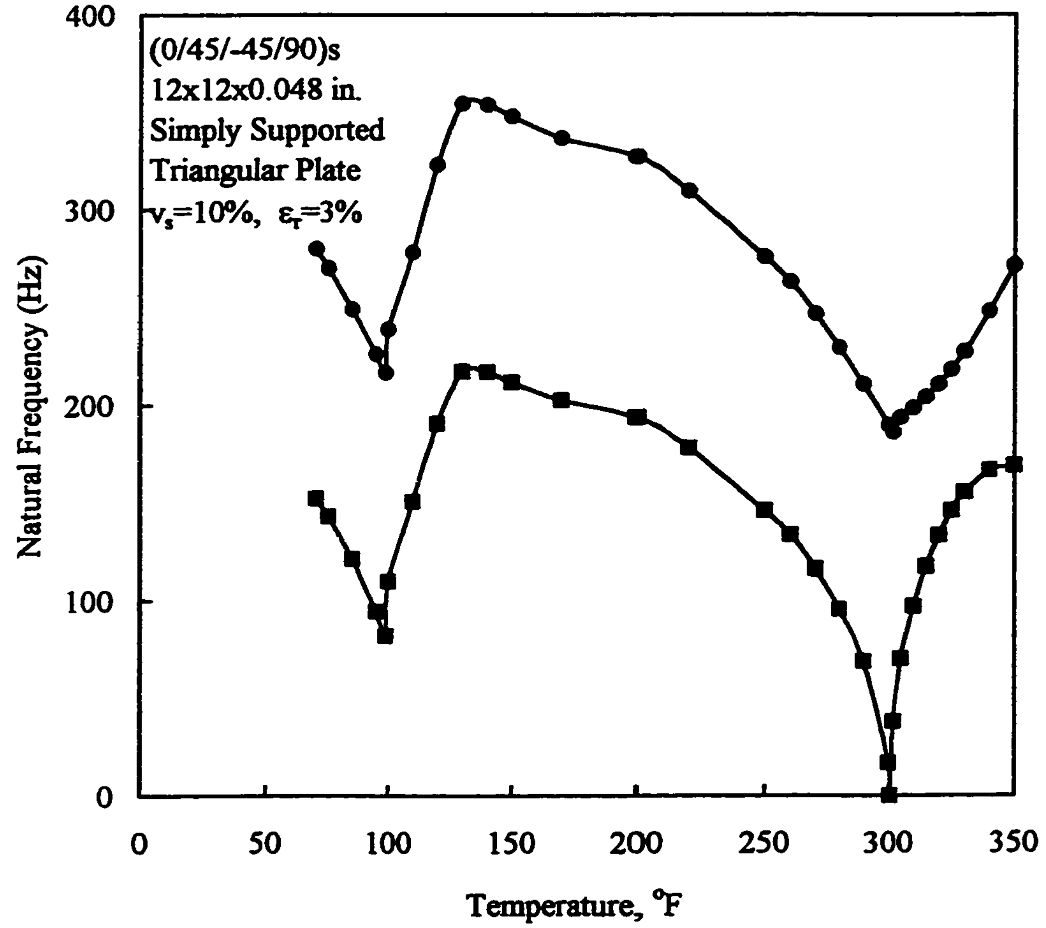

Fig. 4.24 Natural Frequencies versus Temperature (Triangle, Simply Supported, v_s=10%, ε_T=3%)

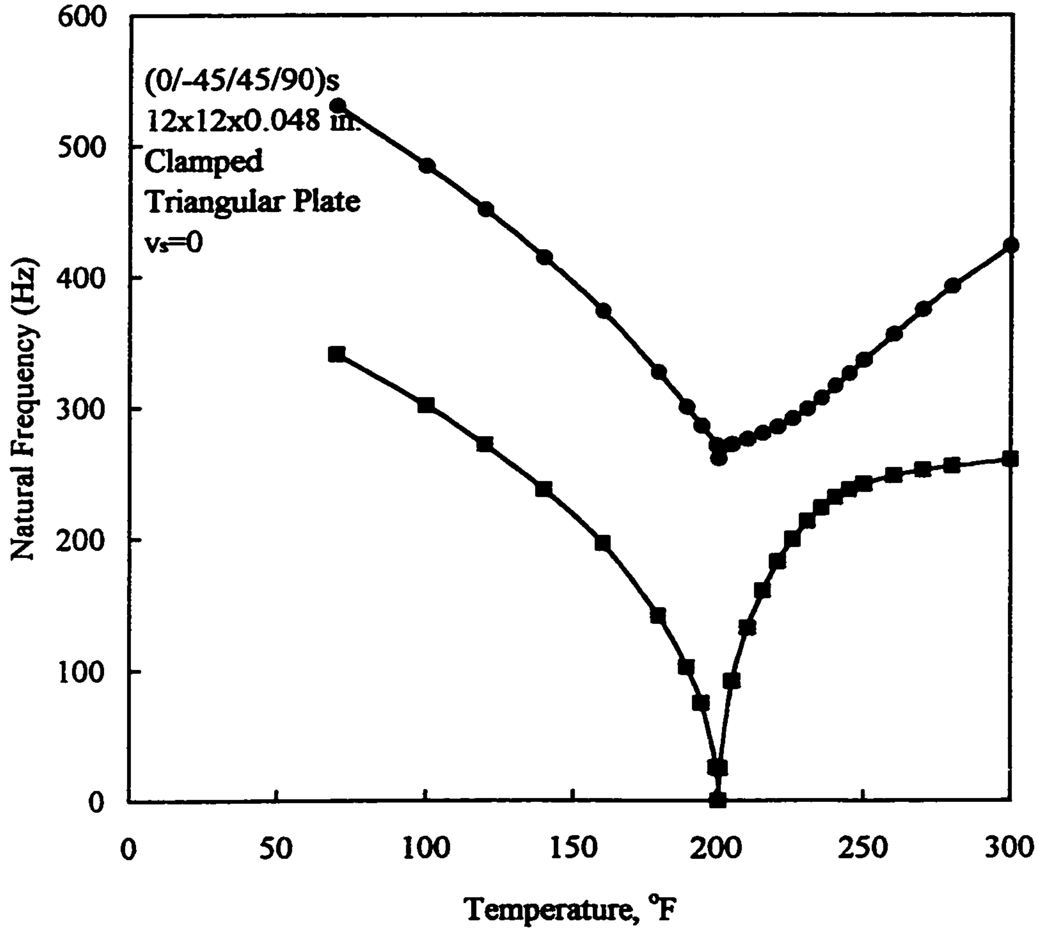

Fig. 4.25 Natural Frequencies versus Temperature
(Triangle, Clamped)

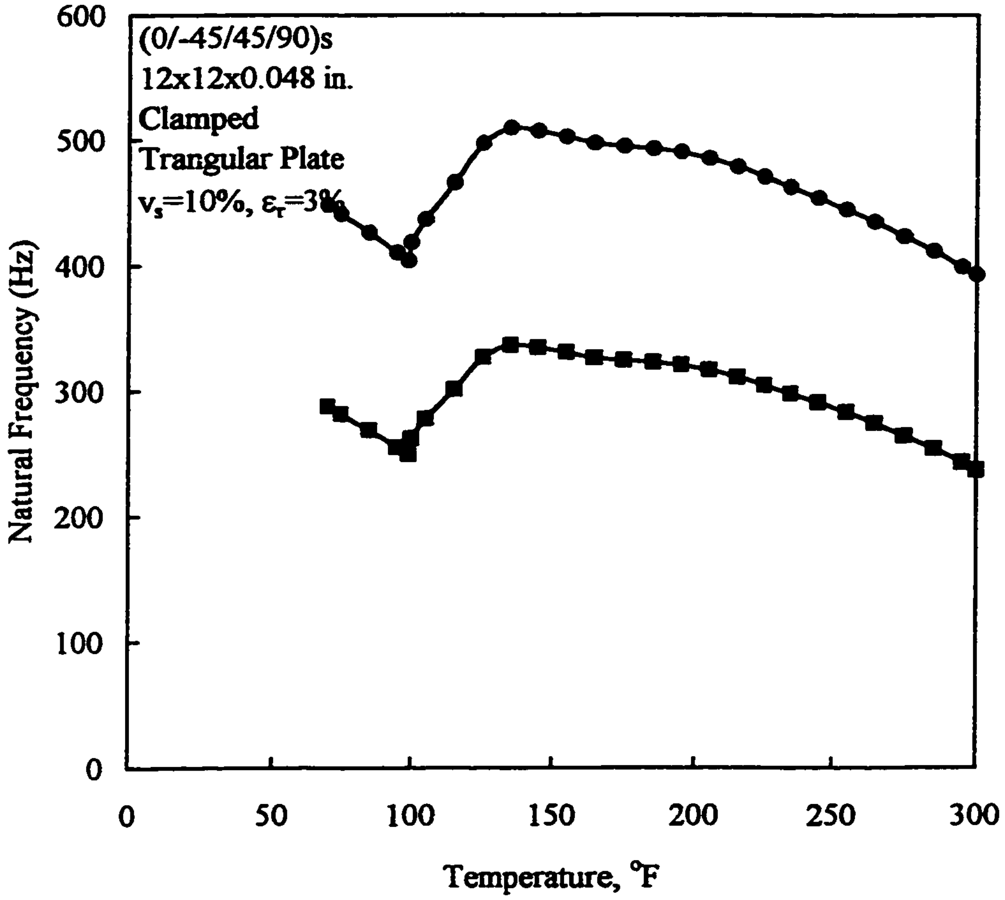

Fig. 4.26 Natural Frequencies versus Temperature (Triangle, Clamped, v_s=10%, ε_T=3%)

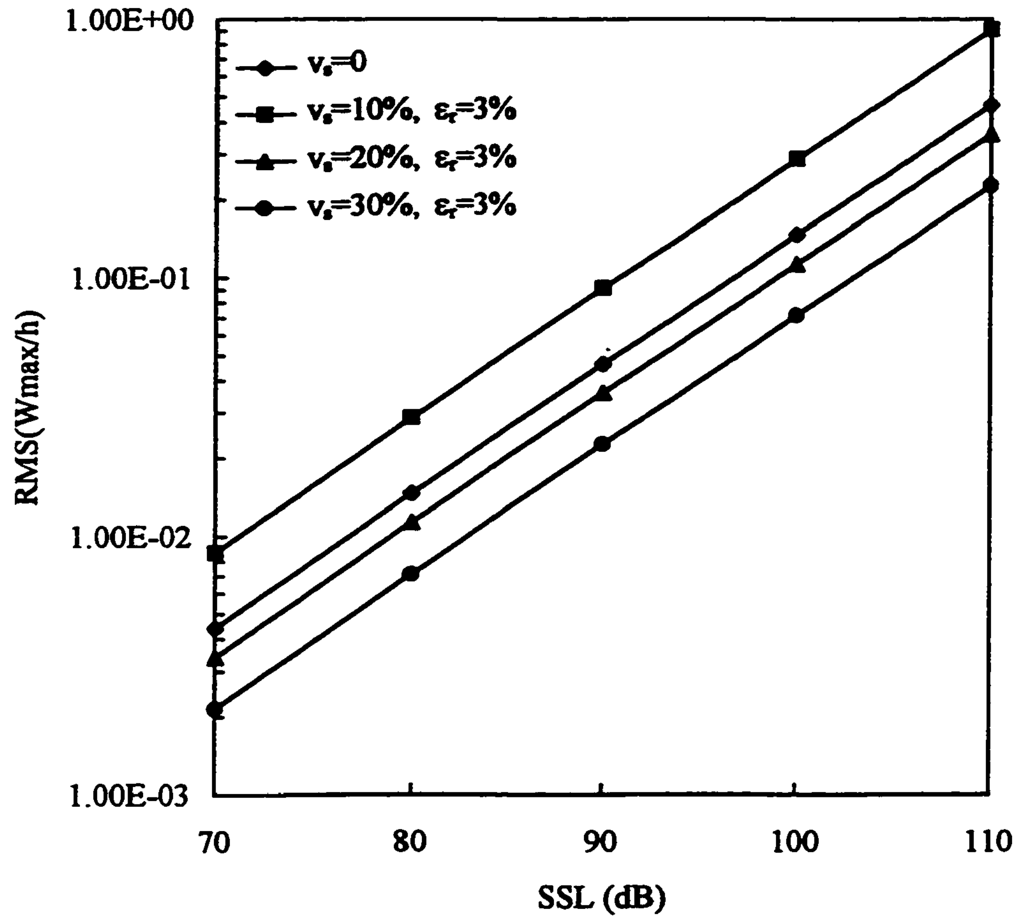

Fig. 4.27 RMS(Wmax/h) versus Sound Spectrum Level at 170°F (v_s=0, 10, 20, 30%, ε_r=3%)

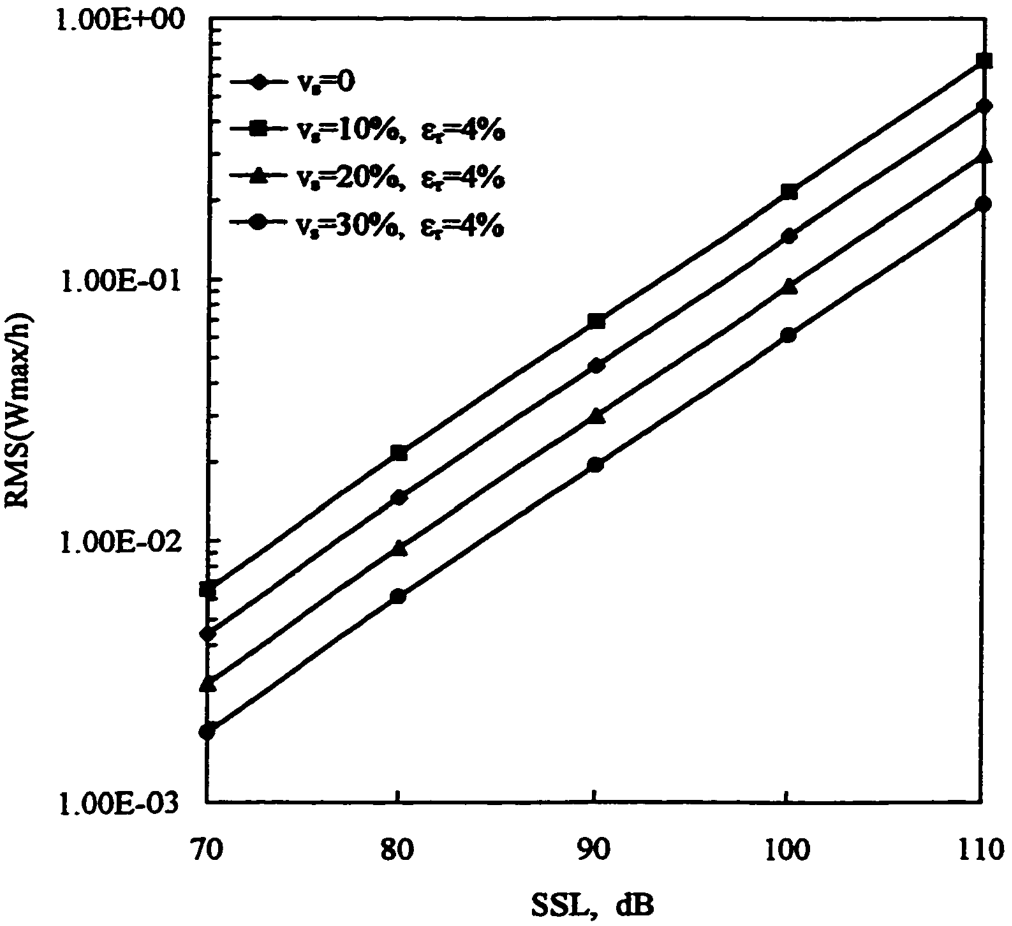

Fig. 4.28 RMS(Wmax/h) versus Sound Spectrum Level at 170°F (v_s=0, 10, 20, 30%, ε_r=4%)

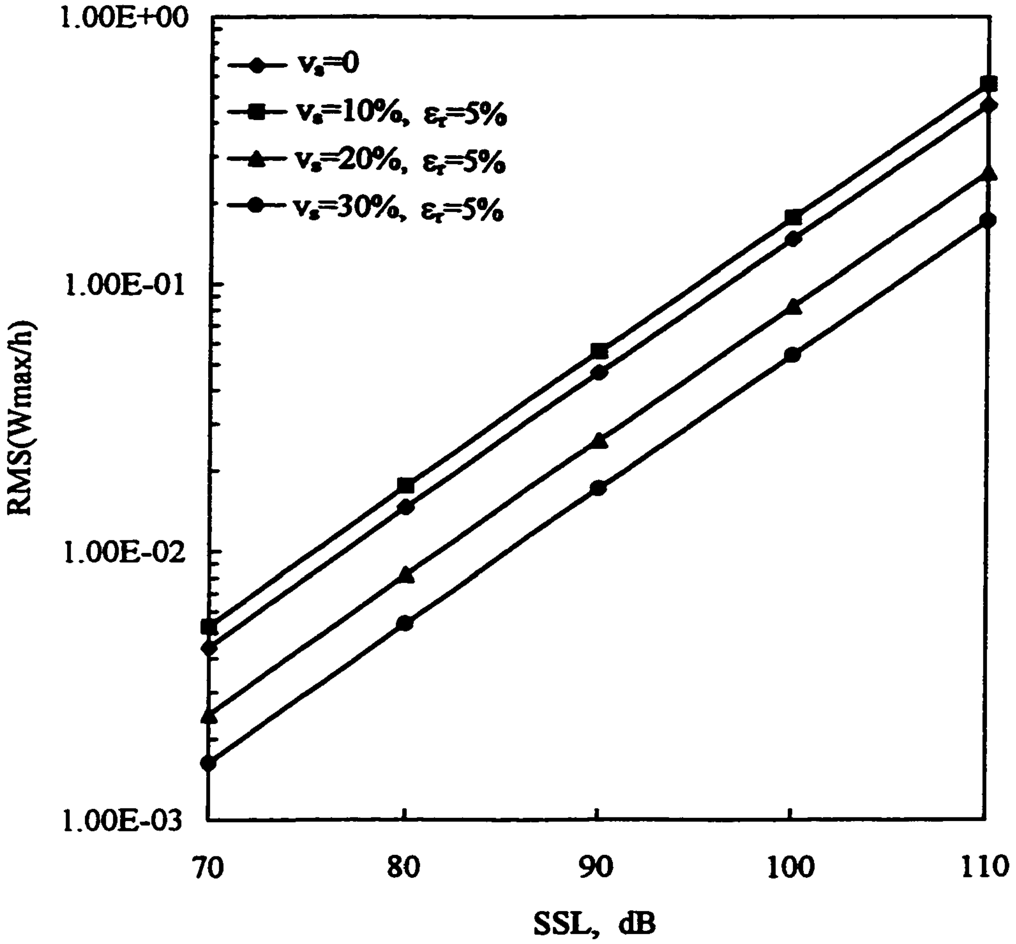

Fig. 4.29 RMS(Wmax/h) versus Sound Spectrum Level at 170°F ($v_s=0$, 10, 20, 30%, $\varepsilon_T=5\%$)

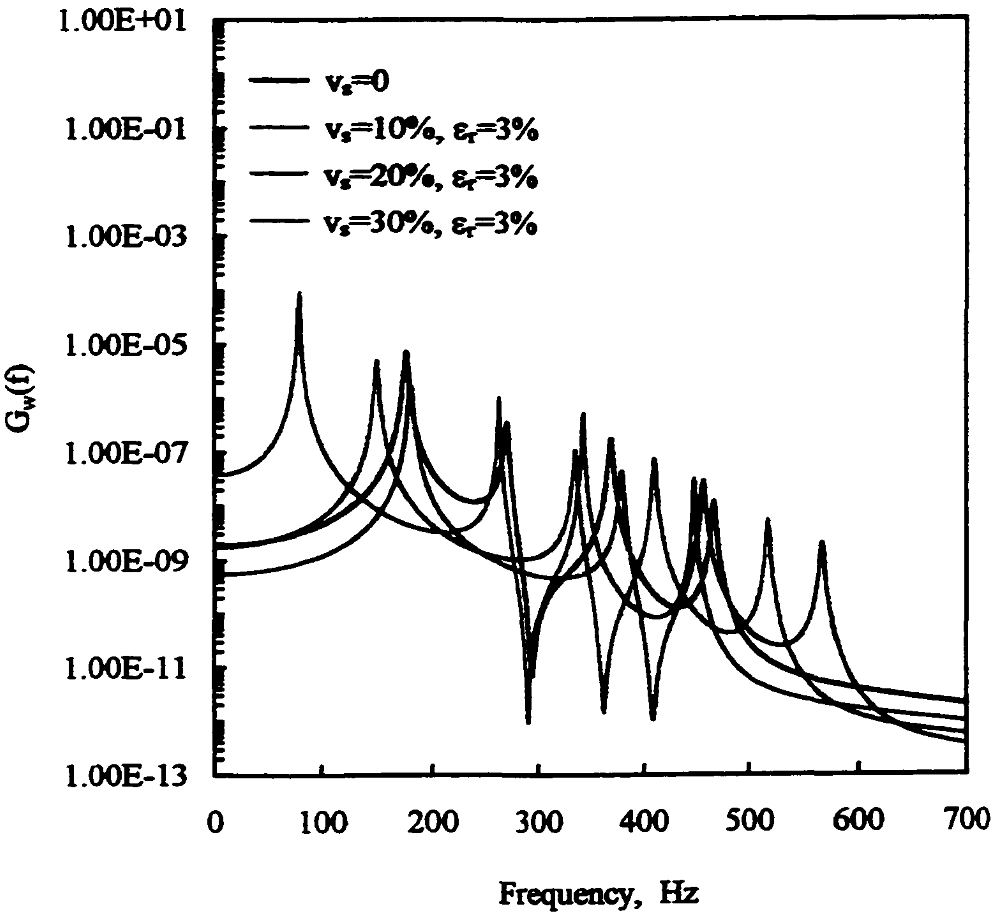

Fig. 4.30 Power Spectral Density of Wmax/h at 170°F and 100dB SSL
(v_s=0, 10, 20, 30%, ε_T=3%)

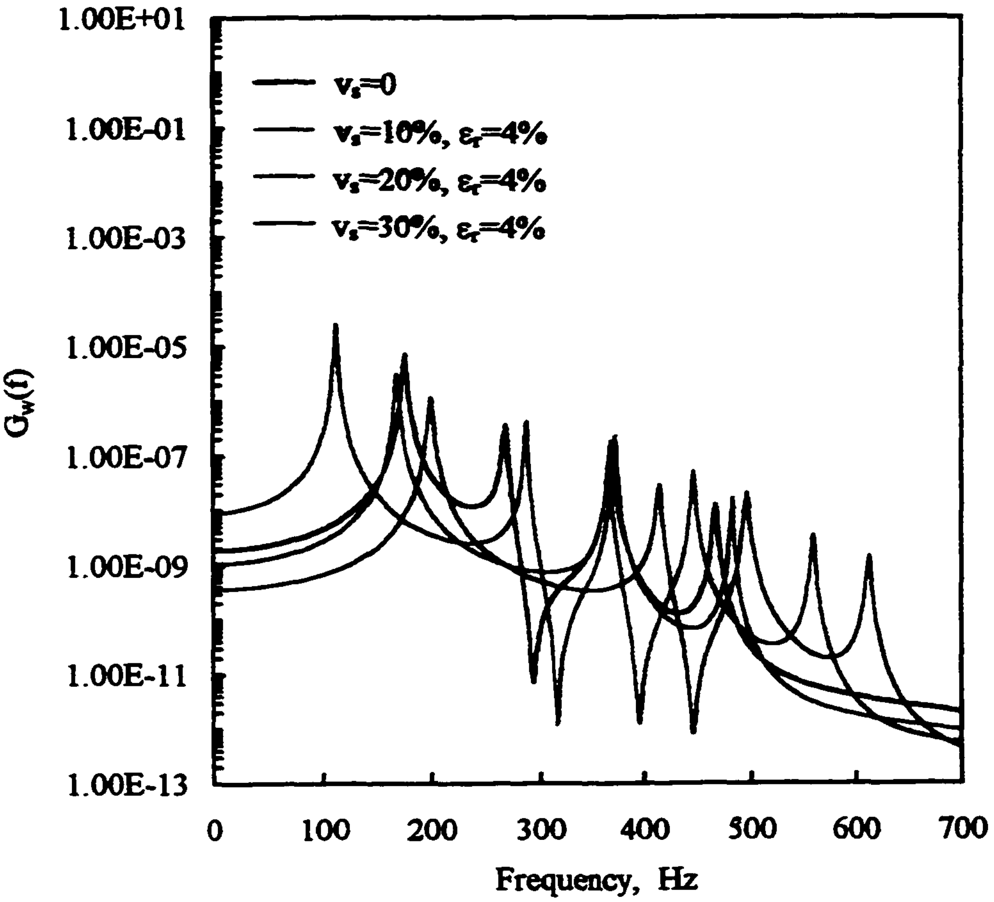

Fig. 4.31 Power Spectral Density of Wmax/h at 170°F and 100dB SSL (v_s=0, 10, 20, 30%, ε_r=4%)

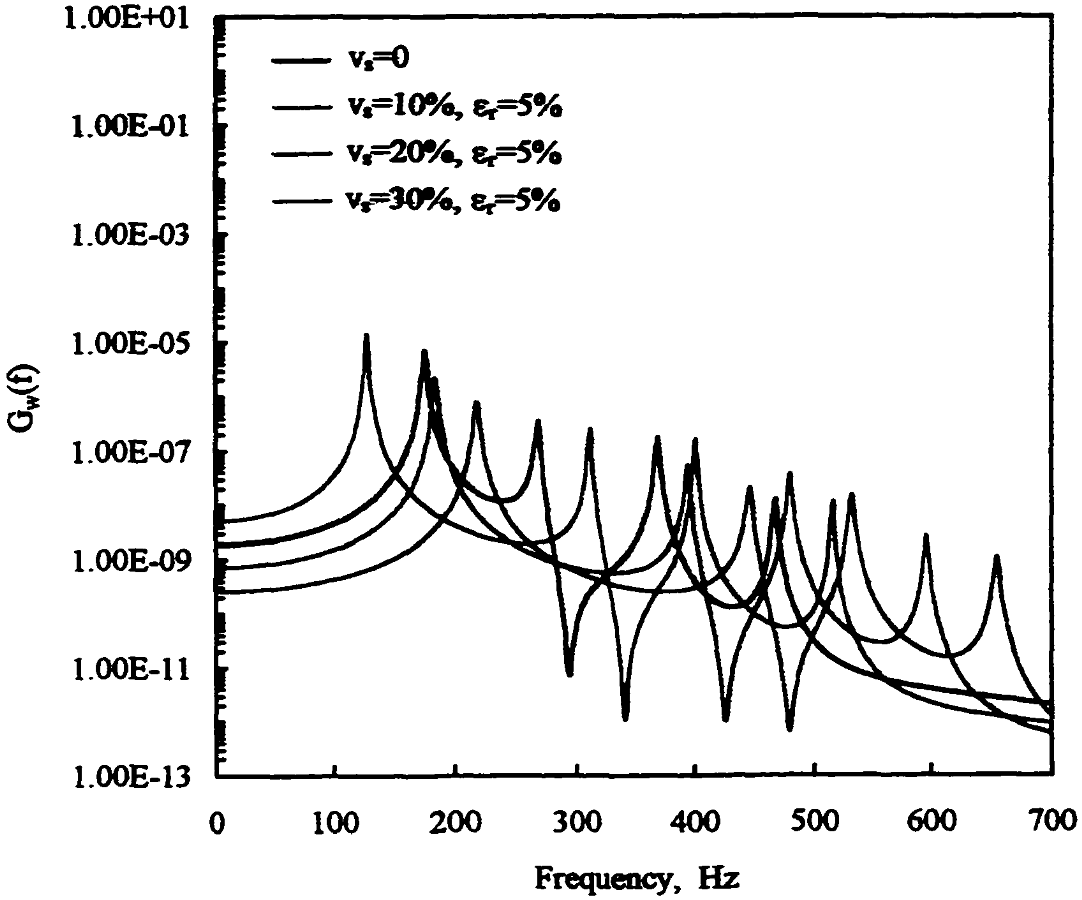

Fig. 4.32 Power Spectral Density of Wmax/h at 170°F and 100dB SSL ($v_s=0$, 10, 20, 30%, $\varepsilon_r=5\%$)

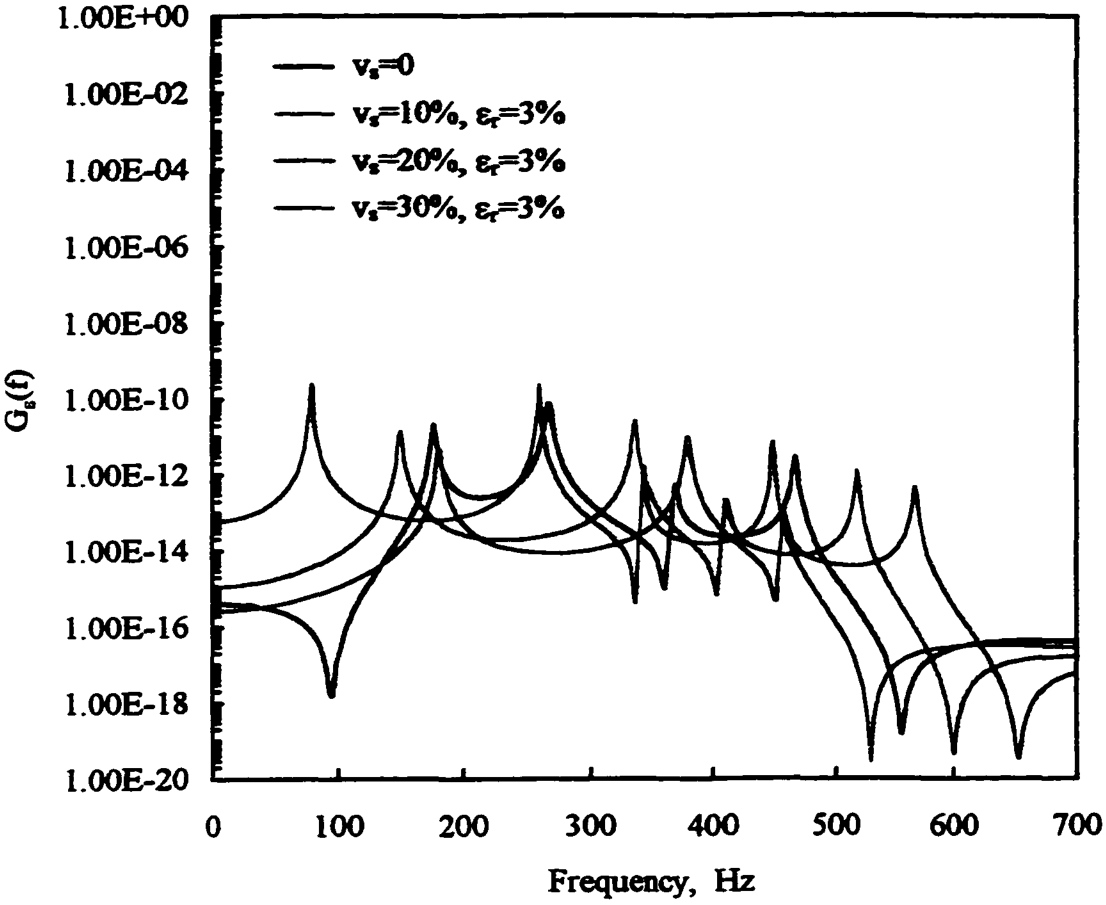

Fig. 4.33 Power Spectral Density of ε_{max} at 170°F and 100 dB SSL (v_s=0, 10, 20, 30%, ε_r=3%)

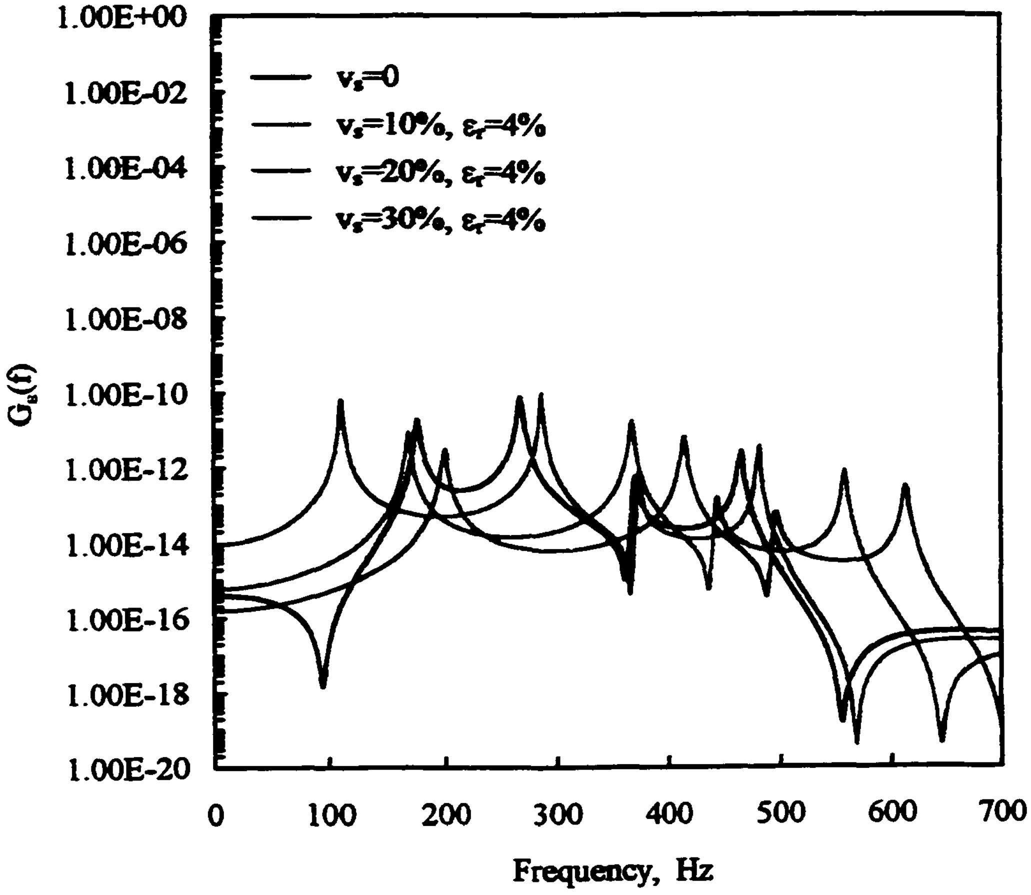

Fig. 4.34 Power Spectral Density of ε_{max} at 170°F and 100 dB SSL (v_s=0, 10, 20, 30%, ε_T=4%)

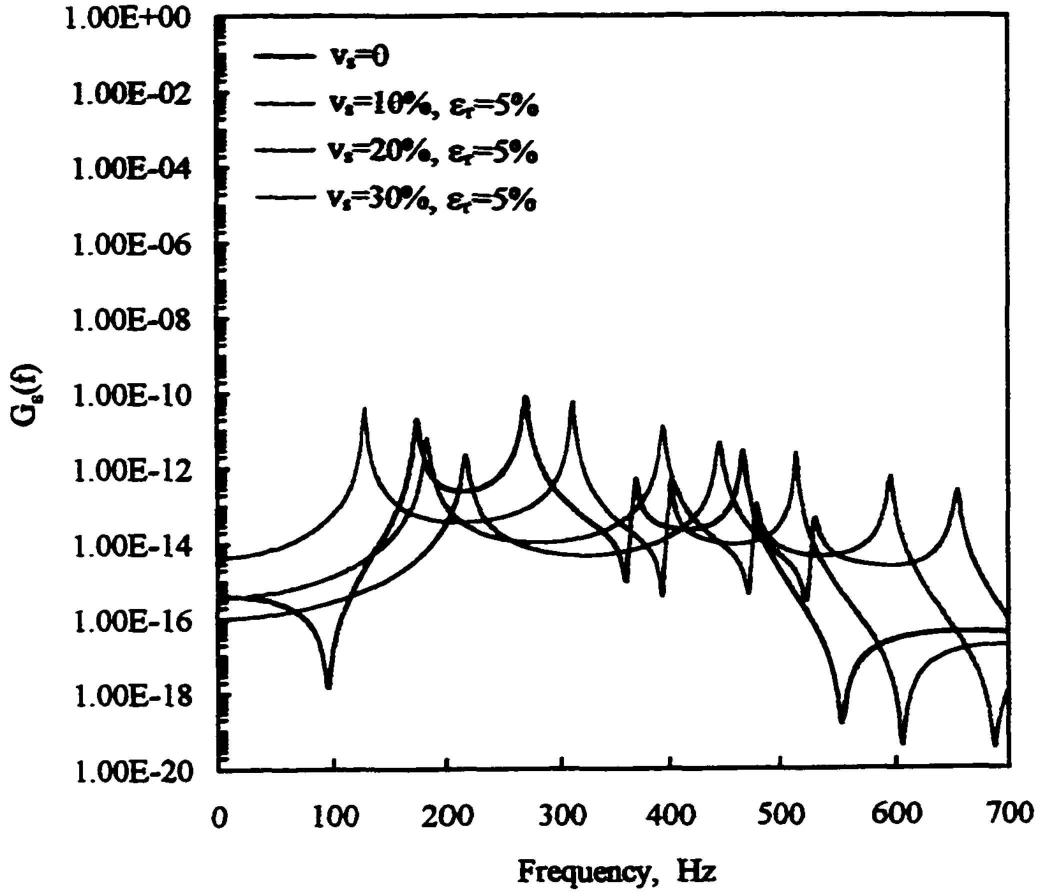

Fig. 4.35 Power Spectral Density of ε_{max} at 170°F and 100 dB SSL (v_s=0, 10, 20, 30%, ε_r=5%)

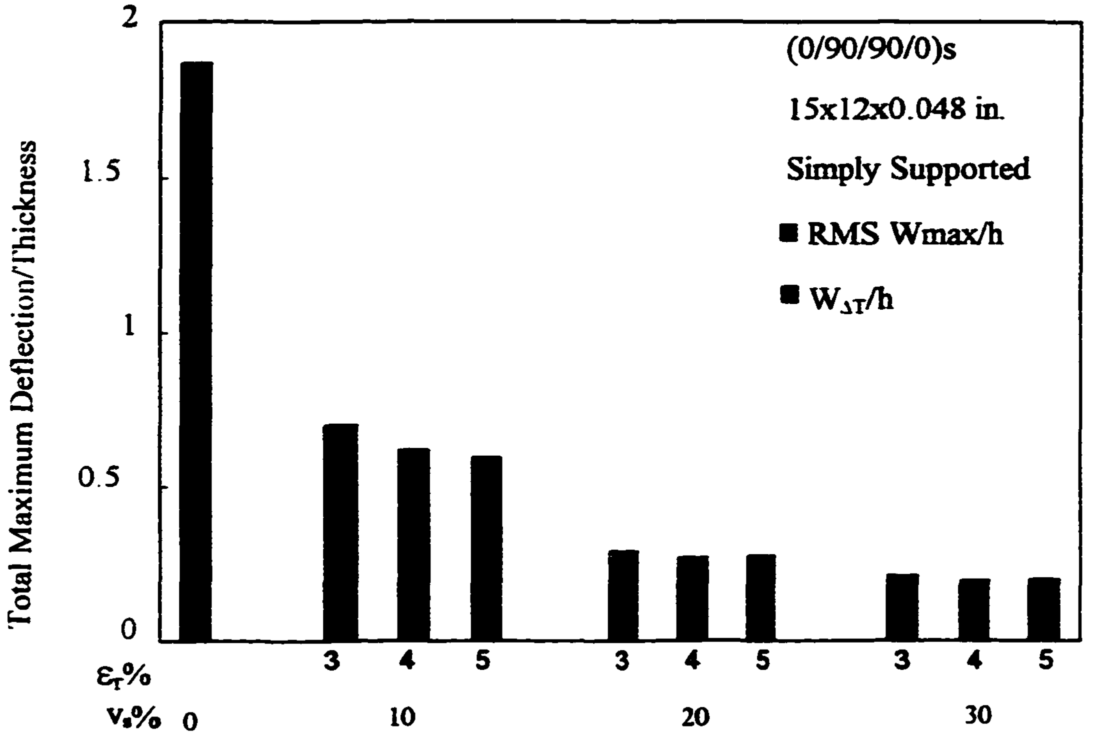

Fig. 4.36 Total Maximum Deflection/Thickness at 170 °F and 100dB SSL

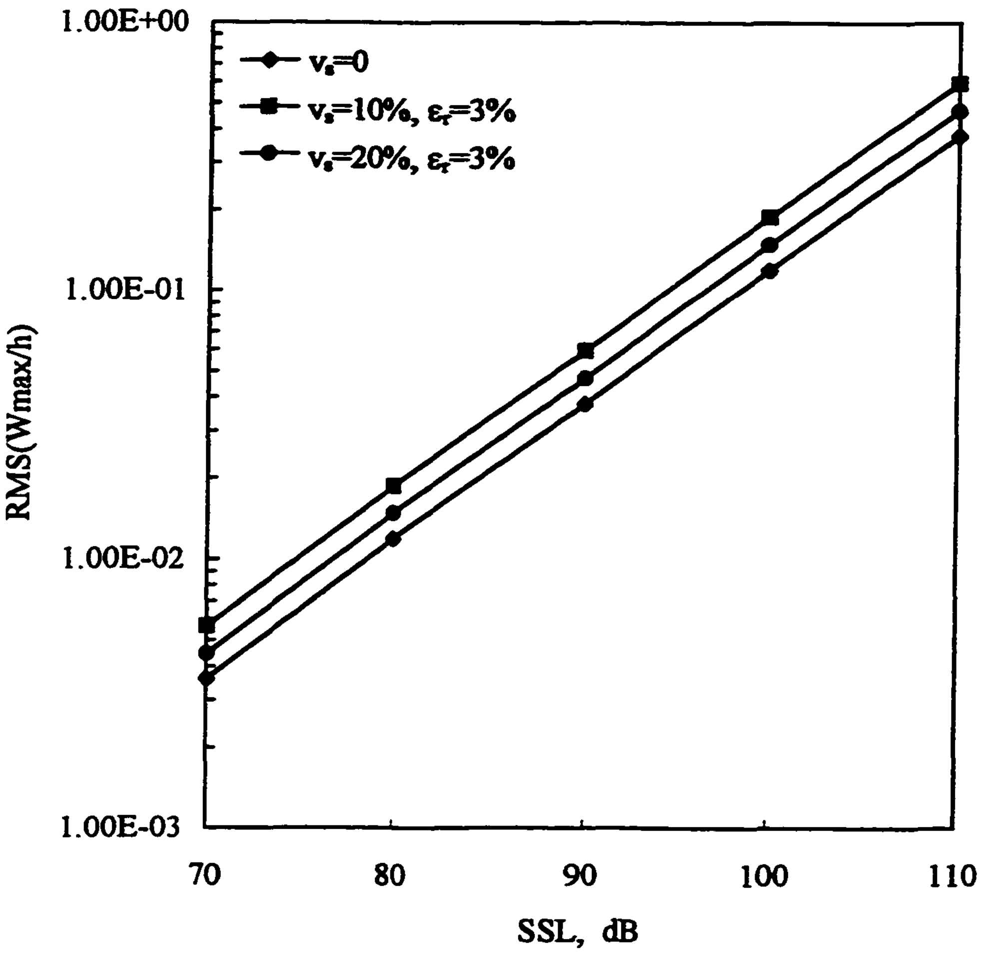

Fig. 4.37 RMS(Wmax/h) versus Sound Spectrum Level at 300°F (v_s=0, 10, 20%, ε_T=3%)

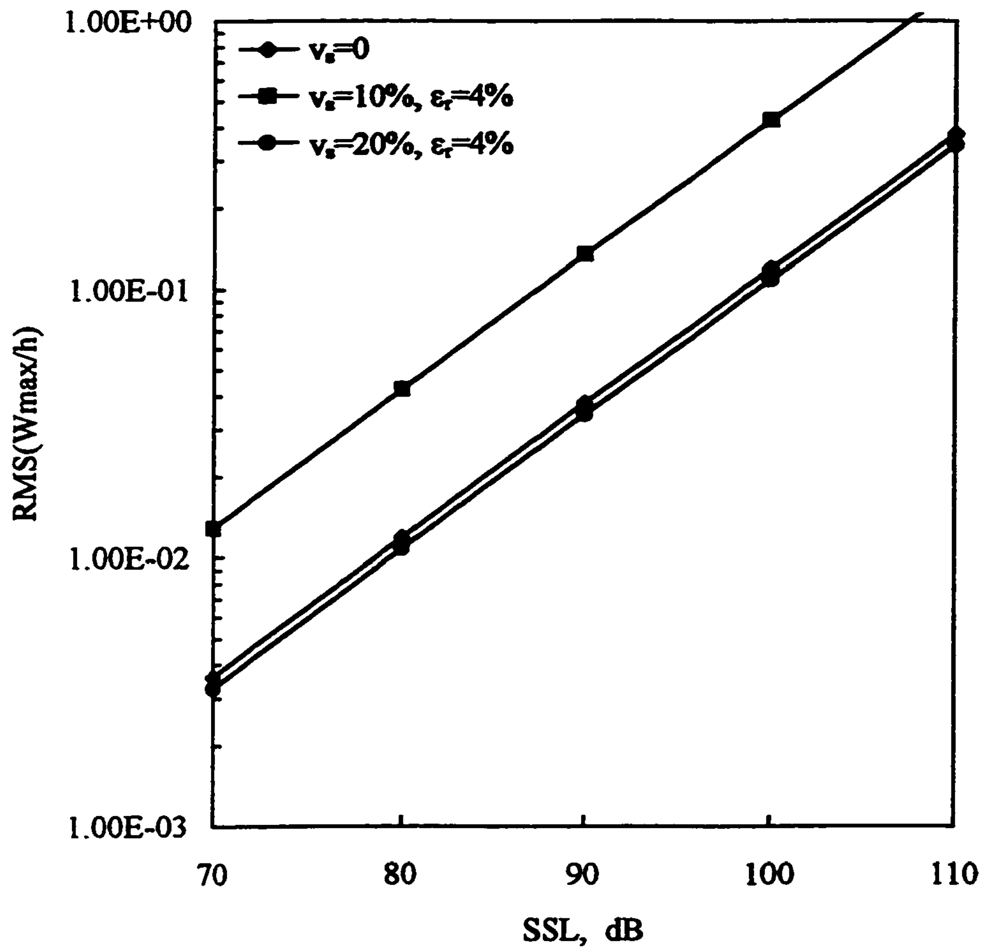

Fig. 4.38 RMS(Wmax/h) versus Sound Spectrum Level at 300°F (v_s=0, 10, 20%, ε_T=4%)

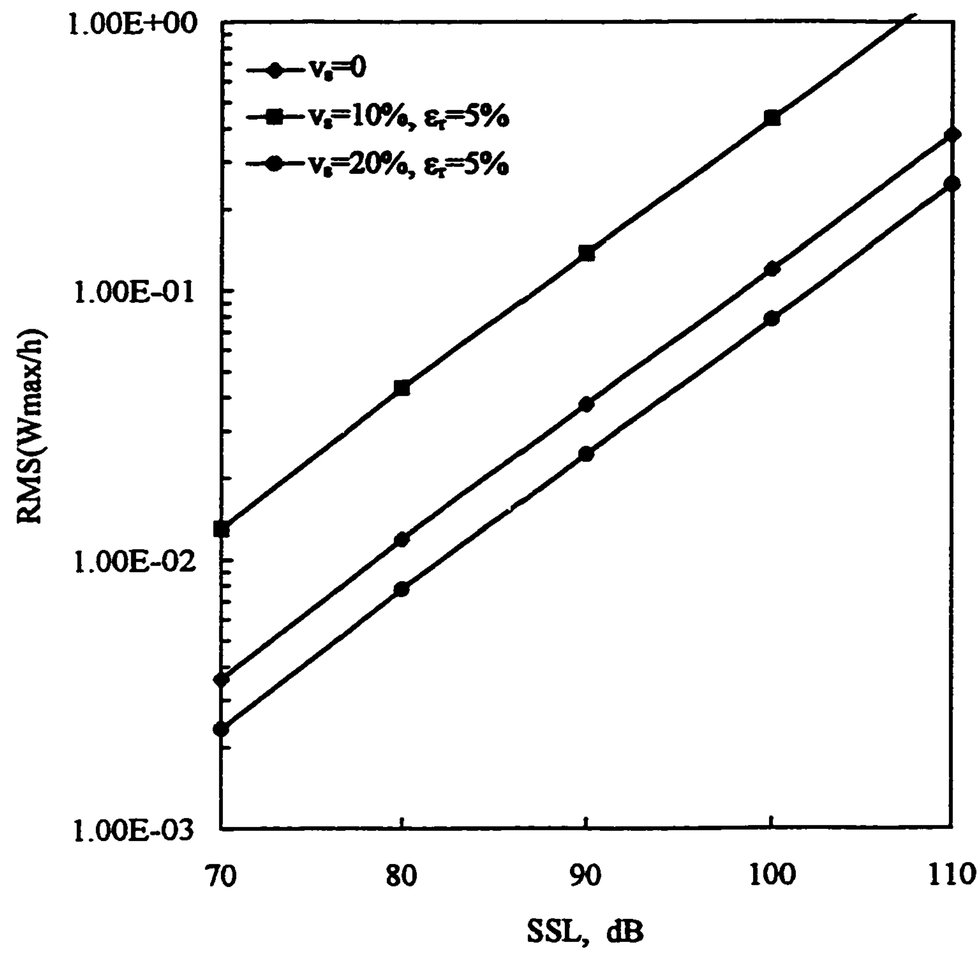

Fig. 4.39 RMS(Wmax/h) versus Sound Spectrum Level at 300°F (v_s=0, 10, 20%, ε_T=5%)

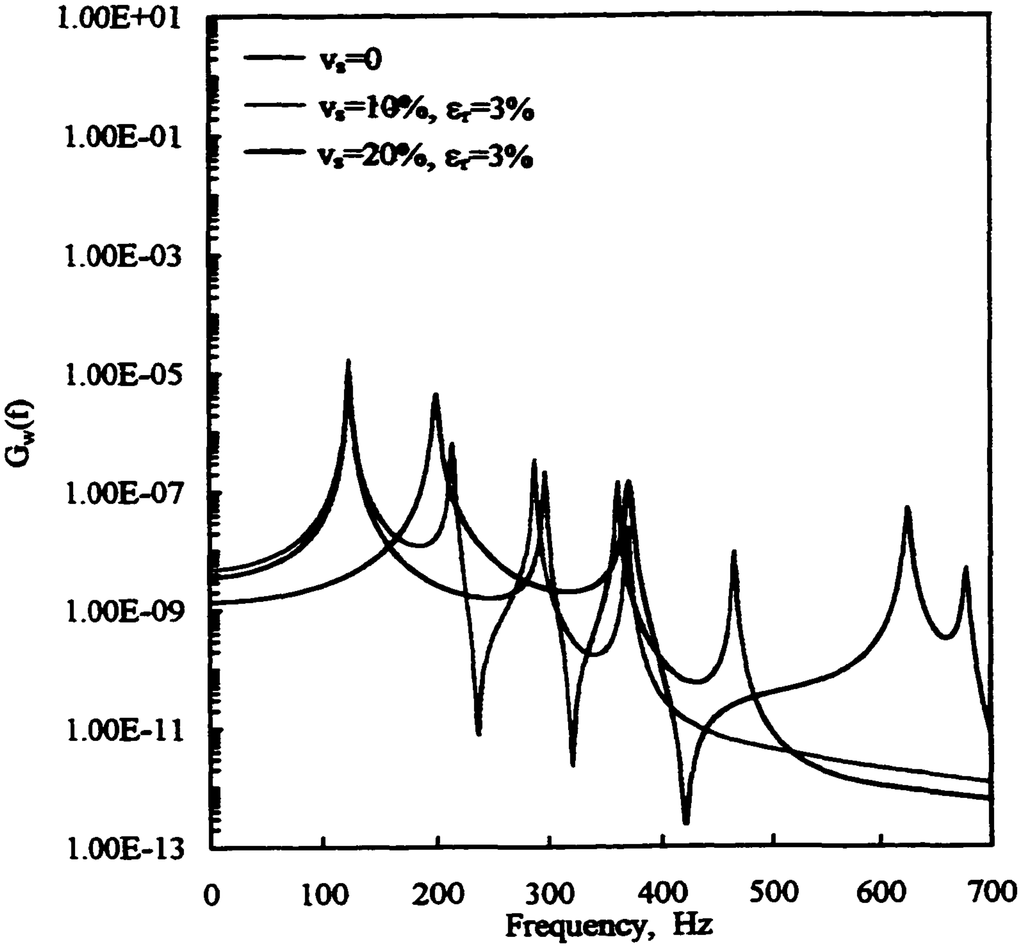

Fig. 4.40 Power Spectral Density of Wmax/h at 300°F and 100 dB SSL
(v_s=0, 10, 20%, ε_r=3%)

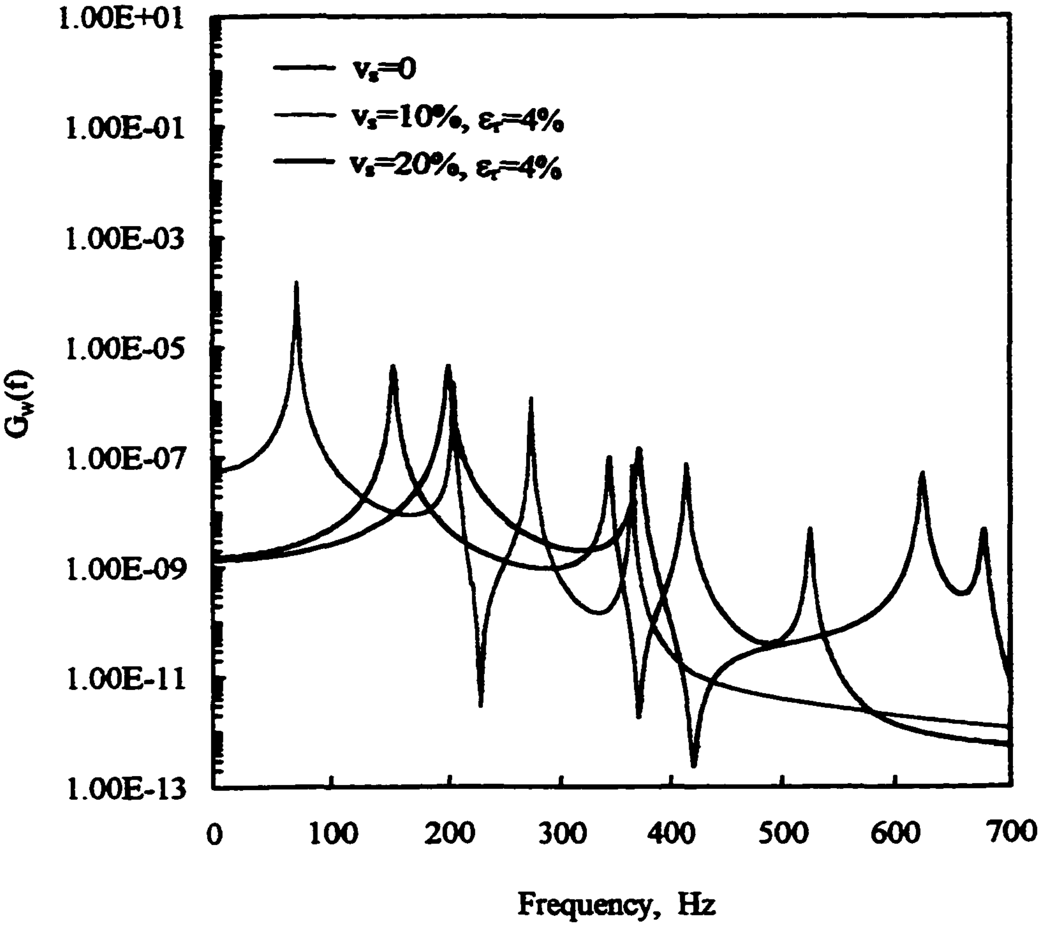

Fig. 4.41 Power Spectral Density of Wmax/h at 300°F and 100 dB SSL (v_s=0, 10, 20%, ε_T=4%)

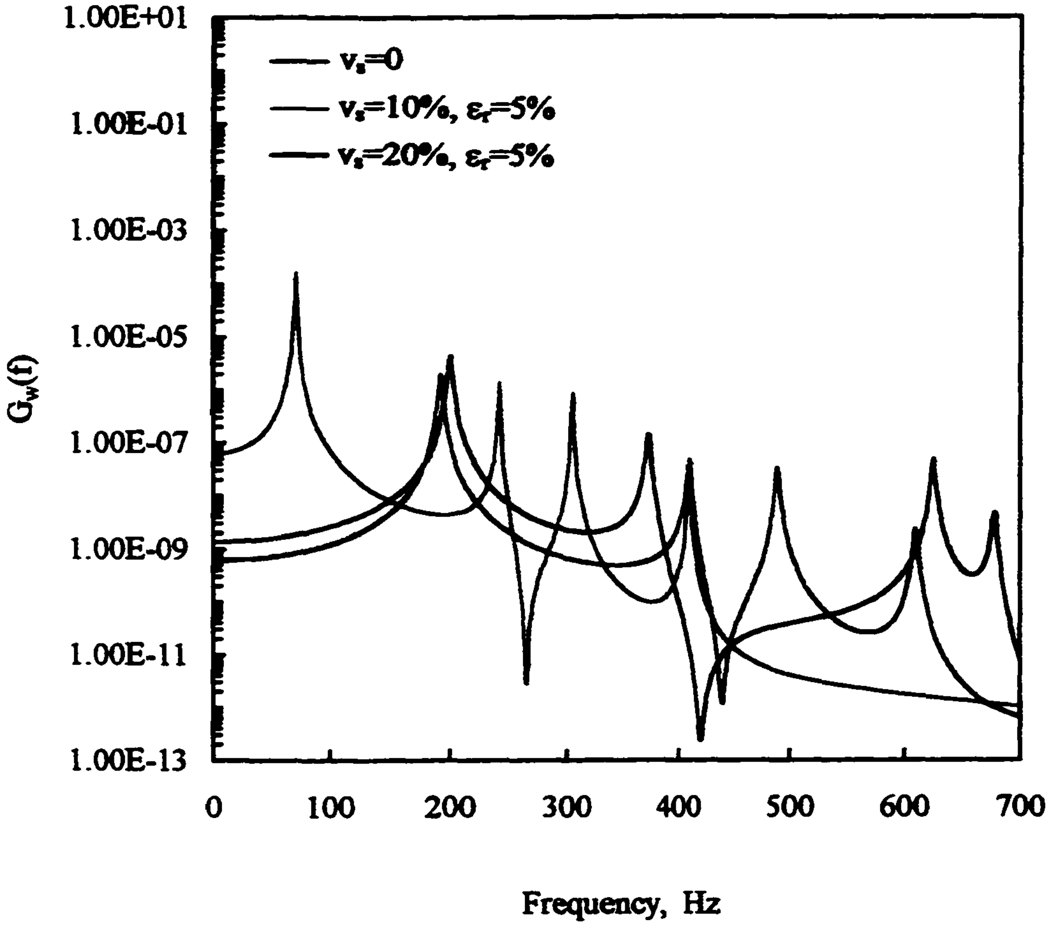

Fig. 4.42 Power Spectral Density of Wmax/h at 300°F and 100 dB SSL ($v_s=0$, 10, 20%, $\varepsilon_r=5\%$)

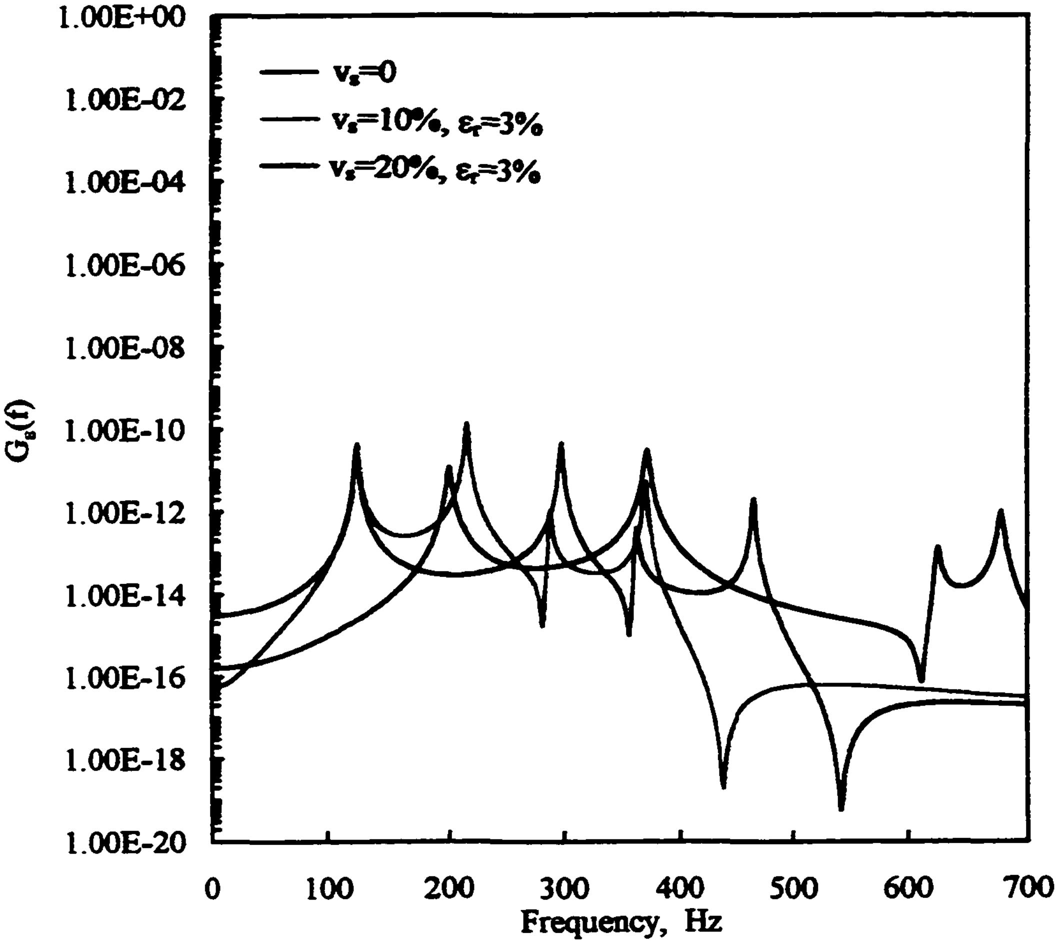

Fig. 4.43 Power Spectral Density of ε_{max} at 300°F and 100 dB SSL (v_s=0, 10, 20%, ε_T=3%)

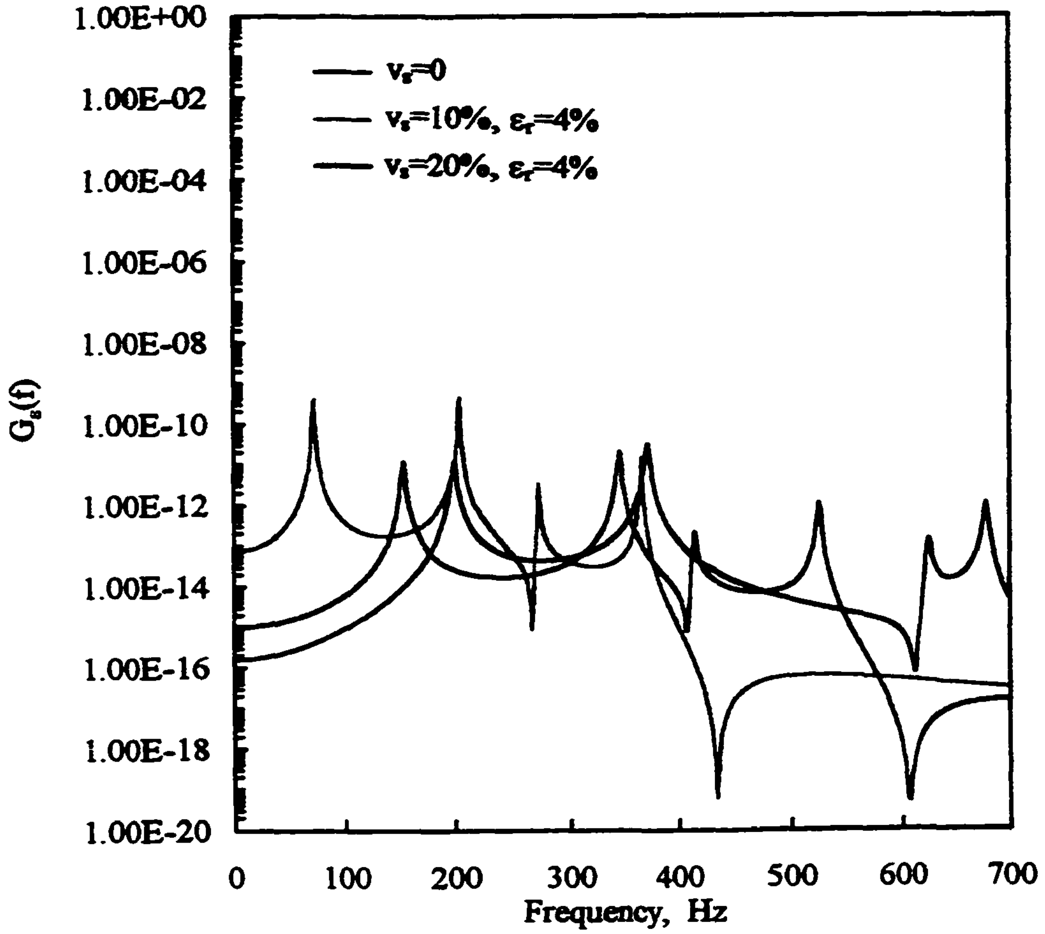

Fig.4.44 Power Spectral Density of ε_{max} at 300°F and 100 dB SSL ($v_s=0$, 10, 20%, $\varepsilon_T=4\%$)

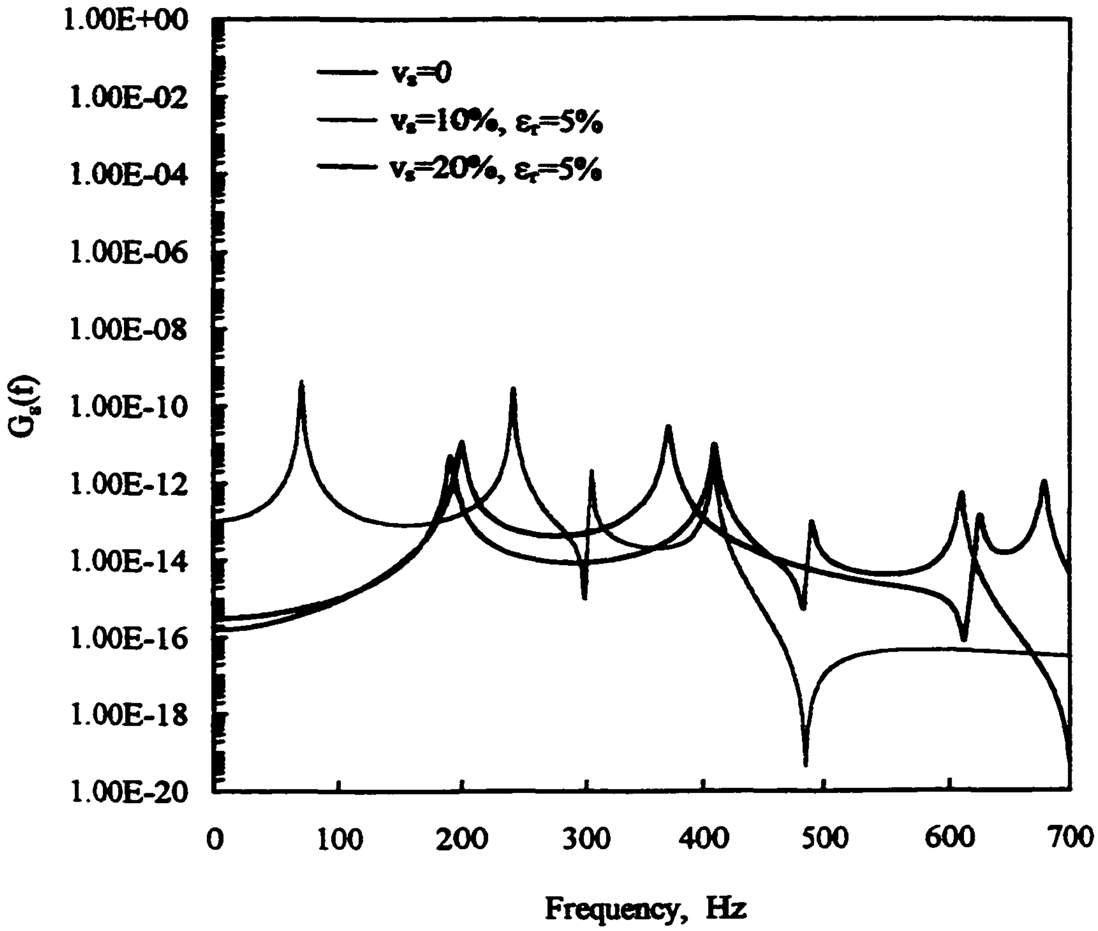

Fig 4.45 Power Spectral Density of ε_{max} at 300°F and 100 dB SSL (v_s=0, 10, 20%, ε_T=5%)

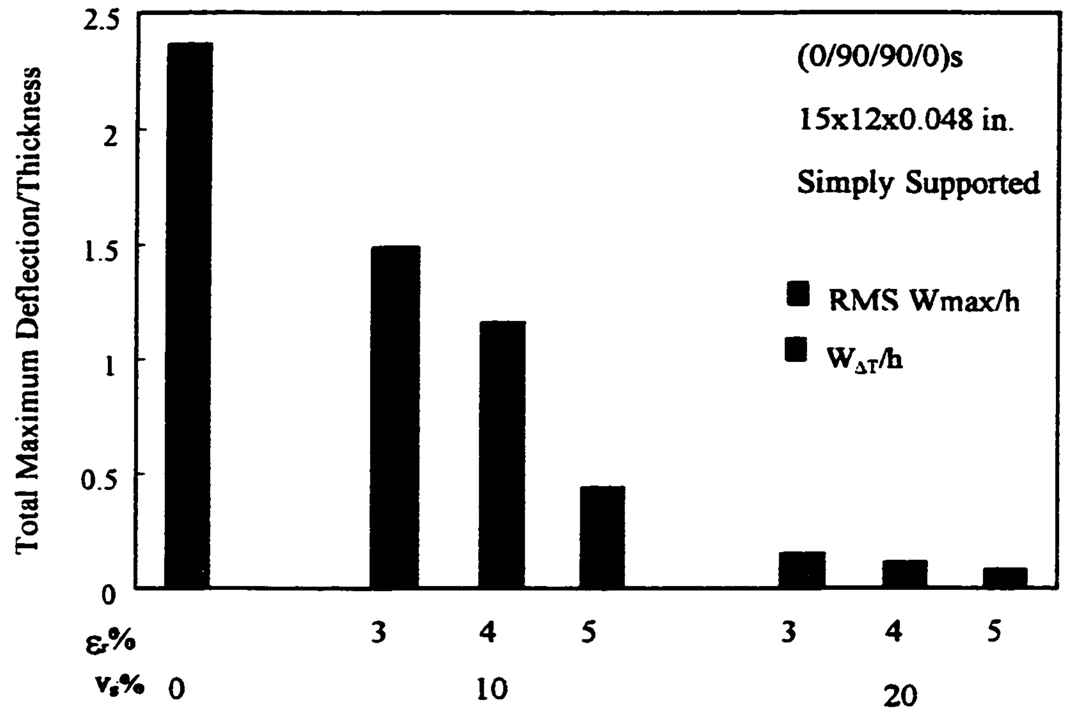

Fig. 4.46 Total Maximum Deflection/Thickness at 300°F and 100 dB

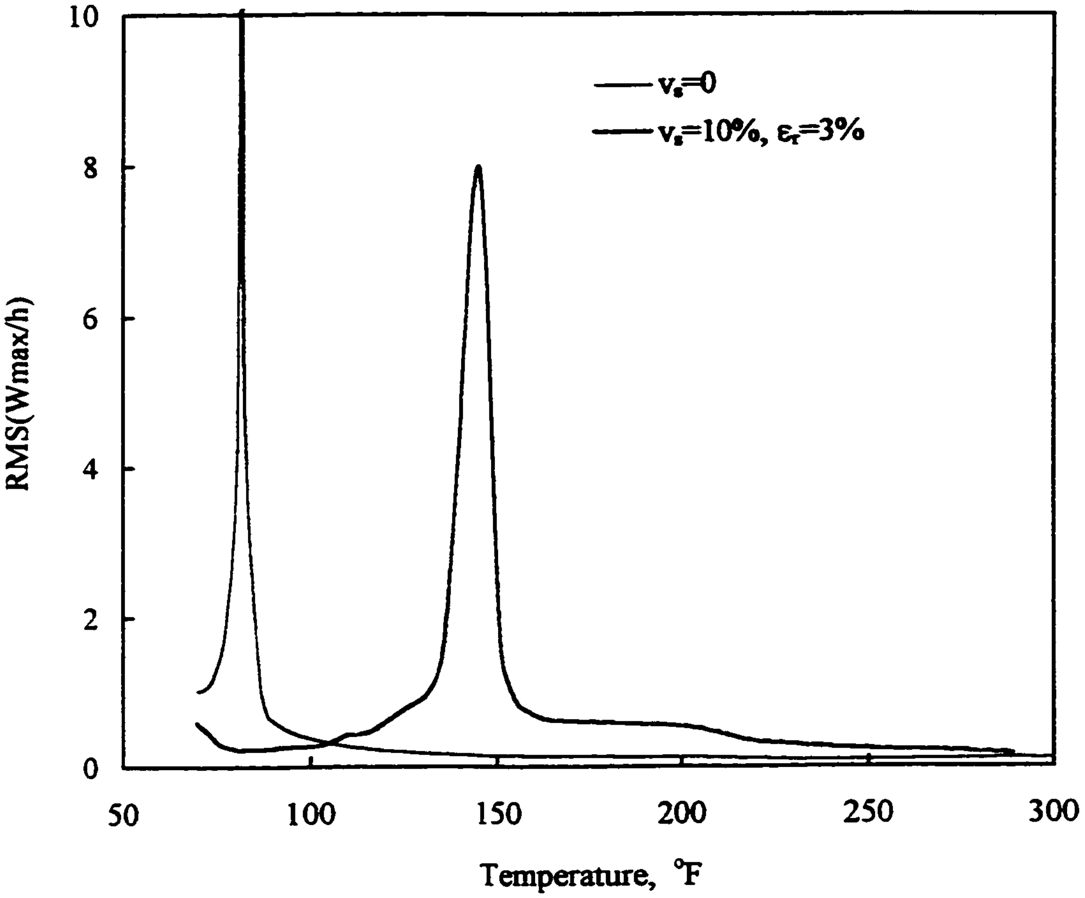

Fig. 4.47 RMS(Wmax/h) versus Temperature at 100 dB SSL
(v_s=0, 10%, ε_T=3%)

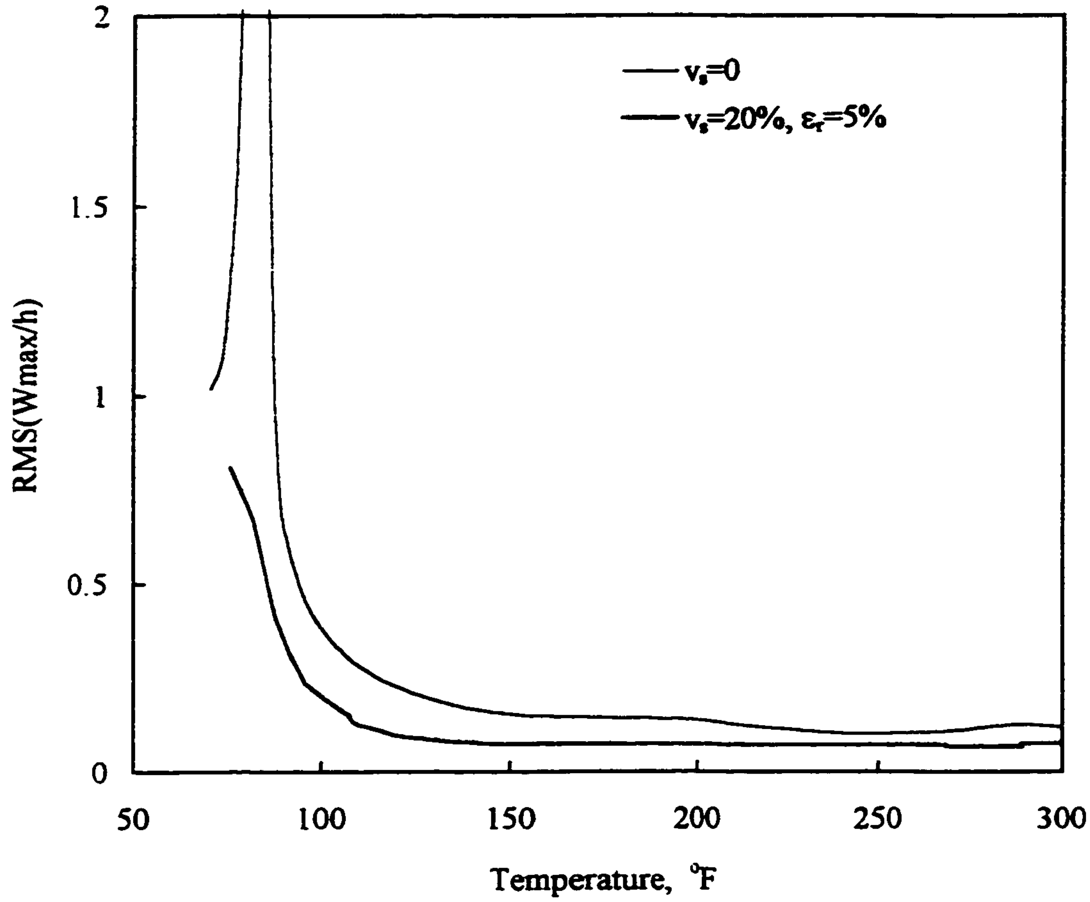

Fig. 4.48 RMS(Wmax/h) versus Temperature at 100 dB SSL
(v_s=0, 20%, ε_r=5%)

CHAPTER V

CONCLUSIONS

A feasibility study of the use of shape memory alloys on changing the behaviors of the thermal buckling, thermal postbuckling deflection, vibration and random vibration of composite structures subjected to a combined acoustic/thermal loading has been presented. The constitutive relations for a composite lamina with embedded SMA fibers have been developed. These relations include the factors of SMA material properties and temperature effects of both SMA fibers and matrix material. Based on von Karman large deflection theory and the first-order, shear-deformation theory, the finite element governing equations with the effects of nonlinear material properties of SMA are derived. The three-node Mindlin plate element with improved shear deformation has been used in the computational solutions.

In order to solve the system equation of motion, the total response is assumed to be the sum of static and dynamic components. Substituting the total displacements into the system equation of motion and regrouping the terms, the equation is of the form $F(\{W\}_s)=G(\{W\}_t)$. The left hand side of the equation is time independent while the right hand side is dependent of time. Therefore, the only possibility for both F and G to exist is that both F and G equal to zero. Thus, the two equations are obtained.

A consistent two-step solution procedure has been developed for solving the static and dynamic problems of composite structures with embedded SMA fibers subjected to combined acoustic and thermal loads. With the consideration of nonlinear material properties of SMA and geometrically nonlinear deflection, an incremental technique and the Newton-Raphson iteration method have been employed to determine the static responses of the SMA embedded composite structures. For the solution of dynamic equation, a modal transformation is used to reduce the number of equations and uncouple the equation of motion.

Thermal buckling behavior of composite plates with and without embedded SMA fibers has been studied first. The critical buckling temperature of the plate with SMA fibers is slightly lower than that of the plate without SMA while the austenite start temperature of SMA is 100°F. This is because that the SMA fibers have relatively low modulus compared to the matrix material and the shape memory effects are not active when temperature is lower than T_s. However, by changing the Nickel composition in SMA, the austenite start temperature of SMA can be altered to 70°F. The change of the austenite start temperature results in the increase of the critical buckling temperature of composite structures with embedded SMA and creates the optimal design area for the composite structures which can potentially be used for high speed flight vehicles.

As one of the most significant contributions to the present research, the study of the thermal postbuckling deflection of SMA hybrid composite structures has revealed the possibility to reduce the thermal deflection of structures at elevated temperatures by changing the volume fraction, prestrain, austenite start temperature of SMA, as well as stacking sequence and boundary condition of structures. The results indicate that the thermal deflection can be completely eliminated for the plate with proper prestrain and volume fraction of SMA. In addition, with the change of austenite start temperature from 100°F to 70°F, the critical buckling temperature can be shifted well above the operating temperature (300°F) in most cases and thus the thermal deflection can be totally eliminated within the entire operating temperature range. This effect could be useful in practical applications by maintaining optimal aerodynamic configuration and eliminating snap-through motions.

Vibrations about the thermally buckled position of the SMA hybrid composite structures has been studied. The purpose of this study is to understand the vibration behavior of the composite structures with embedded SMA fibers and to obtain the natural frequencies and mode shapes which can be used in the solution procedure for random vibration analysis. The results reveal that the characteristic of SMA plays an important role in the dynamic response of structures. The mode shape corresponding to the lowest natural frequency can be changed from (1,1) to (2,1) for the plate without SMA, however, this never happened for the SMA fiber-reinforced composite structures.

The random response analysis of SMA hybrid composite structures is a significant contribution to the present research. An ideal SMA fiber-reinforced composite structure, which can be used for the application to high performance flight vehicles, is to have no thermal deflection at all and very small dynamic response subjected to the combined thermal and acoustic loads. The present investigation of random response provides a design methodology for the SMA hybrid composite structures to meet the application requirements. Although the dynamic response of plate with some of the lower SMA volume fractions and prestrains is actually greater than that of the plate without SMA fibers, significant dynamic response attenuation may be achieved with SMA volume fractions of thirty percent or more when the austenite start temperature of SMA is 100°F. The RMS maximum deflection increases for some SMA volume fractions because of two factors: the modulus of the SMA fibers is relatively low, even at high temperatures; and the recovery forces induced by small volume fraction of SMA fibers is not sufficient to overcome the loss of the buckling stiffness. The other effective method to eliminate the thermal deflection and reduce the random response of SMA hybrid composite structures is to alter the austenite start temperature. The results indicate that with the change of austenite start temperature from 100°F to 70°F, the thermal deflection can be completely eliminated and the random response can be greatly reduced within the entire operating temperature range considered, even with a small volume fraction of SMA. These benefits will: 1) maintain the originally designed optimal aerodynamic efficiency at high temperatures during cruise, and 2)result in lower interior noise and longer service life.

The applications of SMA fiber-reinforced composite structures create a lot of research area. Following the present research, the investigation on panel flutter using SMA hybrid composite structures and the study on superelastic characteristic of SMA material and its application are the open topics for future research.

REFERENCES

1. Bueher, W. J. and Wang, F. E., "A Summary of Recent Research On The Nitinol Alloys and Their Potential Application In Ocean Engineering," *Ocean Engineering*, Vol. 1, 1967, pp. 105-120.

2. Cross, W. B., Kariotis, A. H. and Stimler, F. J., "Nitinol Characterization Study," NASA CR-1433, 1970.

3. Jackson, C. M., Wagner, H. J. and Wasilewski, R. J., "55-Nitinol - The Alloy with a Memory: Its Physical Metallurgy, Properties, and Applications," NASA-SP-5110, p. 91, 1972.

4. Schetky, F., "Shape Memory Alloys," *Scientific American*, Vol. 241, 1979, p. 74.

5. Wayman, C. M. and Shimizu, K., "The Shape Memory ('Marmem') Effect in Alloys," *Metal Science Journal*, Vol. 6, 1972, p. 175.

6. Liang, C. and Rogers, C. A., "One-Dimensional Thermomechanical Constitutive Relations for Shape Memory Materials," *Journal of Intelligent Material Systems and Structures*, Vol. 1. No. 2, 1990, pp. 207-234.

7. Goldstein, D., "A Source Manual for Information on Nitinol and NiTi," Naval Surface Weapons Center, Silver Spring, MD, 1978, Report NSWC/WOL TR 78-26.

8. Achenbach, M., "A Model for an Alloy with Shape Memory," *International Journal of Plasticity*, Vol. 5, 1989, pp. 371-395.

9. Tanaka, K., "A Thermomechanical Sketch of Shape Memory Effect: One-dimensional Tensile Behavior," *Research Mechanica*, Vol. 18, 1986, pp. 251-263.

10. Liang, C. and Rogers, C. A., "The Multi-Dimensional Constitutive Relations of Shape Memory Alloys," Proceedings of 32nd Structures, Structural Dynamics and Materials Conference, Baltimore, MD, April 8-10, 1991, AIAA-91-1165-CP, pp. 178-185.

11. Brinson, L. C., "Constitutive Behavior of Shape Memory Alloys: One Dimensional Thermomechanical Derivation with Non-Constant Material Functions and Redefined Martensite Internal Variable," *Journal of Intelligent Material Systems and Structures*, Vol. 4, 1993, pp. 229-242.

12. Hebda, D. A., Whitlock, M. E., Ditman, J. B. and White, S. R., "Manufacturing of Adaptive Graphite/Epoxy Structures with Embedded Nitinol Wires," *Journal of Intelligent Material Systems and Structures*, Vol. 6, March 1995, pp. 220-228.

13. Mooi, H., "Active Control of Structural Paramenters of a Composite Strip Using Embedded Shape Memory Alloy Wires", DLR Report IB 232-92 J02, 1992.

14. Maclean, B. J., Carpenter, B. F., Draper, J. L. and Misra, M. S., "A Shape Memory Actuated Compliant Control Surface," Proceedings of Smart Structures and Intelligent Systems Conference, Feb. 1-4, 1993, Albuquerque, MN, SPIE Vol. 1917, pp. 809-818.

15. Baz, A. and Chen, T., "Performance of Nitinol Reinforced Drive Shaft," Proceedings of Smart Structures and Intelligent Systems Conference, Feb. 1-4, 1993, Albuquerque, MN, SPIE Vol. 1917, pp. 791-808.

16. Chandra, R., "Active Strain Energy Turning of Composite Beams Using Shape Memory Alloy Actuators," Proceedings of Smart Structures and Intelligent Systems Conference, Feb. 1-4, 1993, Albuquerque, MN, SPIE Vol. 1917, pp. 267-283.

17. Chaudhry, Z. and Rogers, C. A., "Response of Composite Beams to an Internal Actuator Force," *Journal of Mechanical Design*, Vol. 114, No. 3, 1992, pp. 343-348.

18. Paine, J. S. N., Jones, W. M. and Rogers, C. A., "Nitinol Actuator-Host Composite Interfacial Adhesion in Adaptive Hybrid Composites," Proceedings of 33rd Structures, Structural Dynamics and Materials Conference, Dallas, TX, April 12-16, 1992, AIAA-92-2405-CP, Part 2, pp. 556-565.

19. Paine, J. S. N. and Rogers, C. A., "Characterization of Interficial Shear Strength Between SMA Actuators and Host Composite Material in Adaptive Composite Material Systems," Adaptive Structures and Material Systems, AD-Vol. 35, 1993, ASME Winter Annual Meeting, pp. 63-70.

20. White, S. R., Whitlock, M. E., Ditman, J. B. and Hebda, D. A., "Manufacturing of Adaptive Graphite/Epoxy Structures with Embedded Nitinol Wires," Adaptive Structures and Material Systems, AD-Vol. 35, 1993, ASME Winter Annual Meeting, pp.71-79.

21. Ro, J. and Baz, A., "Nitinol-Reinforced Plates: Part II. Static and Buckling Characteristics," *Composites Engineering*, Vol. 5, No. 1, 1995, pp. 77-90.

22. Baz, A. and Tempe, L., "Active Control of Buckling of Flexible Beams," ASME DE-Vol. 16, Proceedings of 8th Biennial Conference on Failure Prevention and Reliability, Montreal, Canada, ASME, NY, 1989, pp. 211-218.

23. Baz, A., Ro, J., Mutua, M. and Gilheany, J., "Active Control of Buckling of NITINOL-Reinforced Composite Beams," Active Materials and Adaptive Structures Conference, Arlington, VA, 1991, pp. 167-176.

24. Baz, A., Poh, S., Ro, J., Mutua, M. and Gilheany, J., "Active Control of Nitinol-Reinforced Composite Beam," *Intelligent Structural Systems*, Eds. Tzou, H. S. and Anderson, G. L., Kluver Academic Publishers, Dordrecht, Netherlands, 1992, pp. 169-212.

25. Baz, A. and Chen, T., "Active Control of the Lateral Buckling of Nitinol-Reinforced Composite Beams," *Active Materials and Structures*, Eds. Anderson, G. L. and Lagoudas, D. C., Proceedings of the Symposium held as part of the 31st Annual Technical Meeting of the Society of Engineering Science, SPIE, Vol. 2427, 1994, pp. 30-48.

26. Liang, C., Jia, J. and Rogers, C.A., "Behavior of Shape Memory Alloy Reinforced Composite Plates-Part II: Results," Proceedings of 30th Structures, Structural Dynamics and Materials Conference, Mobile, Alabama, April 3-5, 1989, AIAA 89-1389-CP, pp. 1504-1513.

27. Paine, J. S. N. and Rogers, C. A., "Characterization of Interfacial Sheer Strength Between SMA Actuators and Host Composite Material in Adaptive Composite Material Systems," Adaptive Structures and Material System, AD-Vol. 35, 1993 ASME Winter Annual Meeting, pp. 63-70.

28. Rogers, C. A., Liang. C. and Jia, J., "Structural Modification of Simply-supported Laminated Plates Using Embedded Shape Memory Alloy Fibers," *Computers and Structures*, Vol. 38, No. 5/6, 1991, pp. 569-580.

29. Paine, J. S. N., Rogers, C. A. and Smith, R. A., "Adaptive Composite Materials with Shape Memory Alloy Actuators for Cylinders and Pressure Vessels," *Journal of Intelligent Material Systems and Structures*, Vol. 6, 1995, pp. 210-219.

30. Brand, W., Boller, C., Huang, M. S. and Brinson, L. C., "Introducing the Constitutive Behavior of Shape Memory Alloys into Adaptive Engineering Structures," *Mechanics of Phase Transformations and Shape Memory Alloys*, Eds. Brinson, L. C. and Moran, B., ASME, New York, 1994, pp. 179-193.

31. Lagoudas, D. C. and Bo, Z., "The Cylindrical Bending of Composite Plates with Piezoelectric and SMA Layers," *Smart Materials and Structures*, Vol. 3, 1994, pp. 309-317.

32. Yoshida, H., "Creation of Environmentally Responsive Composites with Embedded Ti-Ni Alloy as Effectors," *Advances in Composite Materials*, Vol. 5, 1995, pp. 1-16.

33. Birman, V. and Simonyan, A., "Optimum Design of Sandwich Panels with Piezoelectric or Shape Memory Alloy Actuators," Proceedings of the 1995 Design Engineering Technical Conferences, Vol. 3, Part C, Vibration Control Analysis and Identification, Eds. Wang, K. W. et al., ASME, New York, 1995, pp. 627-637.

34. Birman, V., Saravanos, D. A. and Hopkins, D. A., "Micromechanics of Composites with Shape Memory Alloy Fibers in Uniform Thermal Fields," NASA TM-106611, 1995.

35. Rogers, C. A., Liang, C. and Jia, J., "Behavior of Shape Memory Alloy Reinforced Composite Plates. Part I: Model Formulation and Control Concepts," Proceedings of the 30th AIAA/ASME/ASCE/AHS/ASC Structures, Structural Dynamics and Materials Conference, 1989, pp. 2011-2017, AIAA Paper AIAA-89-1389-CP.

36. Rogers, C. A., "Active Vibration and Structural Acoustic Control of Shape Memory Alloy Hybrid Composites: Experimental Results," *Journal of Acoustical Society of America*, Vol. 88, 1990, pp. 2803-2811.

37. Rogers, C. A., Liang, C. and Fuller, C. R., "Modeling of Shape Memory Alloy Hybrid Composite for Structural Acoustic Control," *Journal of Acoustical Society of America*, Vol. 89, No.1, 1991, pp. 210-220.

38. Anders, W. S., Rogers, C. A. and Fuller, C. R., "Control of Sound Radiation from Shape Memory Alloy Hybrid Composite Panels by Adaptive Alternate Resonance Tuning," Proceedings of the 32nd AIAA/ASME/ASCE/AHS/ASC Structural Dynamics and Materials Conference, Part 1, 1991, pp. 159-168. AIAA Paper AIAA-91-1163-CP.

39. Anders, W. S., Rogers, C. A. and Fuller, C. R., "Vibration and Low Frequency Acoustic Analysis of Piecewise-Activated Adaptive Composite Panels," Journal of Composite Materials, Vol. 26, No. 1, 1992, pp. 103-120.

40. Barker, D. K., "Active Dynamic Response Tuning of Adaptive Composites Using Embedded Nitinol Actuators," M.S. Thesis, 1989, Department of Mechanical Engineering, Virginia Polytechnic Institute and State University, Blacksburg, Virginia.

41. Baz, A., Iman, K. and McCoy, J., "Active Vibration Control of Flexible Beams Using Shape Memory Actuators," *Journal of Sound and Vibration*, Vol. 140, No. 3, 1990, pp. 437-456.

42. Srinivasan, A. V., Cutts, D. G. and Schetky, L. M., "Thermal and Mechanical Considerations in Using Shape Memory Alloys to Control Vibrations in Flexible Structures," *Metallurgical Transactions*, Vol. 22A, 1991, pp. 623-627.

43. Venkatesh, A. Hilborn, J. -E. and Gotthardt, R., "Active Vibration Control of Linkage Mechanisms Using Shape Memory Alloy Fiber-Reinforced Composites," Proceedings of the First European Conference on Smart Structures and Materials, Eds. Culshaw, B., Gardiner, P. T. and McDonach, A., IP Publishing and EOS/SPIE, SPIE, Vol. 1777, 1992, pp. 185-188.

44. Shahin, A. R., Meckl, P. H. and Jones, J. D., "Vibration Control Using Shape Memory Alloy Wires," Adaptive Structures and Composite Materials: Analysis and Application, AD-Vol. 45/MD-Vol.54, ASME, 1994, pp. 227-234.

45. Baz, A. and Ro, J., "Thermo-dynamic Characteristics of Nitinol-Reinforced Composite Beams," *Composite Engineering*, Vol. 2, No. 5-7, 1992, pp. 527-542.

46. Baz, A. and Ro, J., "Optimal Vibration Control of Nitinol-Reinforced Composites," *Composites Engineering*, Vol. 4, 1994, pp. 567-576.

47. Baz, A., Poh, S., Ro, J. and Gilheany, J., "Control of the Natural Frequencies of Nitinol-Reinforced Composite Beams," *Journal of Sound and Vibration*, Vol. 185, No. 1, 1995, pp. 171-185.

48. Ro, J. and Baz, A., "Nitinol-Reinforced Plates: Part III. Dynamic Characteristics," *Composites Engineering*, Vol. 5, No.1, 1995, pp. 91-106.

49. Chandra, R., "Active Strain Energy Tuning Using Shape Memory Alloy Actuators," Proceedings of the 1993 Smart Structures and Materials Conference, Smart Structures and Intelligent Systems, Eds. Hagood, N. W. and Knowles, G. J., SPIE Vol, 1917, 1993, pp. 267-284.

50. Schetky, L. McD., Liang, C. and Rogers, C. A., "Hybrid Composite Materials Using Shape Memory Alloy Actuators to Provide Vibration and Acoustic Control," Proceedings of the 1994 SPIE Smart Structures and Materials Symposium, Smart Structures and Intelligent Systems, Ed. Hagood, N. W., SPIE Vol. 2190, 1994, pp. 422-433.

51. Epps, J. and Chandra, R., "Shape Memory Alloy Actuation for Active Tuning of Composite Beams," Presented at the 1995 SPIE's North American Conference on Smart Materials and Structures, February 26-March 3, 1995.

52. Segalman, D. J., Parker, G. G. and Inman, D. J., "Vibration Suppression by Modulation of Elastic Modulus using Shape Memory Alloys," *Intelligent Structures, Materials and Vibrations*, ASME, New York, 1993, pp. 1-5.

53. Graesser, E. J., "Effect of Intrinsic Damping on Vibration Transmissibility of Nickel-Titanium Shape Memory Alloy Springs," *Metallurgical and Material Transactions*, Vol. 26A, 1995, pp. 2791-2796.

54. Birman, V., "Optimum Design of Hybrid Shape Memory Alloy Sandwich Panels for Maximum Natural Frequencies," Proceedings of the 1996 Smart Structures and Materials Conference, Industrial and Commercial Applications of Smart Structures Technologies, Ed. Crowe, C. R., SPIE Vol. 2721, 1996, pp. 263-272.

55. Clarkson, B. L., "Review of Sonic Fatigue Technology," NASA CR-4587, NASA Langley Research Center, April, 1994.

56. Wu, W. -H. and Witmer, E. A., "Finite-Element Analysis of Large Elastic-Plastic Transient Deformations of Simple Structures," *AIAA Journal*, Vol. 9, No. 9, 1971, pp. 1719-1724.

57. Wu, W. -H. and Witmer, E. A., "The Dynamic Responses of Cylindrical Shells Including Geometric and Material Nonlinearities," *International Journal of Solids and Structures*, Vol. 10, 1974, pp. 243-260.

58. Wu, W. -H. and Witmer, E. A., "Nonlinear Transient Responses of Structures by the Spatial Finite-Element Method," *AIAA Journal*, Vol. 11, No. 8, 1973, pp. 1110-1117.

59. Heifitz, J. H. and Costantino, C. J., "Dynamic Response of Nonlinear Media at Large Strains, Journal of the Engineering Mechanics Division," Proceedings of the American Society of Civil Engineering, December, 1972, pp. 1511-1528.

60. Belytschko, T. and Hsieh, B. J., "Non-Linear Transient Finite Element Analysis with Convected Co-ordinates," *International Journal for Numerical Methods in Engineering*, Vol. 7, 1973, pp. 255-271.

61. Tillerson, J. R., Stricklin, J. A. and Haisler, W. E., "Numerical Methods for the Solution of Nonlinear Problems in Structural Analysis," Proceedings of the Winter Annual Meeting of the American Society of Mechanical Engineers, AMD-Vol. 6, 1973, pp. 67-101.

62. Tessler, A. and Hughes, T. J. R., "A Three-Node Mindlin Plate Element with Improved Transverse Shear," *Computer Methods in Applied Mechanics and Engineering*, Vol. 50, 1985, pp. 71-101.

63. Xue, David., "Finite Element Frequency Domain Solution of Nonlinear Panel Flutter with Temperature Effects and Fatigue Life Analysis," Ph.D. Dissertation, 1991, Old Dominion University, Norfolk, Virginia.

64. Chen, R., "Finite Element Nonlinear Random Response of Composite Panels of Arbitrary Shape to Acoustic and Thermal Loads," Ph.D. Dissertation, 1995, Old Dominion University, Norfolk, Virginia.

65. Chiang, C. K., "A Finite Element Large Deflection Multiple-Mode Random Response Analysis of Complex Panels with Initial Stress Subjected to Acoustic Loading," Ph.D. Dissertation, 1988, Old Dominion University, Norfolk, Virginia.

APPENDIX A

FORMULATIONS FOR STRAIN INTERPOLATION MATRICES

$$[C_m] = \frac{1}{2A}\begin{bmatrix} y_{23} & y_{31} & y_{12} & 0 & 0 & 0 \\ 0 & 0 & 0 & x_{32} & x_{13} & x_{21} \\ x_{32} & x_{13} & x_{21} & y_{23} & y_{31} & y_{12} \end{bmatrix} \tag{A.1}$$

$$[C_{\psi b}] = \frac{1}{2A}\begin{bmatrix} y_{23} & y_{31} & y_{12} \\ x_{32} & x_{13} & x_{21} \end{bmatrix} \tag{A.2}$$

$$[C_{\psi\psi}] = \frac{1}{2A}\begin{bmatrix} C_{\psi\psi 11} & C_{\psi\psi 12} & C_{\psi\psi 13} & C_{\psi\psi 14} & C_{\psi\psi 15} & C_{\psi\psi 16} \\ C_{\psi\psi 21} & C_{\psi\psi 22} & C_{\psi\psi 23} & C_{\psi\psi 24} & C_{\psi\psi 25} & C_{\psi\psi 26} \end{bmatrix} \tag{A.3}$$

$$[C_b] = \frac{1}{2A}\begin{bmatrix} 0 & 0 & 0 & y_{23} & y_{31} & y_{12} \\ x_{32} & x_{13} & x_{21} & 0 & 0 & 0 \\ y_{23} & y_{31} & y_{12} & x_{32} & x_{13} & x_{21} \end{bmatrix} \tag{A.4}$$

$$[C_{\gamma b}] = \frac{1}{2A}\begin{bmatrix} x_{32} & x_{13} & x_{21} \\ y_{23} & y_{31} & y_{12} \end{bmatrix} \tag{A.5}$$

$$[C_{\gamma\psi}] = \begin{bmatrix} C_{\psi\psi 21} + \xi_1 & C_{\psi\psi 22} + \xi_2 & C_{\psi\psi 23} + \xi_3 & C_{\psi\psi 24} & C_{\psi\psi 25} & C_{\psi\psi 26} \\ C_{\psi\psi 11} & C_{\psi\psi 12} & C_{\psi\psi 13} & C_{\psi\psi 14} + \xi_1 & C_{\psi\psi 15} + \xi_2 & C_{\psi\psi 16} + \xi_3 \end{bmatrix} \tag{A.6}$$

where $C_{\psi\psi ij}$'s $(i = 1,2;\ j = 1,2,\ldots,6)$ are related to the area coordinates and the coordinates of the three nodes.

$$C_{\psi\psi 11} = \frac{1}{2}(y_{12}\xi_2 - y_{31}\xi_3)y_{23} \tag{A.7}$$

$$C_{\psi\psi 12} = \frac{1}{2}(y_{23}\xi_3 - y_{12}\xi_1)y_{31} \tag{A.8}$$

$$C_{\psi\psi 13} = \frac{1}{2}(y_{31}\xi_1 - y_{23}\xi_2)y_{12} \tag{A.9}$$

$$C_{\psi\psi14}=\frac{1}{2}(x_{13}\xi_3-x_{21}\xi_2)y_{23}-\frac{1}{2}x_{21}\xi_1y_{31}+\frac{1}{2}x_{13}\xi_1y_{12} \quad \text{(A.10)}$$

$$C_{\psi\psi15}=\frac{1}{2}(x_{21}\xi_1-x_{32}\xi_3)y_{31}-\frac{1}{2}x_{32}\xi_2y_{12}+\frac{1}{2}x_{21}\xi_2y_{23} \quad \text{(A.11)}$$

$$C_{\psi\psi16}=\frac{1}{2}(x_{32}\xi_2-x_{13}\xi_1)y_{12}-\frac{1}{2}x_{13}\xi_3y_{23}+\frac{1}{2}x_{32}\xi_3y_{31} \quad \text{(A.12)}$$

$$C_{\psi\psi21}=\frac{1}{2}(y_{12}\xi_2-y_{31}\xi_3)x_{32}-\frac{1}{2}x_{21}\xi_1y_{31}+\frac{1}{2}x_{13}\xi_1y_{12} \quad \text{(A.13)}$$

$$C_{\psi\psi22}=\frac{1}{2}(y_{23}\xi_3-y_{12}\xi_1)x_{13}-\frac{1}{2}x_{32}\xi_2y_{12}+\frac{1}{2}x_{21}\xi_2y_{23} \quad \text{(A.14)}$$

$$C_{\psi\psi23}=\frac{1}{2}(y_{31}\xi_1-y_{23}\xi_2)x_{21}-\frac{1}{2}x_{13}\xi_3y_{23}+\frac{1}{2}x_{32}\xi_3y_{31} \quad \text{(A.15)}$$

$$C_{\psi\psi24}=\frac{1}{2}(x_{13}\xi_3-x_{21}\xi_2)x_{32} \quad \text{(A.16)}$$

$$C_{\psi\psi25}=\frac{1}{2}(x_{21}\xi_1-x_{32}\xi_3)x_{13} \quad \text{(A.17)}$$

$$C_{\psi\psi26}=\frac{1}{2}(x_{32}\xi_2-x_{13}\xi_1)x_{21} \quad \text{(A.18)}$$

APPENDIX B

THE ELEMENT MATRICES

Linear stiffness matrix

$$[k]_{\psi} = \int_A [C_b]^T [D][C_b] dA \tag{B.1}$$

$$[k]_{\psi m} = \int_A [C_b]^T [B][C_m] dA \tag{B.2}$$

$$[k]_{m\psi} = \int_A [C_m]^T [B][C_b] dA \tag{B.3}$$

$$[k]_{m} = \int_A [C_m]^T [A][C_m] dA \tag{B.4}$$

Linear stiffness matrix due to $w_o(x, y)$

$$[k_o]_b = \int_A [C_{\psi b}]^T [\theta_o]^T [A][\theta_o][C_{\psi b}] dA \tag{B.5}$$

$$[k_o]_{b\psi} = \int_A [C_{\psi b}]^T [\theta_o]^T [B][C_b] dA + \int_A [C_{\psi b}]^T [\theta_o]^T [A][\theta_o][C_{\psi\psi}] dA \tag{B.6}$$

$$[k_o]_{bm} = \int_A [C_{\psi b}]^T [\theta_o]^T [A][C_m] dA \tag{B.7}$$

$$[k_o]_{\psi b} = \int_A [C_b]^T [B][\theta_o][C_{\psi b}] dA + \int_A [C_{\psi\psi}]^T [\theta_o]^T [A][\theta_o][C_{\psi b}] dA \tag{B.8}$$

$$\begin{aligned} [k_o]_{\psi} = & \int_A [C_{\psi\psi}]^T [\theta_o]^T [B][C_b] dA + \int_A [C_b]^T [B][\theta_o][C_{\psi\psi}] dA \\ & + \int_A [C_{\psi\psi}]^T [\theta_o]^T [A][\theta_o][C_{\psi\psi}] dA \end{aligned} \tag{B.9}$$

$$[k_o]_{\psi m} = \int_A [C_{\psi\psi}]^T [\theta_o]^T [A][C_m] dA \tag{B.10}$$

$$[k_o]_{mb} = \int_A [C_m]^T [\theta_o]^T [A][C_{\psi b}] dA \tag{B.11}$$

$$[k_o]_{m\psi} = \int_A [C_m]^T [A][\theta_o][C_{\psi\psi}] dA \tag{B.12}$$

Linear stiffness matrix due to $\{N_{\Delta T}\}$

$$[k_{N\Delta T}]_b = \int_A [C_{\psi b}]^T [N_{\Delta T}][C_{\psi b}] dA \tag{B.13}$$

$$[k_{N\Delta T}]_{b\psi} = \int_A [C_{\psi b}]^T [N_{\Delta T}][C_{\psi\psi}] dA \tag{B.14}$$

$$[k_{N\Delta T}]_{\psi b} = \int_A [C_{\psi\psi}]^T [N_{\Delta T}][C_{\psi b}] dA \tag{B.15}$$

$$[k_{N\Delta T}]_{\psi} = \int_A [C_{\psi\psi}]^T [N_{\Delta T}][C_{\psi\psi}] dA \tag{B.16}$$

Stiffness matrix due to $\{N_r^*\}$

$$[k_r^*]_b = \int_A [C_{\psi b}]^T [N_r^*][C_{\psi b}] dA \tag{B.17}$$

$$[k_r^*]_{b\psi} = \int_A [C_{\psi b}]^T [N_r^*][C_{\psi\psi}] dA \tag{B.18}$$

$$[k_r^*]_{\psi b} = \int_A [C_{\psi\psi}]^T [N_r^*][C_{\psi b}] dA \tag{B.19}$$

$$[k_r^*]_{\psi} = \int_A [C_{\psi\psi}]^T [N_r^*][C_{\psi\psi}] dA \tag{B.20}$$

Stiffness Matrices due to $\{N_\sigma\}$

$$[k_\sigma]_b = \int_A [C_{\psi b}]^T [N_\sigma][C_{\psi b}] dA \tag{B.21}$$

$$[k_\sigma]_{b\psi} = \int_A [C_{\psi b}]^T [N_\sigma][C_{\psi\psi}] dA \tag{B.22}$$

$$[k_\sigma]_{\psi b} = \int_A [C_{\psi\psi}]^T [N_\sigma][C_{\psi b}] dA \tag{B.23}$$

$$[k_\sigma]_{\psi} = \int_A [C_{\psi\psi}]^T [N_\sigma][C_{\psi\psi}] dA \tag{B.24}$$

First-order nonlinear stiffness matrix

$$[nl_l]_{b\psi} = \int_A [C_{\psi b}]^T [\theta]^T [B][C_b] dA \tag{B.25}$$

$$[nl_l]_{bm} = \int_A [C_{\psi b}]^T [\theta]^T [A][C_m] dA \tag{B.26}$$

$$[nl_l]_{\psi b} = \int_A [C_b]^T [B][\theta][C_{\psi b}] dA \tag{B.27}$$

$$[nl_l]_{\psi} = \int_A [C_b]^T [B][\theta][C_{\psi\psi}] dA + \int_A [C_{\psi\psi}]^T [\theta]^T [B][C_b] dA \tag{B.28}$$

$$[nl_l]_{\psi m} = \int_A [C_{\psi\psi}]^T [\theta]^T [A][C_m] dA \tag{B.29}$$

$$[nl_l]_{mb} = \int_A [C_m]^T [A][\theta][C_{\psi b}] dA \tag{B.30}$$

$$[nl_l]_{m\psi} = \int_A [C_m]^T [A][\theta][C_{\psi\psi}] dA \tag{B.31}$$

First-order nonlinear stiffness matrix due to $\{w_o\}$

$$[nl_o]_b = \int_A [C_{\psi b}]^T [\theta]^T [A][\theta_o][C_{\psi b}] dA + \int_A [C_{\psi b}]^T [\theta_o]^T [A][\theta][C_{\psi b}] dA \tag{B.32}$$

$$[nl_o]_{b\psi} = \int_A [C_{\psi b}]^T [\theta]^T [A][\theta_o][C_{\psi\psi}] dA + \int_A [C_{\psi b}]^T [\theta_o]^T [A][\theta][C_{\psi\psi}] dA \tag{B.33}$$

$$[nl_o]_{\psi b} = \int_A [C_{\psi\psi}]^T [\theta]^T [A][\theta_o][C_{\psi b}] dA + \int_A [C_{\psi\psi}]^T [\theta_o]^T [A][\theta][C_{\psi b}] dA \tag{B.34}$$

$$[nl_o]_{\psi} = \int_A [C_{\psi\psi}]^T [\theta]^T [A][\theta_o][C_{\psi\psi}] dA + \int_A [C_{\psi\psi}]^T [\theta_o]^T [A][\theta][C_{\psi\psi}] dA \tag{B.35}$$

First-order nonlinear stiffness matrix due to $\{N_m\}(= [A]\{\varepsilon_m^o\})$

$$[nl_{Nm}]_b = \int_A [C_{\psi b}]^T [N_m][C_{\psi b}] dA \tag{B.36}$$

$$[nl_{Nm}]_{b\psi} = \int_A [C_{\psi b}]^T [N_m][C_{\psi\psi}] dA \tag{B.37}$$

$$[nl_{Nm}]_{\psi b} = \int_A [C_{\psi\psi}]^T [N_m][C_{\psi b}] dA \tag{B.38}$$

$$[nl_{Nm}]_{\psi} = \int_A [C_{\psi\psi}]^T [N_m][C_{\psi\psi}] dA \tag{B.39}$$

First-order nonlinear stiffness matrix due to $\{N_b\}(=[B]\{\kappa\})$

$$[n1_{Nb}]_b = \int_A [C_{\psi b}]^T [N_b][C_{\psi b}] dA \tag{B.40}$$

$$[n1_{Nb}]_{b\psi} = \int_A [C_{\psi b}]^T [N_b][C_{\psi\psi}] dA \tag{B.41}$$

$$[n1_{Nb}]_{\psi b} = \int_A [C_{\psi\psi}]^T [N_b][C_{\psi b}] dA \tag{B.42}$$

$$[n1_{Nb}]_{\psi} = \int_A [C_{\psi\psi}]^T [N_b][C_{\psi\psi}] dA \tag{B.43}$$

Second-order nonlinear stiffness matrix

$$[n2]_b = \frac{3}{2}\int_A [C_{\psi b}]^T [\theta]^T [A][\theta][C_{\psi b}] dA \tag{B.44}$$

$$[n2]_{b\psi} = \frac{3}{2}\int_A [C_{\psi b}]^T [\theta]^T [A][\theta][C_{\psi\psi}] dA \tag{B.45}$$

$$[n2]_{\psi b} = \frac{3}{2}\int_A [C_{\psi\psi}]^T [\theta]^T [A][\theta][C_{\psi b}] dA \tag{B.46}$$

$$[n2]_{\psi} = \frac{3}{2}\int_A [C_{\psi\psi}]^T [\theta]^T [A][\theta][C_{\psi\psi}] dA \tag{B.47}$$

Linear stiffness matrix due to shear

$$[k_s]_b = \beta\int_A [C_{\gamma b}]^T [A_s][C_{\gamma b}] dA \tag{B.48}$$

$$[k_s]_{b\psi} = \beta\int_A [C_{\gamma b}]^T [A_s][C_{\gamma\psi}] dA \tag{B.49}$$

$$[k_s]_{\psi b} = \beta\int_A [C_{\gamma\psi}]^T [A_s][C_{\gamma b}] dA \tag{B.50}$$

$$[k_s]_{\psi} = \beta\int_A [C_{\gamma\psi}]^T [A_s][C_{\gamma\psi}] dA \tag{B.51}$$

Mass Matrix

$$[m]_b = \int_A [H_w]^T \rho h [H_w] dA \tag{B.52}$$

$$[m]_{b\psi} = \int_A [H_w]^T \rho h [H_{w\psi}] dA \tag{B.53}$$

$$[m]_{\psi b} = \int_A [H_{w\psi}]^T \rho h [H_w] dA \tag{B.54}$$

$$[m]_{\psi} = \int_A [H_{w\psi}]^T \rho h [H_{w\psi}] dA \tag{B.55}$$

$$[m]_m = \int_A ([H_u]+[H_v])^T \rho h ([H_u]+[H_v]) dA \tag{B.56}$$

Load vectors due to distributed force $p(x, y, t)$

$$\{p_p(t)\}_b = \int_A [H_w]^T p(x,y,t) dA \tag{B.57}$$

$$\{p_p(t)\}_{\psi} = \int_A [H_{w\psi}]^T p(x,y,t) dA \tag{B.58}$$

Load vectors due to $\{N_{\Delta T}\}$

$$\{p_{\Delta T}\}_{\psi} = \int_A [C_b]^T \{M_{\Delta T}\} dA \tag{B.59}$$

$$\{p_{\Delta T}\}_m = \int_A [C_m]^T \{N_{\Delta T}\} dA \tag{B.60}$$

Load vectors due to recovery stress $\{\sigma_r^*\}$

$$\{p_r^*\}_{\psi} = \int_A [C_b]^T \{M_r^*\} dA \tag{B.61}$$

$$\{p_r^*\}_m = \int_A [C_m]^T \{N_r^*\} dA \tag{B.62}$$

Load vectors due to initial stress $\{\sigma_o\}$ and $\{\tau_o\}$

$$\{p_{\sigma}\}_{\psi} = \int_A [C_b]^T \{M_{\sigma}\} dA \tag{B.63}$$

$$\{p_{\sigma}\}_m = \int_A [C_m]^T \{N_{\sigma}\} dA \tag{B.64}$$

$$\{p_{\tau}\}_b = \beta \int_A [C_{\gamma b}]^T \{R_{\sigma}\} dA \tag{B.65}$$

$$\{p_\tau\}_\psi = \beta\int_A [C_{\gamma\psi}]^T \{R_\sigma\} dA \tag{B.66}$$

Load vectors due to coupling between $\{N_{\Delta T}\}$ and w_o

$$\{p_{\Delta To}\}_b = \int_A [C_{\psi b}]^T [\theta_o]^T \{N_{\Delta T}\} dA \tag{B.67}$$

$$\{p_{\Delta To}\}_\psi = \int_A [C_{\psi\psi}]^T [\theta_o]^T \{N_{\Delta T}\} dA \tag{B.68}$$

Load vectors due to coupling between $\{\sigma_r^*\}$ and w_o

$$\{p_{ro}^*\}_b = \int_A [C_{\psi b}]^T [\theta_o]^T \{N_r^*\} dA \tag{B.69}$$

$$\{p_{ro}^*\}_\psi = \int_A [C_{\psi\psi}]^T [\theta_o]^T \{N_r^*\} dA \tag{B.70}$$

Load vectors due to coupling between $\{\sigma_o\}$ and w_o

$$\{p_{\sigma o}\}_b = \int_A [C_{\psi b}]^T [\theta_o]^T \{N_\sigma\} dA \tag{B.71}$$

$$\{p_{\sigma o}\}_\psi = \int_A [C_{\psi\psi}]^T [\theta_o]^T \{N_\sigma\} dA \tag{B.72}$$

APPENDIX C

DERIVATION OF SYSTEM STATIC AND DYNAMIC EQUATIONS

The solution of the system equation of motion, Eq. (2.70), can be assumed to be the sum of a time-independent solution $\{W\}_s$ and a time-independent solution $\{W\}_t$

$$\{W\} = \{W\}_s + \{W\}_t \tag{C.1}$$

Substituting Eq. (C.1) into Eq. (2.70) leads to

$$\begin{aligned}
&[M](\{\ddot{W}\}_s + \{\ddot{W}\}_t) + ([K] + [K_o] - [K_{N\Delta T}] + [K_r^*] + [K_\sigma] + [K_s])(\{W\}_s + \{W\}_t) \\
&+ \tfrac{1}{2}[N1]_{s+t}(\{W\}_s + \{W\}_t) + \tfrac{1}{3}[N2]_{s+t}(\{W\}_s + \{W\}_t) \\
&= \{P_p(t)\} + \{P_{\Delta T}\} - \{P_r^*\} - \{P_\sigma\} - \{P_\tau\} + \{P_{\Delta To}\} - \{P_{ro}^*\} - \{P_{\sigma o}\}
\end{aligned} \tag{C.2}$$

where subscripts s and t, [ ]$_s$ and [ ]$_t$, denote that the corresponding nonlinear stiffness matrix is evaluated by using $\{W\}_s$ and $\{W\}_t$, respectively.

In Eq. (C.2), the nonlinear stiffness matrices $[N1]_{s+t}$ and $[N2]_{s+t}$ are evaluated in Appendix B, and they can be separated as [64]

$$[N1]_{s+t} = [N1]_s + [N1]_t \tag{C.3}$$

$$[N2]_{s+t} = [N2]_s + [N2]_{st} + [N2]_{ts} + [N2]_t \tag{C.4}$$

then, Eq. (C.2) can be rearranged as

$$\begin{aligned}
&[M]\{\ddot{W}\}_t + ([K] + [K_o] - [K_{N\Delta T}] + [K_r^*] + [K_\sigma] + [K_s])\{W\}_t \\
&+ \tfrac{1}{2}[N1]_t\{W\}_t + \tfrac{1}{3}[N2]_t\{W\}_t \\
&+ \tfrac{1}{2}([N1]_s\{W\}_t + [N1]_t\{W\}_s) + \tfrac{1}{3}([N2]_{st} + [N2]_{ts})(\{W\}_s + \{W\}_t) + \tfrac{1}{3}[N2]_s\{W\}_t + \tfrac{1}{3}[N2]_t\{W\}_s \\
&+ ([K] + [K_o] - [K_{N\Delta T}] + [K_r^*] + [K_\sigma] + [K_s])\{W\}_s \\
&+ \tfrac{1}{2}[N1]_s\{W\}_s + \tfrac{1}{3}[N2]_s\{W\}_s \\
&= \{P_p(t)\} + \{P_{\Delta T}\} - \{P_r^*\} - \{P_\sigma\} - \{P_\tau\} + \{P_{\Delta To}\} - \{P_{ro}^*\} - \{P_{\sigma o}\}
\end{aligned} \tag{C.5}$$

From the rearrangement of element level equation shown in Appendix B, the following relations are established and proved

$$[N1]_s\{W\}_t = [N1]_t\{W\}_s \tag{C.6}$$

$$[N2]_{st} = [N2]_{ts} \tag{C.7}$$

$$[N2]_t\{W\}_s = [N2]_{st}\{W\}_t \tag{C.8}$$

$$[N2]_{st}\{W\}_s = [N2]_s\{W\}_t \tag{C.9}$$

Substituting Eqs. (C.6), (C.7), (C.8) and (C.9) into Eq. (C.5) leads to

$$F(\{W\}_s) = G(\{W\}_t) \tag{C.10}$$

where

$$\begin{aligned} F(\{W\}_s) = {} & ([K]+[K_o]-[K_{N\Delta T}]+[K_r^*]+[K_\sigma]+[K_s])\{W\}_s \\ & +\frac{1}{2}[N1]_s\{W\}_s+\frac{1}{3}[N2]_s\{W\}_s \\ & -\{P_{\Delta T}\}+\{P_r^*\}+\{P_\sigma\}+\{P_\tau\}-\{P_{\Delta To}\}+\{P_{ro}^*\}+\{P_{\sigma o}\} \end{aligned} \tag{C.11}$$

$$\begin{aligned} G(\{W\}_t) = {} & [M]\{\ddot{W}\}_t+([K]+[K_o]-[K_{N\Delta T}]+[K_r^*]+[K_\sigma]+[K_s])\{W\}_t \\ & +[N1]_s\{W\}_t+[N2]_s\{W\}_t \\ & +\tfrac{1}{2}[N1]_t\{W\}_t+\tfrac{1}{3}[N2]_t\{W\}_t+[N2]_{st}\{W\}_t \\ & -\{P_p(t)\} \end{aligned} \tag{C.12}$$

In Eq. (C.10), function F({W}$_s$} is independent of time while function G({W}$_t$} is time dependent. Therefore, the only possible solution for F({W}$_s$} and G({W}$_t$} to exist is that both F({W}$_s$} and G({W}$_t$} equal to zero. Thus the following complete static and dynamic equations are obtained.

$$
\begin{aligned}
&([K]+[K_o]-[K_{N\Delta T}]+[K_r^{\bullet}]+[K_\sigma]+[K_s])\{W\}_s \\
&+\frac{1}{2}[N1]_s\{W\}_s+\frac{1}{3}[N2]_s\{W\}_s \\
&=\{P_{\Delta T}\}-\{P_r^{\bullet}\}-\{P_\sigma\}-\{P_\tau\}+\{P_{\Delta To}\}-\{P_{ro}^{\bullet}\}-\{P_{\sigma o}\}
\end{aligned}
\tag{C.13}
$$

and

$$
\begin{aligned}
&[M]\{\ddot{W}\}_t+([K]+[K_o]-[K_{N\Delta T}]+[K_r^{\bullet}]+[K_\sigma]+[K_s])\{W\}_t \\
&+[N1]_s\{W\}_t+[N2]_s\{W\}_t \\
&+\tfrac{1}{2}[N1]_t\{W\}_t+\tfrac{1}{3}[N2]_t\{W\}_t+[N2]_{st}\{W\}_t \\
&=\{P_p(t)\}
\end{aligned}
\tag{C.14}
$$

where the subscript [ ]$_s$ denotes that the corresponding stiffness matrix is evaluated with static deflection, [ ]$_{st}$ is determined by static deflection and dynamic deflection and [ ]$_t$ is evaluated with dynamic deflection. Neglecting the higher order terms of {W}$_t$ in Eq. (C.14) for small amplitude random vibrations, the simply dynamic equation can be obtained as

$$
\begin{aligned}
&[M]\{\ddot{W}\}_t+([K]+[K_o]-[K_{N\Delta T}]+[K_r^{\bullet}]+[K_\sigma]+[K_s])\{W\}_t \\
&+[N1]_s\{W\}_t+[N2]_s\{W\}_t \\
&=\{P_p(t)\}
\end{aligned}
\tag{C.15}
$$

VITA

Zhiwei Zhong was born in Wuhan, P.R.China on October 4, 1963. In June 1985, he graduated from Wuhan Institute of Technology with a Bachelor of Science in Automotive Engineering. In June 1990, he received his Master degree from the Mechanical Engineering Department (I) at Huazhong University of Science and Technology. He began to pursue a Ph.D degree in the Department of Mechanical Engineering and Mechanics at Old Dominion University in the Fall of 1992. His Ph.D. research was in the area of shape memory alloys. He graduated with his Ph.D. degree in Engineering Mechanics. He now is a Test Engineer at ITT Automotive, Inc., Auburn Hills, MI.

IMAGE EVALUATION
TEST TARGET (QA-3)

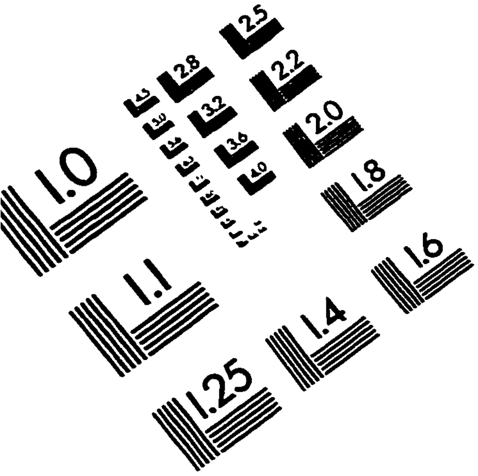

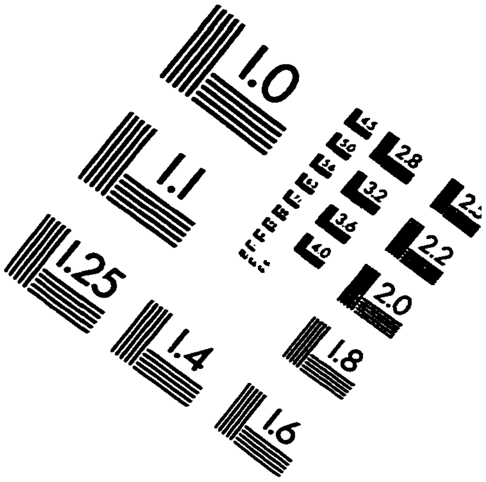

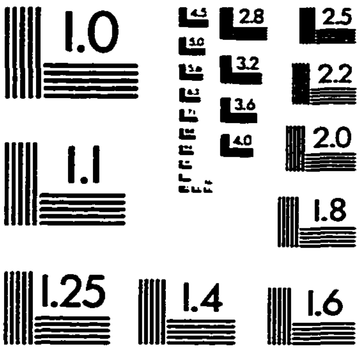

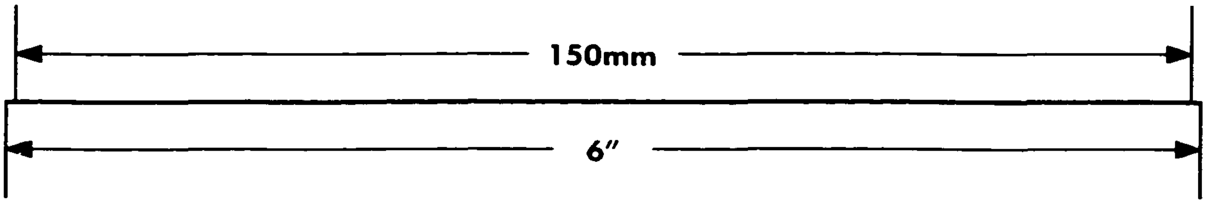

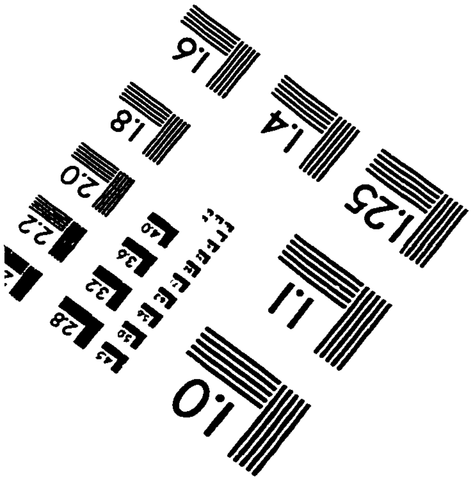

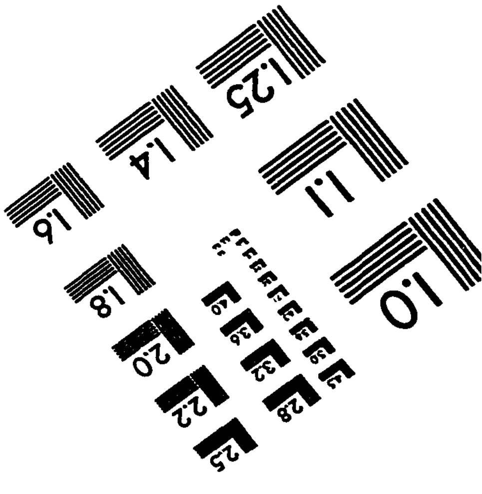

APPLIED IMAGE . Inc
1653 East Main Street
Rochester, NY 14609 USA
Phone: 716/482-0300
Fax: 716/288-5989